Effects of Non-hydrocarbon Liquids on Particulate Emissions of Flares

by

Mohsen Kazemimanesh

A thesis submitted in partial fulfillment of the requirements for the degree of

Master of Science

Department of Mechanical Engineering
University of Alberta

Abstract

To investigate the effects of non-hydrocarbon liquids found in the produced water following fracturing operations on particulate emissions of flares, a small-scale experiment with methane diffusion flame was used. Size distributions, mass-mobility relationships, effective density, volatility, and elemental analysis of particulate emissions from unseeded and seeded flames were obtained. To mimic real flaring, another pilot-scale experiment using a 2-in. diameter burner with a methane-based turbulent diffusion flame with flow conditions and fuel composition typical of flares in the petroleum industry was used. Particle morphology was determined using Transmission Electron Microscopy (TEM). Particle size distributions, soot volume fractions, and emission factors were obtained using Scanning Mobility Particle Sizer (SMPS) and Laser-Induced Incandescence (LII). The results showed that emission factor depended on the liquid mass ratio. Distilled water and HCl solution decreased emission factor. Emission factor was orders of magnitude higher for NaCl-doped flames; however, majority of particles were NaCl and soot emission was suppressed in this case.

Preface

Some of the research conducted for the Chapter 3 of this thesis was conducted in collaboration with Energy and Emissions Research Lab at Carleton University. The flare facility used in Chapter 3 was designed and constructed by Dr. Matthew Johnson and Darcy Corbin; however, the burner and liquid delivery and generation system was designed by myself. The flare facility at Carleton University was operated by Darcy Corbin for the course of this research. He also operated the LII and FTIR gas analyzer to measure soot volume fraction and CO_2 mole fraction, respectively, which I used for the calculation of dilution ratio and emission factor. Furthermore, particle morphology analysis discussed in Chapter 3 was carried out by Dr. Steven Rogak and Ramin Dastanpour at the University of British Columbia. The rest of the work presented in Chapter 3 is my original work.

Acknowledgements

I would like to express my appreciation to my supervisor, Dr. Jason Olfert, for his encouragement, support, and scientific guidance during the course of this research. He has been a truly supportive supervisor who helped me a lot with his ideas to improve this study. I could not ask for a better supervisor.

I also acknowledge my co-supervisor, Dr. Larry Kostiuk, for his informative feedbacks and ideas, and his support and enthusiasm for this research. His intrinsic scientific curiosity pushed this research forward and I always learned from his extensive knowledge in the field of combustion. I also thank him for providing his decent lab to run our experiments.

I would like to extend my gratitude to Dr. Matthew Johnson and Darcy Corbin for allowing/helping us to use their flare facility at Carleton University. Dr. Johnson is very knowledgeable in all matters of flaring and I learned much from him. Darcy was so generous to invest his personal time to operate the facility for our pilot-scale experiment under a tight schedule.

I should also thank Dr. Steven Rogak and Ramin Dastanpour from the University of British Columbia for their help during running the pilot-scale experiments and conducting TEM analysis on the samples.

Finally, I need to appreciate my colleagues in our research group, especially Ali Momeni and Tyler Johnson, for their assistance on running DMA, CPC, CPMA, etc. and for their insightful thoughts on this research.

Table of Contents

List of Figures

List of Tables

Nomenclature

List of Symbols

AF_s	Stoichiometric air-to-fuel mass ratio
d_e	Burner exit diameter (m)
d_m	Particle mobility diameter (nm)
D_m	Mass-mobility exponent
$dN/d\log d_m$	Normalized particle concentration (cm^{-3})
Fr_f	Fire Froude number
Fr_g	Gas Froude number
f_s	Stoichiometric fuel fraction
f_v	Soot volume fraction (ppb)
g	Gravitation acceleration (m/s^2)
k	Constant coefficient of mass-mobility relationship
m	Particle mass
$\dot{m}$	Mass flow rate (kg/s)
$m(d_m)$	Mass-mobility function
M_{fuel}	Molar mass of fuel (g/mol)
M_{tot}	Total particle mass concentration (g/m^3)
N	Particle number concentration (cm^{-3})
$\dot{n}$	Molar flow rate (mol/s)
P	Pressure (Pa)
P_{sat}	Saturation pressure (Pa)
P_{stat}	Static pressure (Pa)

P_v	Vapour partial pressure (Pa)
R	Ideal gas constant (8.314 J/mol·K)
Re_s	Source Reynolds number
T	Temperature (K)
T_∞	Ambient temperature (K)
T_{adb}	Flame adiabatic temperature (K)
u_e	Fuel gas exit velocity (m/s)
V_{air}	Volume of air
V_{soot}	Volume of soot particles
w	Mass fraction
X	Mole fraction
x	Number of carbon atoms in the hydrocarbon
y	Number of hydrogen atoms in the hydrocarbon
Y_i	Mass fraction of component i
Y_{LII}	Mass emission factor measured by LII (mg/kg fuel)
Y_{SMPS}	Mass emission factor measured by SMPS (mg/kg fuel)
μ_∞	Dynamic viscosity of ambient air (Pa·s)
ρ_∞	Ambient air density (kg/m^3)
ρ_e	Fuel density (kg/m^3)
ρ_{eff}	Effective density (kg/m^3)
ρ_{soot}	Material density of soot (kg/m^3)
Φ	Equivalence ratio
ω	Humidity ratio

List of Acronyms

CMD	Count Median Diameter
CPC	Condensation Particle Counter
CPMA	Centrifugal Particle Mass Analyzer
DMA	Differential Mobility Analyzer
DR	Dilution Ratio
DT	Dilution Tunnel
EDS (EDX)	Energy-Dispersive X-ray Spectroscopy
FTIR	Fourier Transform Infrared Spectroscopy
GSD	Geometric Standard Deviation
ID	Internal Diameter
IPCC	Intergovernmental Panel on Climate Change
LII	Laser-Induced Incandescence
NPRI	National Pollutant Release Inventory
PM	Particulate Matter
SLPM	Standard Litre Per Minute
SMPS	Scanning Mobility Particle Sizer
TD	Thermo-denuder
TEM	Transmission Electron Microscopy
UOG	Upstream Oil and Gas
XPS	X-ray Photoelectron Microscopy

CHAPTER 1

Introduction

This study investigates the effects of non-hydrocarbon liquids from fracturing operation on particulate emissions from the flares that carry over these liquid droplets. This chapter presents a brief overview of the flaring process, the extent of flaring in the oil and gas industry and its health and environmental implications, hydraulic fracturing and its significance with regard to flaring, objectives of the current study, and finally an introduction to the next chapters in this thesis.

1.1 Flaring

There are two processes used extensively in the upstream oil and gas (UOG) industry and downstream petrochemical industry to dispose of unwanted gases: flaring and venting. In flaring, the undesired flammable gases are burned off in an open atmosphere flame; however, in venting, the unwanted gases are simply released into the atmosphere. Gases are usually flared or vented because they are

not economic to process (*e.g.* when well sites are far from pipeline or it contains low-concentrations of toxic H_2S) or due to leakages or emergency blow-downs at facilities. The composition of flared or vented gases varies considerably from site to site but, generally, methane is the main component of these gases in the UOG.

Flaring can significantly reduce green-house gases compared to venting because the mass-based global warming potential of methane for a 100-year time horizon is 25 times higher than carbon dioxide produced from burning methane (Intergovernmental Panel on Climate Change, 2013). Therefore, flaring is often preferred over venting due to the mitigation of green-house gases. However, flaring has the potential to produce soot and other pollutants that have negative impacts on the environment and air quality (Pohl et al., 1986; Strosher, 2000; Johnson et al., 2001). The potential environmental effects of flaring and venting are discussed in more details in section 1.1.3.

The significance of these impacts becomes clearer by considering the sheer volume of flaring and venting. U.S. Energy Information Administration (2013) reported that the amount of gases flared or vented worldwide in 2008 was approximately 136.7 billion m^3. Another study used satellite imagery technique to reveal that an estimated 139 billion m^3 of gas was flared or vented globally (Elvidge et al., 2009). In Canada, the province of Alberta is the most significant source of flaring and venting (McEwen, 2010). In the petroleum industry in Alberta, approximately 941 million m^3 and 501 million m^3 of gas was flared and vented in 2012, respectively (Alberta Energy Regulator, 2013).

1.1.1 Categorization of flares

Many different strategies have been developed for flaring to meet the operating conditions needed in the industry. In the oil and gas industry, flares can be categorized into three main groups: production flares, process flares, and emergency flares (Johnson et al., 2001).

Production flaring refers to all kinds of flaring that occur in different levels of the upstream oil and gas industry. Production flaring can be divided into two categories: well testing and solution gas flaring. Well testing happens at the initial development of a gas well when gas may be flared at very high flow rates for the course of a few days. Well testing flares typically do not have engineered provisions for smoke reduction or flame stability. By contrast, solution gas flaring is usually established during the initial operation of an oil well. At this time, the associated gases may be flared while assessing their economic suitability as sale-grade natural gas. If the flared gases are not economic to conserve (a term used to describe the capture of these gases for sales), solution gas could continue to be flared for the life of the oil well. Typically, solution gas flares have significantly lower flow rates and exit velocities compared to well testing flares. However, due to the sheer number of solution gas flares and their continuous operation, solution gas flare is the primary source of flaring in the upstream oil and gas industry (Johnson et al., 2001).

Process flaring typically occurs at refineries, petrochemical plants, and sour gas plants. Gases that leak past the relief valves are directed to process flaring at these facilities. Process flaring is usually continuous and has relatively low flow rate;

however, during blow-down of process units or start-up and shutdown of the plant, significantly higher gas flow rates may be flared (Johnson et al., 2001).

Emergency flares typically occur at large refineries or gas plants during emergency situations when the safety of plant staff or the plant itself is a concern. Under an emergency situation, such as fire, valve rupture, compressor failure, over-pressure, large volumes of flammable gas needs to be disposed of very quickly. In these conditions, very high flow rates of gas may be flared and the exit velocity of gas from the flare stack can approach sonic velocity (Johnson et al., 2001).

1.1.2 Solution gas flaring

As mentioned in section 1.1.1, solution gas flaring is the main contributor to flaring volumes in Alberta and, therefore, it is discussed in more detail here. Solution gas is the dissolved gas released from oil when its pressure is reduced from high reservoir pressure to near atmospheric pressure (Johnson et al., 2001). When the oil is brought to the surface, any dissolved water or solution gas is separated from the oil at a facility known in the UOG industry as an "oil battery". In an oil battery site, oil is stored temporarily for further processing, while water is typically re-injected into the well and solution gas is flared, vented or conserved (as fuel source for the battery site or for sale).

Solution gas flare stacks are typically 10 m high with an internal diameter of ~100 mm in Alberta (Johnson et al., 2001). In contrast, commercial flares (such as flares used in petroleum refining, manufacturing industry, and landfill

applications) have a more complex design. Commercial flares can include commercial burner tip, pilot, and smoke suppressant. Commercial burner tips are usually complicated in design and may include crosswind protection, pilot flame integration, and steam injection. The pilot (or alternatively, electric spark) is used to keep the flare lit during start-up, when low heating value gas is flared, or during high crosswinds. Smoke suppressant typically includes steam or compressed air. It should be noted that despite many options that can potentially improve flaring performance, smaller or remotely-located solution gas flares rarely or never use these options (McEwen, 2010).

1.1.3 Environmental and health effects of flaring

Environmental issues of flaring are typically investigated in terms of efficiency and emissions. Flare efficiency is defined as the efficiency of combustion process in oxidizing the fuel completely (Johnson et al., 2001). In a typical solution gas flare, two different efficiencies are relevant: the carbon conversion efficiency is the measure of the ability of the flare in fully converting all hydrocarbons into CO_2, while sulfur conversion efficiency measures the ability of the flare in fully converting H_2S into SO_2 (Johnson et al., 2001).

When there is inefficiency in flaring, unburned hydrocarbons, carbon monoxide, soot, semi-volatile organic material, etc. is produced. Any unburned hydrocarbon increases the greenhouse gas emissions because global warming potentials of the hydrocarbons found in flares are higher than carbon dioxide. If the solution gas contains H_2S, then any unburned gas is potentially toxic (Johnson et al., 2001), though in this case, the oxidized sulphur (SO_2) is quite toxic.

A major particle emission from flaring is soot. Air pollution, including soot emission, has been extensively studied for its negative impacts on human health. Results from a 16-year prospective study in six U.S. cities shows that there is an association between fine particulate air pollution (particles with aerodynamic diameter less than 2.5 μm) and annual mortality rates from lung cancer and cardiopulmonary disease (Dockery et al., 1993). Results of this study were further reanalyzed and validated in another study funded by U.S. Environmental Protection Agency (Krewski et al., 2000). An important factor on deposition mechanisms in the respiratory tract is the particle size. Deposition in the upper respiratory tract for particles larger than 10 μm is generally due to impaction while for ultrafine particles (smaller than 100 nm) is due to diffusion.

Soot emissions are also a major contributor to positive radiative forcing of the earth's climate with an estimated radiative forcing of 0.9 W/m^2 (Ramanathan and Carmichael, 2008). Radiative forcing of CO_2 and CH_4 are 1.66 W/m^2 and 0.48 W/m^2, respectively (Intergovernmental Panel on Climate Change, 2013). These sources suggest that soot (black carbon) is the second largest contributor to globally averaged radiative forcing of the climate and global warming, after carbon dioxide. Some studies suggest that due to the relatively short lifespan of soot in the atmosphere (only a few weeks), reduction in soot emission is the fastest means of decreasing the trend of global warming in the short term (Ramanathan and Carmichael, 2008).

1.2 Hydraulic fracturing

Induced hydraulic fracturing (in short, hydraulic fracturing or fracturing) is a technique extensively used in the upstream oil and gas industry to increase extraction rate and recovery from oil and natural gas reservoirs. Hydraulic fracturing is very common to extract unconventional oil and natural gas that is trapped in low-permeability rock formations such as shale gas, shale oil (also known as, tight oil), and tight gas (Charlez, 1997).

Figure 1.1 shows a schematic of a typical hydraulic fracturing process for a horizontal wellbore. During hydraulic fracturing, water is mixed with proppant (usually sand, aluminium oxide, or ceramic pellets) and chemical additives and the mixture, known as fracturing fluid, is injected into the wellbore at high pressure. Wells can be drilled vertically for hundreds to thousands of meters into deep rock formations and may include horizontal sections extending for several

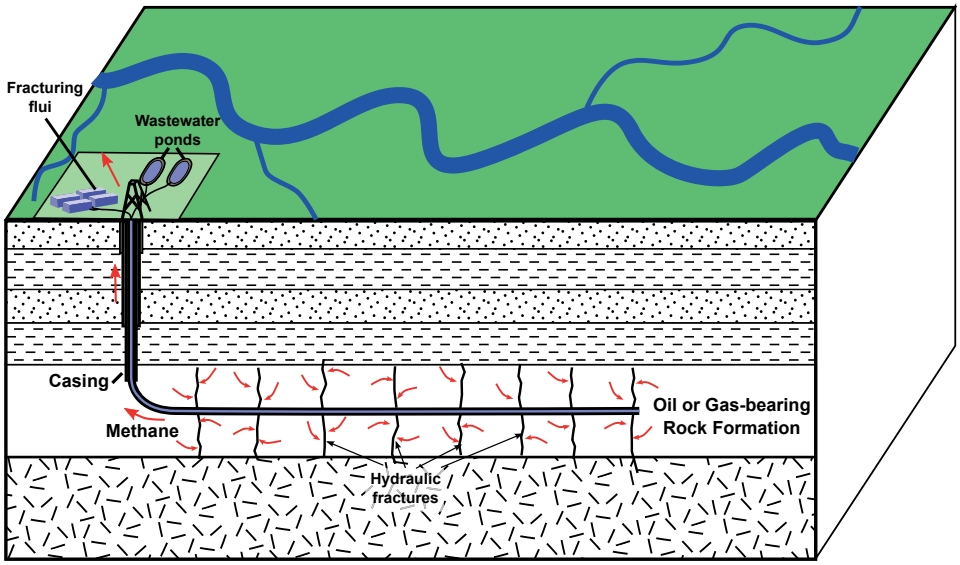

Adapted from Wikimedia Commons image file "HydroFrac2". Retrieved May 2014 from http://en.wikipedia.org/wiki/File:HydroFrac2.svg

Figure 1.1: Schematic of a typical hydraulic fracturing process for a horizontal wellbore

hundred meters into the rock formation. The injection of fracturing fluid into the wellbore at high pressure causes small fractures (typically less than 1 mm wide) in the rock formation and, oil, gas, and brine trapped in the formation can flow to the wellbore. The newly created fractures can extend several hundred meters away from the wellbore, thus increasing the extraction of oil and gas significantly. When the high pressure of fracturing fluid is removed, the internal pressure of the rock formation causes the fracturing fluid to return to the surface through the wellbore. This fluid is known as "produced water" and may contain chemical additives from fracturing fluid, brine, hydrocarbons, and metals. The proppant holds the fractures open in the formation after equilibrium, and oil and gas can continue to flow to the wellbore even after hydraulic fracturing is finished. It should be noted that hydraulic fracturing is usually targeted for a specific rock formation and the wellbore is sealed with an internal steel casing for non-targeted areas while perforated casing is used for the rock formation of interest (Arthur et al., 2008a).

1.2.1 Fracturing fluid composition

Fracturing fluid composition is determined based on the type of fracturing, water characteristics, and geological properties of the target rock formation where access to trapped oil and gas reservoir is required. Fracturing fluids should possess four properties for ideal performance: Sufficient viscosity to create a fracture of adequate width, maximum fluid travel distance to increase fracture length, capability to transport large amounts of proppant into the fracture, and minimum gelling agent to allow easier degradation (Powell et al., 1999).

Fracturing fluid composition used in the upstream oil and gas industry varies widely from site to site and, in most cases, the exact composition is proprietary. However, in recent years, regulatory requirements were designed in Canada and the United States to enforce disclosure of fracturing fluid composition, and amount and source of chemical additives used by the industry (see for example Frac Focus, 2014).

Fracturing fluid is composed of mainly water and proppant as well as a small fraction of chemical additives. Some studies show that, typically, the fracturing fluid composition by volume is ~90% water, ~9.5% proppant, and ~0.5%-2% chemical additives (U.S. Department of Energy, 2009; American Petroleum Institute, 2010). Another study for the composition of two sample fracturing fluids shows that the composition by mass is 90.60% and 90.23% water, 8.96% and 9.11% proppant, and 0.44% and 0.65% chemical additives for Fayetteville Shale and Marcellus Shale, respectively (New York State Department of Environmental Conservation, 2011). The proppant is a small incompressible material used to keep the induced fractures open during and after the hydraulic fracturing operation. The proppants that are typically used in the industry are treated sand, ceramic pellets, or aluminium oxide.

The chemical additives used in the fracturing fluid vary considerably for each site and operator; however, typically between 3 to 12 chemical additives are used to prepare the fracturing fluid (U.S. Environmental Protection Agency, 2004; Arthur et al., 2008b; U.S. Department of Energy, 2009; Gomaa et al., 2011). Table 1.1 lists the most commonly used chemical additives in the fracturing fluids and the

purpose of each additive (American Petroleum Institute, 2010). However, some studies have identified about 750 different chemical additives used in hydraulic fracturing in the United States (Waxman et al., 2011; New York State Department of Environmental Conservation, 2011), some of which are known toxic chemicals (*e.g.* methanol, ethylene glycol, toluene) or carcinogens (*e.g.* benzene, naphthalene, acrylamide). Reviewing the list of these chemical additives is beyond the scope of the current study but public concern also exists over leakage of these chemicals into the underground sources of drinking water (U.S. Environmental Protection Agency, 2004).

Table 1.1: Typical chemical additives used in fracturing fluids

Chemical Additive	Purpose of Usage
Acids (i.e. Hydrochloric Acid and Formic Acid)	Helps dissolve minerals and initiate fissure in rock formation
Sodium Chloride	Allows a delayed breakdown of the gel polymer chains
Polyacrylamide	Minimizes the friction between fluid and pipe
Ethylene Glycol	Prevents scale deposits in the pipe
Borate Salts	Maintains fluid viscosity as temperature increases
Sodium/Potassium Carbonate	Maintains effectiveness of other components such as crosslinkers
Glutaraldehyde	Eliminates bacteria in the water
Guar Gum	Thickens the water to suspend the proppant
Citric Acid	Prevents precipitation of metal oxides
Isopropanol	Increases the viscosity of fracturing fluid

Although the fraction of chemical additives in the fracturing fluid may appear relatively small, the sheer volume of fracturing fluids used by the UOG industry makes the amount of chemical additives very significant. A recent study shows

that an estimated 3 billion litres (780 million US gallons) of chemical additives, not considering water and proppant, were used in fracturing operations between 2005 and 2009 in the United States only (Waxman et al., 2011).

1.2.2 Flaring with non-hydrocarbon droplets

After the hydraulic fracturing operation in a wellbore, the produced water along with oil and gas is brought to the surface. At an oil battery, the separation of produced water and solution gas from the oil takes place. Due to inefficiencies of the knock-out drums used for separation at oil battery sites, the separation process can potentially create scenarios where droplets of liquid can enter the solution gas flow directed to the flare stack for flaring (Strosher, 2000). The composition of this liquid is mostly similar to the produced water brought to the surface. It seems likely that the liquid droplets should be mainly composed of water with substances such as salt solutions (from brine) and other chemical additives from the fracturing fluid. A study on the fate and transport of fracturing fluids and their implications on produced water in two UOG sites in western and eastern U.S. shows that sodium chloride and other dissolved solids are the major constituents of the produced water; however, other fracturing chemicals are also present in the produced water (McElreath, 2011). It should be noted that the naturally-occurring concentrations of sodium and chloride from formation water rapidly dominated the concentrations of these compounds in tested fracturing fluids.

1.3 Objectives

To the authors' knowledge, there are currently no scientific data available that show what effect flaring these substances has on particle-phase emissions from

the flare. The main objective of the current study is to evaluate the potential effects of non-hydrocarbon liquids found in produced water and fracturing fluids on particulate matters emitted from a flare and the characteristics of these particles. The knowledge gap investigated in this study is to understand and evaluate the morphology, size and mass distributions, mass-mobility relationships, semi-volatile fraction of the particulate matter (PM), and PM emission factors.

Current recommended method for estimating soot from UOG flares are derived from data that is based on flaring landfill gas and is not applicable to open-atmosphere flames (Canadian Association of Petroleum Producers, 2007). UOG industry members in Canada report their emissions to the National Pollutant Release Inventory (NPRI) based on this method. This method is oversimplified and brings questions about the accuracy of current soot estimations from flares in Canada. By obtaining improved and relevant PM emission factors, the air emissions inventories can also be improved.

1.4 Outline of the thesis

This thesis consists of three further chapters. The investigation of particle emissions from a small-scale methane diffusion flame with injected droplets of distilled water, sodium chloride solution, and hydrochloric acid solution is presented in Chapter 2. The small-scale diffusion flame was set up at the University of Alberta and its purpose was to gain an understanding of the potential effects of mentioned non-hydrocarbon liquids on emissions from a diffusion flame. Size distributions of particulate emissions for two flame

conditions (*i.e.* non-sooty and sooty flames) are obtained in both unseeded and seeded cases. The effect of two liquid mass ratios on particle emissions is discussed and it is shown how changes in NaCl solution concentration relates to total particle mass concentration. Mass-mobility relationships, effective density functions, and volatility of particle emissions from unseeded and seeded flames are discussed in details later. Lastly, a brief discussion about composition of particulate matter (PM) emissions is presented.

The results from the small-scale experiment were used to help design a pilot-scale experiment. Chapter 3 presents the results of a pilot-scale investigation of particulate matter emissions from large diffusion flames with flow conditions and fuel composition typical of UOG flares in Alberta when droplets of distilled water, NaCl solution, and HCl solution were injected into the gas flow. This pilot-scale flare facility was at Carleton University. Morphology and size distributions of PM emissions from various diffusion flames (both unseeded and seeded with mentioned liquids) are discussed. Based on the mass-mobility relationships obtained from small-scale experiment, the mass emission factors measured by a scanning mobility particle sizer (SMPS) are discussed. Furthermore, mass emission factors measured by a laser-induced incandescence (LII) are compared with SMPS-measured emission factors. Effects of liquid mass ratio on particle mass emission factor are discussed in details later. Finally, number emission factors of particulate matter from studied flame conditions are obtained.

Chapter 4 presents a brief summary on major conclusions of the current study as well as recommendations for future works on this topic.

CHAPTER 2

Effects of Distilled Water, Sodium Chloride Solution, and Hydrochloric Acid Solution Droplets on Particle Emissions from a Co-flow Methane Diffusion Flame

2.1 Introduction

It is a common practice in the oil, gas, and petrochemical industries to dispose of undesired flammable gases by either flaring or venting. Venting is simply the release of these gases to the atmosphere, which is a major emission source particularly in the production of heavy oils when gas is released at the well-head (Clearstone Engineering Ltd., 2002). Flaring is the burning of unwanted combustible gases in an open-atmosphere flame. Methane is the major component of flared or vented gas in the petroleum industry. Flaring is preferred to simply venting the gases since the mass-based global warming potential of CO_2 is approximately 25 times lower than that of methane on a 100-year time horizon (IPCC, 2013). The U.S. Energy Information Administration (2013) estimated that

136.7 billion m^3 of gas was flared or vented worldwide in 2008. Other studies show that, by use of satellite data, the approximate amount of flare gases are 139 billion m^3 in the world annually Elvidge et al. (2009).

Fracturing fluids have been utilised successfully for many years in the petroleum industry for the purpose of increasing the extraction rates and recovery of oil and gas from reservoirs. This process is based on the injection of highly-pressurized fracturing fluid into the wellbore to induce fractures and cracks in rock layers, which increases permeability and enables access to oil and gas reservoirs that would be otherwise isolated from the well. Fracturing fluids usually contain a proppant to keep the induced hydraulic fracture open, after removal of the pressurized fracturing fluids. Fracturing fluids and proppants currently used in industry vary considerably in composition based on geological data of the well site, and their exact composition and formulation remain proprietary in most cases. Some studies showed that the major components of fracturing fluid are water, sodium chloride (which allows a delayed breakdown of the gel-polymer chains), and acids (mostly hydrochloric acid, which helps dissolve minerals and initiate fissure in the rock), and polymers (Arthur et al., 2008b; Gomaa et al., 2011; U.S. Environmental Protection Agency, 2004). A recent study revealed that in the United States, approximately 3 billion liters (780 million US gallons) of hydraulic fracturing products (*i.e.,* salt solutions and acids) have been used in fracturing operations between 2005 and 2009 (Waxman et al., 2011).

A possible scenario at oil battery sites (*i.e.,* facilities where produced oil is collected for primary separation before being sent to refineries) is that the

produced water after fracturing operation can enter the flare gas stream as droplets during the separation process and can be burned in the flare. The majority of the produced water is likely brackish water but hydraulic fracturing products may also be present. The main motivation behind the current study was to conduct a small-scale experiment to evaluate the potential effects of non-hydrocarbon liquids (particularly those found in the produced water and fracturing fluid) on particulate matter emitted from a small co-flow diffusion flame.

Other researchers have investigated combustion phenomenon, soot formation or suppression mechanisms within the flame, and emitted particles from diffusion flames with non-hydrocarbon liquid droplets (*cf.*, Cotton et al., 1971; Bulewicz et al., 1975; Ndubizu and Zinn, 1982; Bonczyk, 1983, 1987, 1988; Mitchell and Miller, 1989) or vapors (*cf.*, Schug et al., 1980; Rao and Bardon, 1984) added to various fuels. However, little work has been focused on determining the aerosol properties of the particle emissions from these flames. Therefore, the objective of the current study was to measure the particle size, mass, volatility, morphology, and elemental composition of the particulate emitted from a small laboratory flame during the combustion of methane with distilled water droplets, salt-water (sodium chloride solutions) droplets, and hydrochloric acid solution droplets.

2.2 Experimental Setup

The experimental setup is represented schematically in Figure 2.1. The setup consisted of a co-flow burner with liquid delivery and droplet generation system (bottom right), and a particle measurement suite comprised of a differential

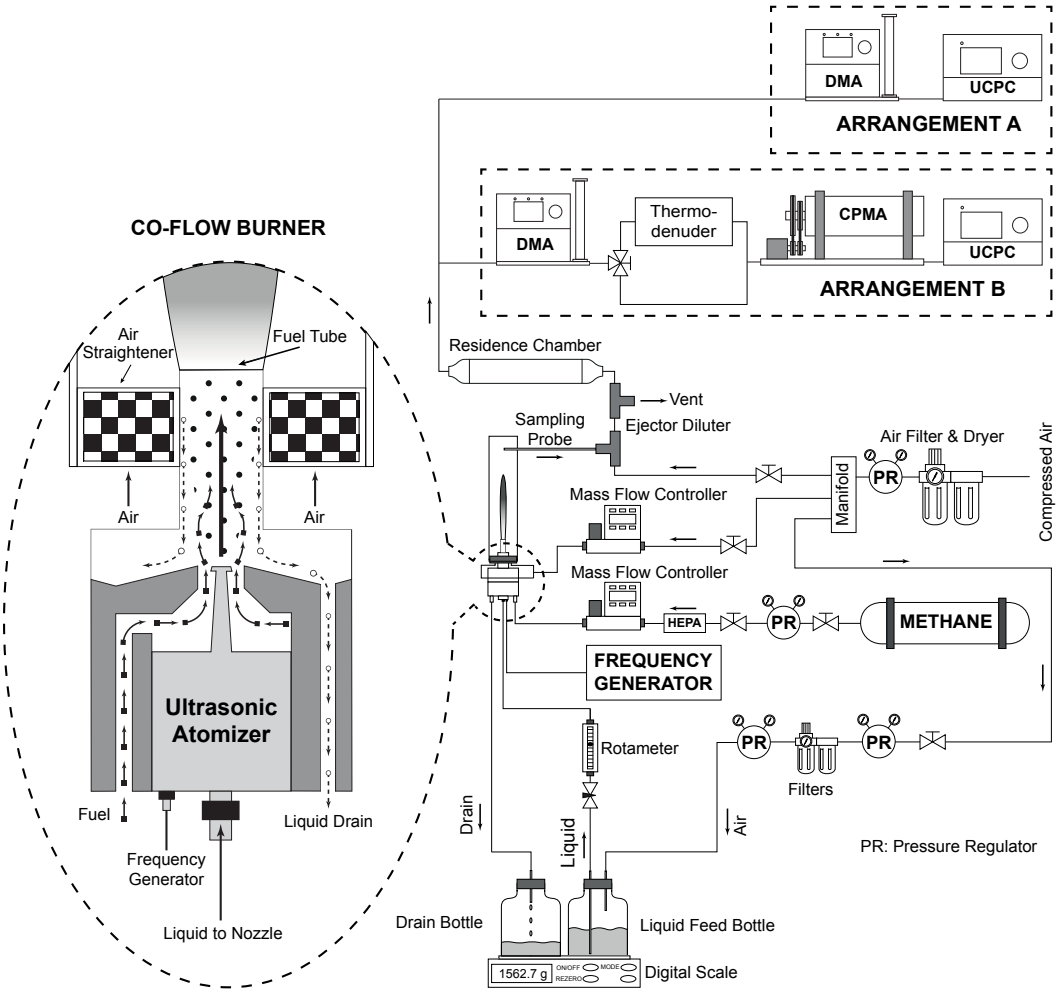

Figure 2.1: Schematic of the experimental setup with details of the co-flow burner

mobility analyzer (DMA), a condensation particle counter (CPC), a centrifugal particle mass analyzer (CPMA), and a thermo-denuder (top right).

2.2.1 Co-flow Burner

The burner (shown in detail in Figure 2.1 left) consisted of a round base with two fuel ports and two liquid-drain ports at the bottom, air straightener, and an ultrasonic atomizer. The ultrasonic atomizer attached to the base of the burner was used to introduce liquid droplets into the methane flow prior to combustion. The fuel tube (with inner diameter of 9.45 mm), which supplied the flame also

acted as a mixing chamber, where the methane stream and liquid droplets mixed. Air for combustion was provided through a co-flow arrangement consisting of an air straightener. A 72-mm diameter quartz tube was fitted around the air straightener, which prevented entrainment of ambient air. The compressed air used throughout the experiment was dry and filtered. The methane flow from the cylinder was also filtered by an in-line filter.

The methane and air flow rates were controlled by mass flow controllers (Cole-Parmer, model 32907-67 and Omega, model FMA-2608A, respectively). Two flow conditions were considered. For condition 1, the methane and air mass flow rates were 0.30 SLPM (standard litres per minute at 1 atm and 25°C) and 13.40 SLPM, respectively, and the flame had an average length of 70 mm. For condition 2, the methane and air flow rates were 0.80 SLPM and 8.00 SLPM, respectively, and the flame had an average length of 200 mm. The condition 2 exceeded the smoke point of the flame and produced higher amounts of soot in the exhaust stream. Furthermore, flame condition 1 was visually non-flickering while flame condition 2 was flickering randomly. Throughout this study, we will call flame condition 1 the “non-sooty flame” and flame condition 2 as the “sooty flame”.

The ultrasonic atomizer (Sono-Tek Corp., Model 06-04022) had a flat tip nozzle with cylindrical spray pattern and was equipped with a broadband ultrasonic generator (Model 06-05108). Operating at the frequency of 120 kHz, the atomizer nozzle could deliver a distribution of droplets with count median diameter (CMD) equal to 19 μm and geometric standard deviation (GSD) of 1.84 according to the

manufacturer's specifications. A portion of the liquid droplets that did not exit the fuel tube with the fuel was drained back to a bottle via drain ports at the bottom of the burner base. The mass of liquid in the feed and drain bottles were measured simultaneously as a function of time using a digital scale to measure the net liquid flow rate exiting the top of the fuel tube into the flame. Two different liquid flow rates were considered for this study. In the case of the lower liquid flow rate, the liquid input flow rate was set at 2.21 mL/min and steady-state tests showed that approximately 0.132 mL/min (or ~6%) of the liquid droplets exited the fuel tube into the flame zone. However, in the case of higher liquid flow rate, the liquid input flow rate was set at 4.60 mL/min and approximately 0.180 mL/min (or ~4%) of the liquid exited the fuel tube into the flame at steady state.

2.2.2 Aerosol Measurement

Figure 2.1 also shows the instrumentation used to study the properties of particles from the diffusion flame. Aerosol sample was collected ~150 mm above the tip of the flame (tests were conducted to show that the resulting particles were independent of radial position across the quartz tube) by a 305-mm long stainless steel sampling probe (I.D. 4.6 mm) and was then diluted by an ejector diluter with a dilution ratio of 10:1 to reduce particle concentration for the instruments and prevent water condensation. The probe had a residence time of ~1 s and, therefore, the effect of coagulation in the probe was negligible. The diffusion loss for ~100 nm particles in the probe was ~1.5%; however, the temperatures of the wall of the probe and the sample flow in the probe were assumed to be equal at steady state and, therefore, thermophoretic loss was neglected. The diluted aerosol

sample was sent to a cylindrical residence chamber with a 60 s residence time to reduce the fluctuation in the particle number concentration because SMPS needed a stable aerosol input due to its time-response limit. The extent of particle-particle coagulation in the residence chamber varied significantly. Considering an average coagulation coefficient for a log-normal distribution of polydisperse particles, when particle concentration in the residence chamber was 10^6 cm^{-3} and 10^7 cm^{-3} (sooty flame without and with NaCl solution, respectively), ~10% and ~38% of the number of particles would be expected to coagulate, respectively; however, when particle concentration in the residence chamber was below 10^5 cm^{-3} (*e.g.* sooty flame with distilled water or HCl solution), less than 1% of particles coagulated and, therefore, coagulation was negligible. Consequently, particle size distributions of the sooty flame without and with NaCl solution would be smaller particles with higher number concentrations in the absence of the residence chamber.

A scanning mobility particle sizer (SMPS) which consisted of the DMA (TSI Inc., Model 3081) and the CPC (TSI Inc., model 3776) was used to measure the particle size distribution (Arrangement A in the Figure 2.1). The measurement range of the SMPS was 15 to 661 nm when the aerosol and the sheath air flow rates were 0.30 SLPM and 3.00 SLPM, respectively. A smaller measurement range of the SMPS equal to 6 to 229 nm was obtained when the aerosol and the sheath air flow rates were 1.50 SLPM and 15.0 SLPM, respectively.

A thermodenuder similar to the one used by Ghazi and Olfert (2013) was used in this study to investigate the volatility of particles. It consisted of a long piece of

copper tubing where the aerosol sample was first heated up to 200°C in the heating section and then cooled down to room temperature in the cooling section. This procedure led to the condensation of any volatile material on the inner wall of the tubing. The thermodenuder also had a bypass tube with the same residence time (~6 s) as the denuding tube to match the effects of coagulation or diffusion on the two sampling procedures.

Arrangement B in Figure 2.1 was used to determine the mass-mobility relationship of particles as well as to study the volatility of emitted particles in terms of their mass. The diluted aerosol sample was drawn into the DMA which was set to a desired mobility diameter (*e.g.,* 100 nm). The mobility-classified particles were sent to the thermodenuder (or bypassed). Particles then entered the CPMA (Cambustion Ltd.) which determined their mass (for singly charged particles), by stepping its voltage and rotational speed and counting the particles with the CPC (Olfert et al., 2006). The transfer function resolution was set to 10 throughout this study (where the resolution is defined as the particle mass at the maximum of the CPMA transfer function divided by the full width half maximum of the transfer function).

Elemental composition of the particle phase of emissions was determined by X-ray photoelectron spectroscopy (XPS). Particle emissions were collected above the flame on 6 mm diameter porous titanium frits (Applied Porous Technologies Inc.) by means of a vacuum pump. Samples were then analyzed by high energy-resolution XPS Axis Ultra (Kratos Analytical Ltd.) for determination of elemental composition.

2.3 Results and Discussion

Experiments were performed to evaluate the effects of entrained droplets of distilled water, sodium chloride solutions, and a hydrochloric acid solution on particulate matter emissions of the co-flow diffusion flames for the aforementioned methane and liquid flow conditions.

2.3.1 Effect of liquid droplets on the particle size distribution of the non-sooty flame

Figure 2.2 shows the particle size distributions measured by the SMPS for the non-sooty flame (base case) and when liquid droplets of distilled water and NaCl

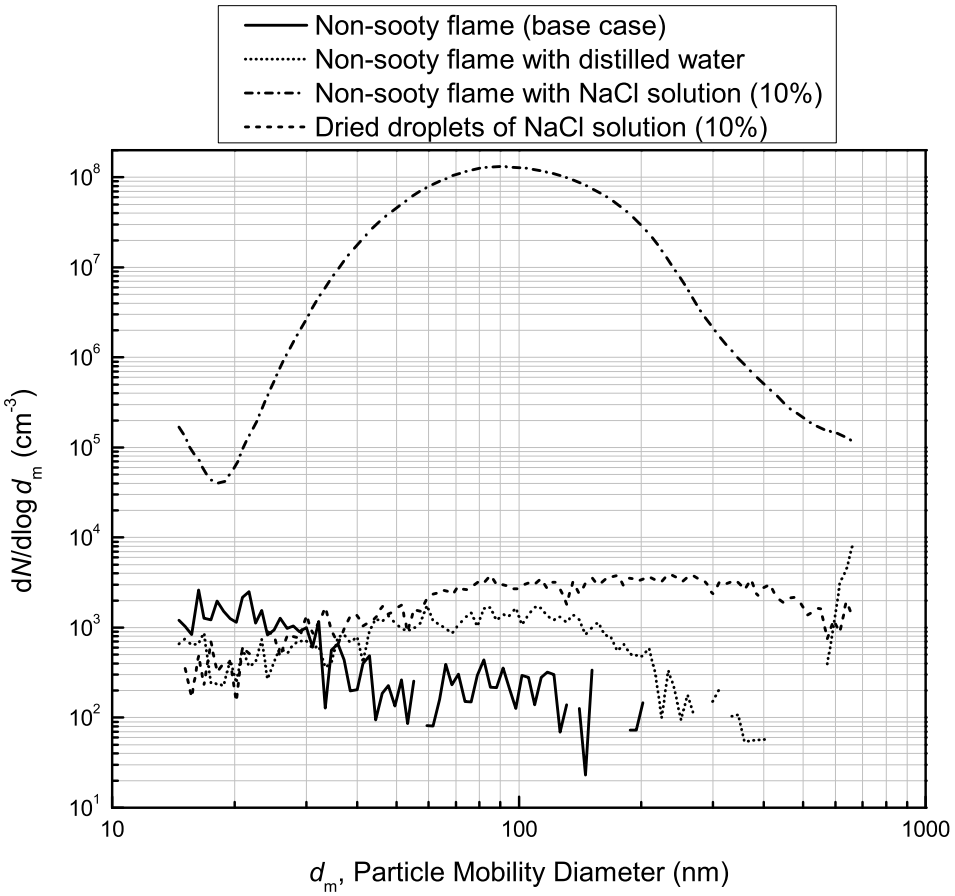

Figure 2.2: Particle size distribution for non-sooty flame with droplets of distilled water and sodium chloride solution (10%). Net liquid flow rate of 0.180 mL/min

solution were injected into the fuel stream. The net liquid flow rate of 0.180 mL/min was used in all cases. Where the distribution line is not shown, it should be interpreted that no particles of that particular size were detected, since the logarithm of zero is not defined.

The particle concentrations in the base case and the case with distilled water were extremely small and the size distributions resembled a noisy response rather than a log-normal distribution typical for soot particles. The air and methane flow rates used in the non-sooty flame provided combustion conditions with 22 times more oxygen available than that required for stoichiometric combustion. Therefore, the non-sooty flame produced very few soot particles. Moreover, the distilled water droplets contain very little dissolved substances; therefore, low levels of particulate matter were expected when these droplets were combusted in the diffusion flame.

The NaCl solution droplets were composed of an aqueous solution of 10% sodium chloride by mass (w_{NaCl} = 0.10). Spraying droplets of sodium chloride solution into the diffusion flame affected its luminosity, giving the flame a bright yellow appearance, which resembled the characteristic colour of sodium in the flame. In this case, the particle size distribution shows a total particulate number concentration that is approximately 5 orders of magnitude higher than the flame without any liquid added. It is important to realize that the particles measured with the SMPS were not simply dried NaCl/water droplets passing through the diffusion flame. Figure A.1 in Appendix A shows the expected frequency distribution of the atomized droplets and the expected dried NaCl particle

frequency distribution. If the droplets of sodium chloride solution were simply dried, then the vast majority of the dried particles should be greater than 1 μm with expected median diameter of 7 μm. Presumably, the small dried NaCl particle concentration measured with the SMPS in Figure 2.2 (for the case of injected sodium chloride solution without the flame present) is simply the left-hand tail of the distribution predicted in Figure A.1. Therefore, the high particle concentration measured when droplets of sodium chloride solution were passed through the flame can be attributed to the generation of new particles and not simply dried droplets. The mechanism for this new particle generation is not completely known. It is possible that the high flame temperatures cause the droplets of sodium chloride solution to evaporate (NaCl has a boiling point of 1413°C) and then nucleate to form a higher number of smaller particles.

2.3.2 Effect of liquid droplets on the particle size distribution of the sooty flame

Figure 2.3 shows particle size distributions for the sooty flame (higher methane flow rate) with and without entrained droplets (net liquid flow rate of 0.180 mL/min). The sooty flame produced total particulate number concentrations more than 4 orders of magnitude higher than the non-sooty flame condition.

The presence of distilled water droplets in the sooty diffusion flame had a significant effect on the reduction of particulate matter emissions. This result is in agreement with the qualitative results by Rao and Bardon (1984) where the soot concentration from a laminar diffusion flame collected on filter reduced as the mole fraction of water in fuel increased when the fuels were diesel, toluene and benzene. Rao and Bardon (1984) also concluded that suppression of soot particles

due to the addition of water vapour is mainly a thermal effect and this same thermal effect can be seen in the pyrolysis of methane towards the formation of acetylene (Holmen et al., 1976), which can be a precursor to soot. Schug et al. (1980) obtained a similar qualitative result in the decrease in sooting tendency in an ethylene diffusion flame by addition of water vapour as a diluent. They concluded that water vapour could act as a heat sink where its specific heat capacity is an important parameter in determining the reduction of soot formation compared to other additive diluents. Schug et al. (1980) also concluded that water vapour has primarily a thermal effect on the flame and chemical reactions

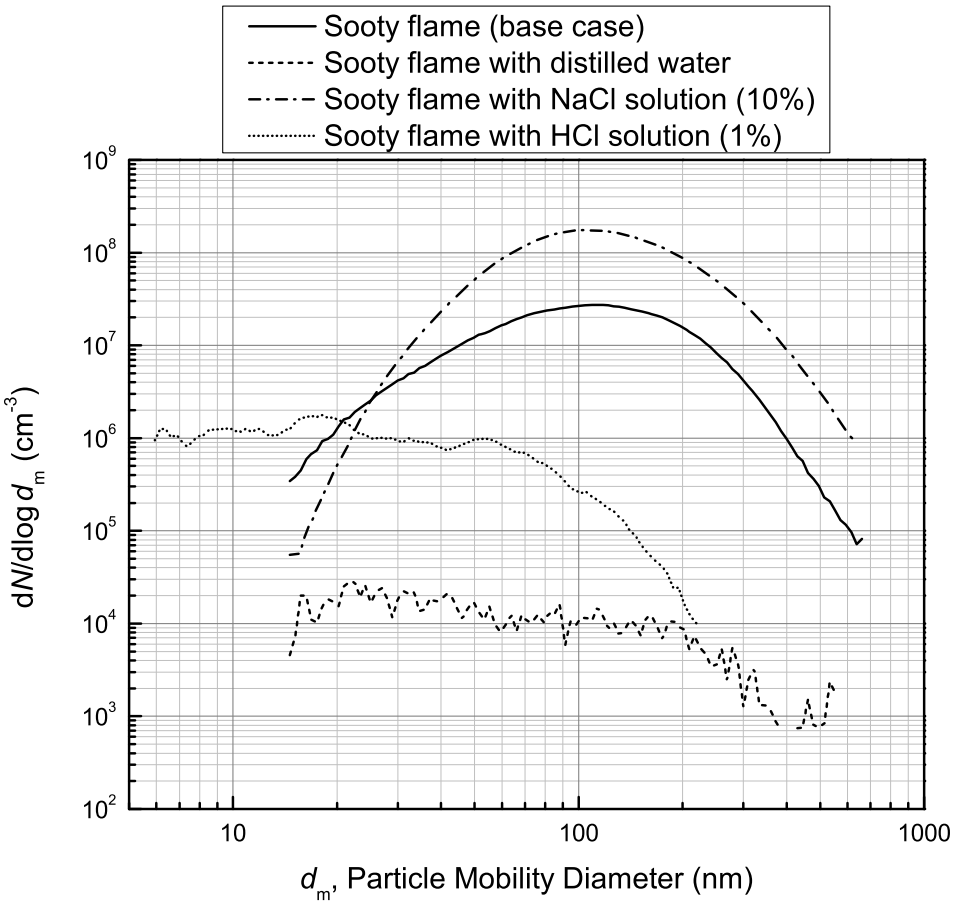

Figure 2.3: Particle size distribution for the sooty flame with droplets of distilled water, NaCl solution (10%), and HCl solution (1%). Net liquid flow rate of 0.180 mL/min

involving the additive have a negligible influence on the soot precursors.

As before, the sodium chloride solution had a 10% NaCl mass fraction ($w_{NaCl} = 0.10$). The effect of droplets with NaCl in the sooty flame is interesting as combustion was quite different when such droplets are present in the flame. The total number concentration of particulate matter emissions was increased by a factor of 5.6 when droplets with NaCl were injected into the sooty flame. However, the particles emitted at this flame condition did not visually appear to be soot. Specifically, these particles were dominantly white in colour and appeared to be salt (*i.e.,* sodium chloride). More detailed discussion regarding composition is presented in section 3.5. However, from the composition analysis used in the current study, it is not possible to quantify soot and NaCl particles in this case. Previous studies by other researchers, discussed in more details below, suggest that NaCl solution would suppress soot formation in diffusion flames. Therefore, the increase in the particle emission of the sooty flame with droplets of NaCl solution, could be due to newly generated sodium chloride particles (as before, presumably due to the nucleation of NaCl in the post-flame region).

Besides the same thermal effects, which are seen with distilled water droplets, other researchers have introduced possible chemical effects to impair soot production. Bonczyk (1983, 1988) studied the effects of nebulized aqueous solution of alkali salts (including NaCl) on sooting propane and ethylene diffusion flames, respectively. He used the ionic theory of soot formation to show that alkali metal ionization causes a reduction in the soot precursors and soot formation. Bulewicz et al. (1975) also reported a slight reduction in soot

collection rate from acetylene and propane diffusion flames when seeded with sodium chloride solution. Some researchers have suggested that the reduction in soot in the presence of droplets of alkali salt solution is due to the formation of smaller soot particles in the flame which are more susceptible to rapid oxidation (Haynes et al., 1979; Mitchell and Miller, 1989).

Figure 2.3 also shows the particle size distribution for the sooty flame with droplets of hydrochloric acid solution. The concentration of this solution was selected as 1% (mass-based), which is representative of acid concentration in fracturing fluids. Only in this case, the SMPS settings for sample and sheath air flow rates were changed to 0.15 SLPM and 1.50 SLPM, respectively, to obtain size distribution for particles smaller than 15 nm. The total number concentration of particles emitted by the sooty flame with hydrochloric acid solution was 19 times less than the particles generated by the sooty flame. The reduction in soot emission can be attributed to the thermal effects of the water in the droplets. However, the HCl droplets did not reduce the soot emission to the same level as the distilled water droplets at a similar liquid flow rate.

Appendix A.2 also contains particle size distributions for the same sooty flame but with a lower liquid flow rate of 0.132 mL/min. This small drop in liquid flow rate had a small effect in the size distributions of particles emitted from the flame when NaCl and HCl droplets were added. However, the liquid flow rate did have a relatively significant effect on soot suppression for the flame with distilled water droplets. The lower liquid flow rate of water droplets produced approximately 7 times more particulate (in terms of number) than the higher flow rate.

2.3.3 Effect of solution concentration on the particle size distribution of the sooty flame

The effect of various sodium chloride concentrations was investigated by atomizing 10%, 3%, and 1% mass-based NaCl solutions (w_{NaCl} = 0.10, 0.03, and 0.01, respectively) into the sooty flame. The higher net liquid flow rate of 0.180 mL/min was used and the results are shown in Figure 2.4. As sodium chloride mass was decreased in the solution, the total particle concentration also decreased and smaller particles were generated. These results can be explained by the fact that when NaCl concentration is decreased, less sodium chloride was available in

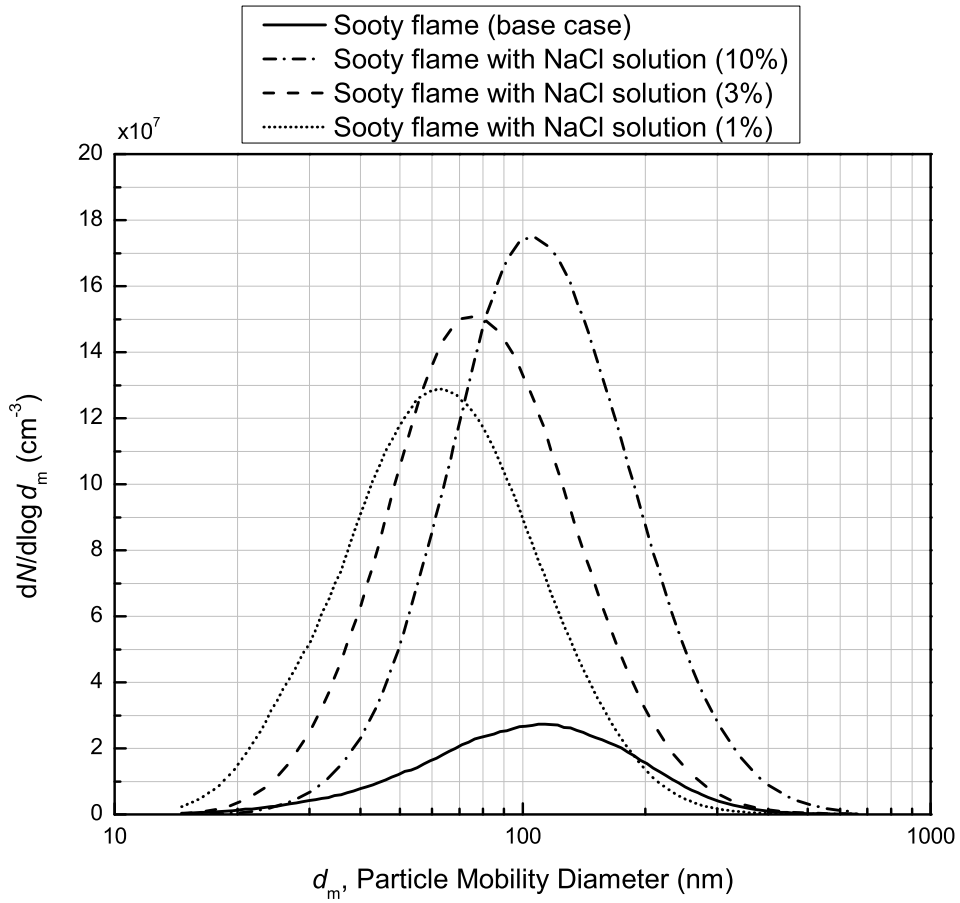

Figure 2.4. Particle size distribution for sooty flame with various NaCl concentrations

the droplets to nucleate in the flame and generated smaller particles in smaller number.

Mass distribution and total mass concentration of particles in each case were obtained from the mass-mobility relationship for undenuded particles from the sooty flame with NaCl droplets (see section 3.4). Total mass concentration of particles for the cases of 10%, 3%, and 1% salt water in the sooty flame was 390 ± 80.3 mg/m^3, 135 ± 20.7 mg/m^3, and 64.8 ± 13 mg/m^3, respectively. This shows that, considering the uncertainty, the ratio of total particle mass concentration was roughly similar to the ratio of sodium chloride mass fractions in each solution, which may be useful in predicting particle emissions when other NaCl solution concentrations are passed through the flame.

2.3.4 Mass-Mobility Measurement and Volatility Study of Particulate Matter

The mass-mobility exponent (D_m) has been defined as

$$m = k d_\mathrm{m}^{D_\mathrm{m}} , \tag{2.1}$$

where m is the particle mass, d_m is the mobility diameter, and k is a constant (*e.g.* Park et al., 2003). Arrangement B of the experimental setup was used to determine the mass-mobility relationship of particles, as well as to determine the mass fraction of volatile material on the particles. Figures A.6–A.8 in Appendix A show the mass-mobility plot of particles from the base case sooty flame, sooty flame with sodium chloride solution ($w_\mathrm{NaCl} = 0.10$), and sooty flame with hydrochloric acid solution ($w_\mathrm{HCl} = 0.01$), respectively.

The particle effective density (ρ_{eff}) is defined as the true mass of the particle divided by the volume of a spherical particle which has the same mobility diameter (McMurry et al., 2002). Therefore, by substituting the mass from Equation (2.1), the effective density is,

$$\rho_{\text{eff}} = \frac{m}{\frac{\pi}{6} d_{\text{m}}^3} = \frac{6}{\pi} k d_{\text{m}}^{D_{\text{m}}-3}, \tag{2.2}$$

which shows that for fractal-like soot, the effective density generally decreases as the mobility diameter increases because mass-mobility exponent is typically less than 3 as shown in Figures A.6–A.8. Effective density is an important factor for particle transport properties, as well as in finding the relationship between aerodynamic diameter and mobility diameter. Figures 2.5a-2.5c show the effective density-mobility relationship for the same three cases of flames mentioned above. The effective density equation was determined by fitting the data points with the power law function by χ-square minimization. The 95% confidence interval errors in both the exponent and the constant are also given.

Figure 2.5a shows that the effective density of particles emitted from the sooty flame varies between 1040 kg/m^3 for small particles (30 nm) to 160 kg/m^3 for large particles (400 nm). The mass-mobility exponent was 2.27 ± 0.03 for undenuded (fresh) particles. This result is very typical of soot particles generated from a diffusion flame and consistent with previous studies in the literature. For a propane diffusion flame with high and low air-to-fuel ratio, Rissler et al. (2013) reported the mass-mobility exponent equal to 2.41 and 2.28, respectively. Maricq

and Xu (2004) reported a mass-mobility exponent equal to 2.15 ± 0.10 for premixed ethylene flame soot. For a McKenna burner with equivalence ratio of $\Phi = 2.0$, the mass-mobility exponent was reported equal to 2.24 ± 0.03 by Cross et al. (2010) and equal to 2.19 by Ghazi et al. (2013). Figure 2.6 shows the mass fraction of volatile material on the emitted particles from the sooty flame without and with droplets of NaCl and HCl solutions. The mass fraction of volatile material is defined as the ratio of volatile mass to the mass of undenuded particle, *i.e.* $(m_{\text{undenuded}} - m_{\text{denuded}})/m_{\text{undenuded.}}$ Figure 2.6 shows that there was very little (less than 7%) or no volatile material on the soot particles from the sooty flame.

Figure 2.5b shows that the effective density of undenuded particles from the sooty flame with droplets of sodium chloride solution (w_{NaCl} = 0.10) was between ~2100 kg/m^3 for small particles to ~1650 kg/m^3 for large particles. The material density of sodium chloride is ~2160 kg/m^3. The mass-mobility exponent was 2.89 ± 0.02 for undenuded particles. The mass-mobility exponent of a spherical particle is 3; therefore, the emitted particles are not aggregated and rather have a compact structure. Also, it is evident from Figure 2.6 that there was little or no volatile coating on the particles. For particles with a mobility diameter greater than 260 nm, it was observed that the CPMA mass spectrum was skewed to the left-hand side, which appears to be a superposition of two log-normal distributions (shown in section A.4 in Appendix A). CPMA mass spectrum is typically a narrow log-normal distribution with a dominant peak for singly-charged particles and much smaller peaks on the right side for multiply-charged particles. The fact that a smaller secondary peak appears to the left-hand side of

the dominant peak indicates that particles of different composition or coagulated NaCl-soot or soot-soot particles exist at large mobility diameters. Figure 2.5b also shows a case where a sodium chloride solution was atomized (using TSI model 3076 atomizer) and measured by the same DMA-CPMA system. The figure shows the effective density of the atomized solution agrees well with the particles exiting the flame. Therefore, it seems that the dominant peak of CPMA mass spectrum is composed of sodium chloride and the left-hand peak is comprised of a particle with a lower effective density (~1400 kg/m^3) which is much higher than a typical fractal-like soot particle. Therefore, these particles may be an internal mixture of soot and NaCl or coagulated particles of same or different species (*i.e.* NaCl and soot).

Figure 2.5c shows the effective density of particles emitted from the sooty flame with droplets of hydrochloric acid solution (w_{HCl} = 0.01). Figure 2.6 shows the presence of volatile coating on the solid component of the particle. The mass fraction of volatile material is dependent on particle size and approximately 30% of the mass of an undenuded particle with mobility diameter of 30 nm was volatile material. Mass fraction of volatile material decreased below 10% as the particle mobility diameter was increased. The undenuded particles had a mass-mobility exponent of 2.14 ± 0.02, which is lower than the mass-mobility exponent of the sooty flame. Presumably particles from the sooty flame with HCl droplets were composed of an internal mixture of soot particle with condensed volatile material filled its open structure. The higher volatile mass fraction at lower

particle sizes increases the effective density at lower particle sizes and thus reduces the mass-mobility exponent.

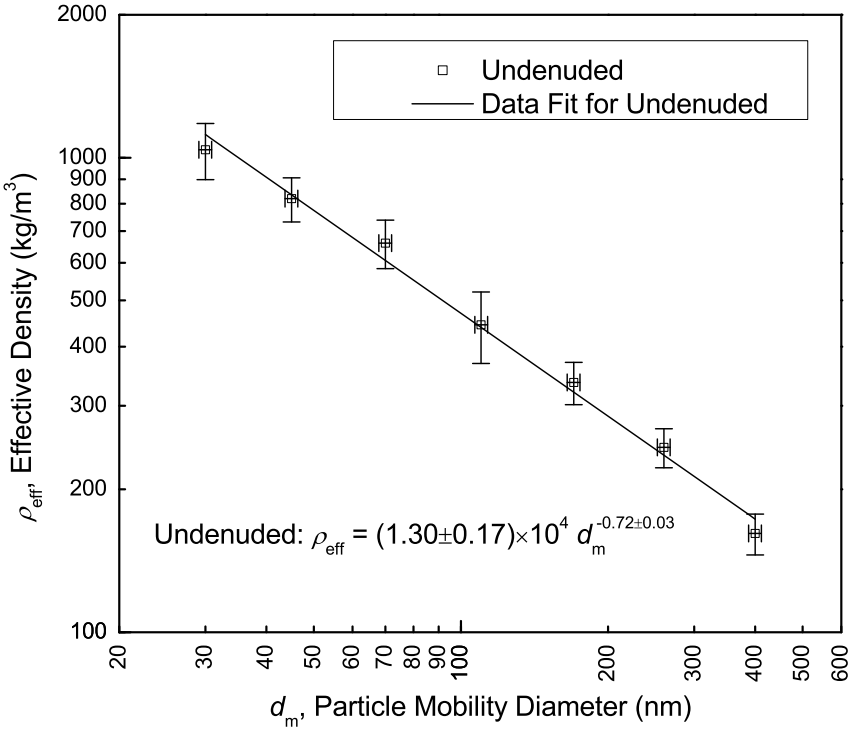

(a)

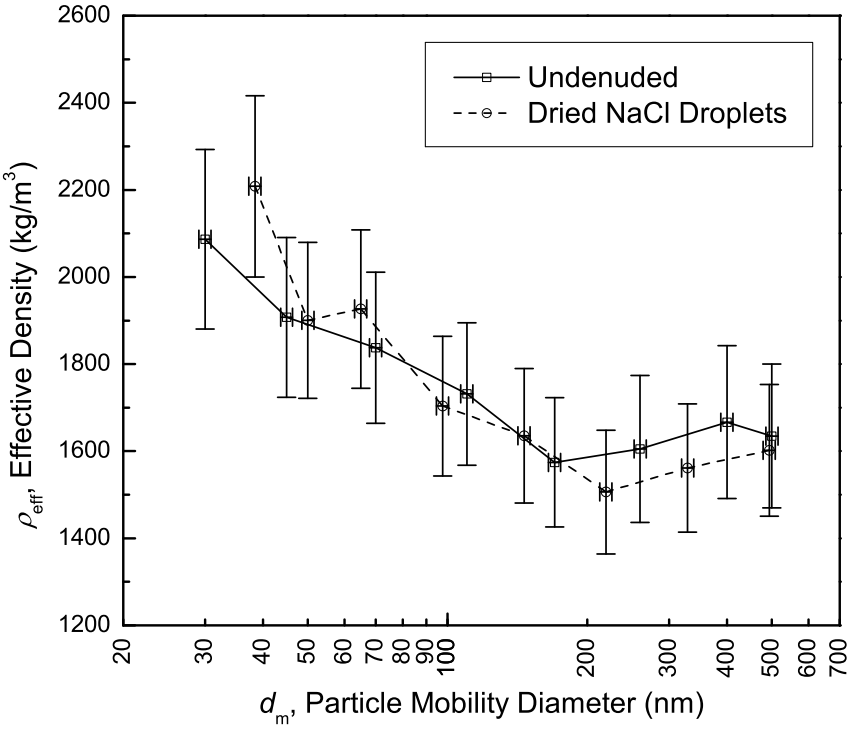

(b)

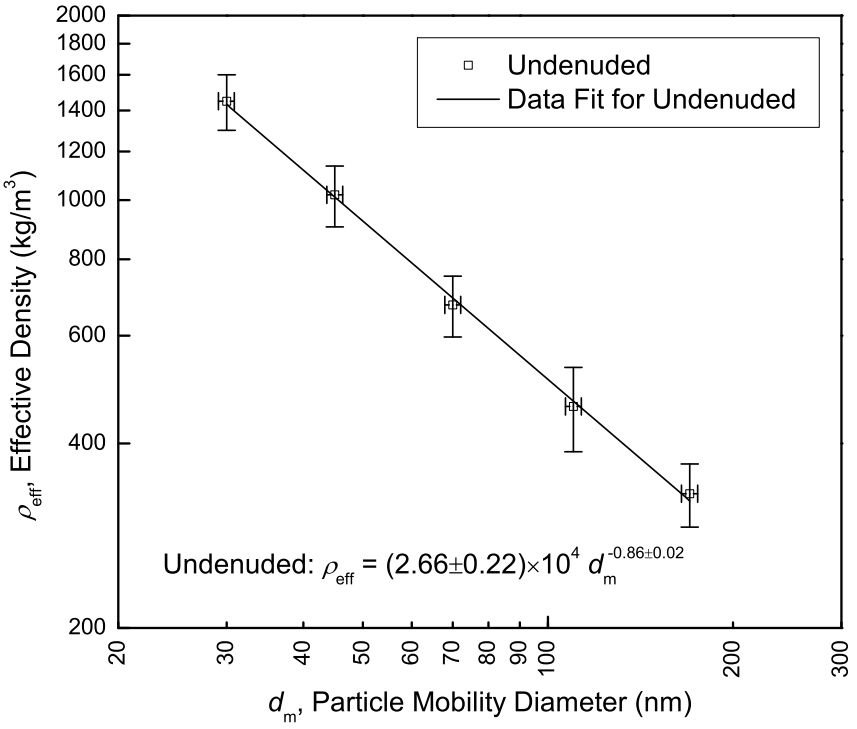

(c)

Figure 2.5. Effective density of particles from sooty flame (a) without liquid droplets, (b) with sodium chloride solution (10%), and (c) with hydrochloric acid solution (1%)

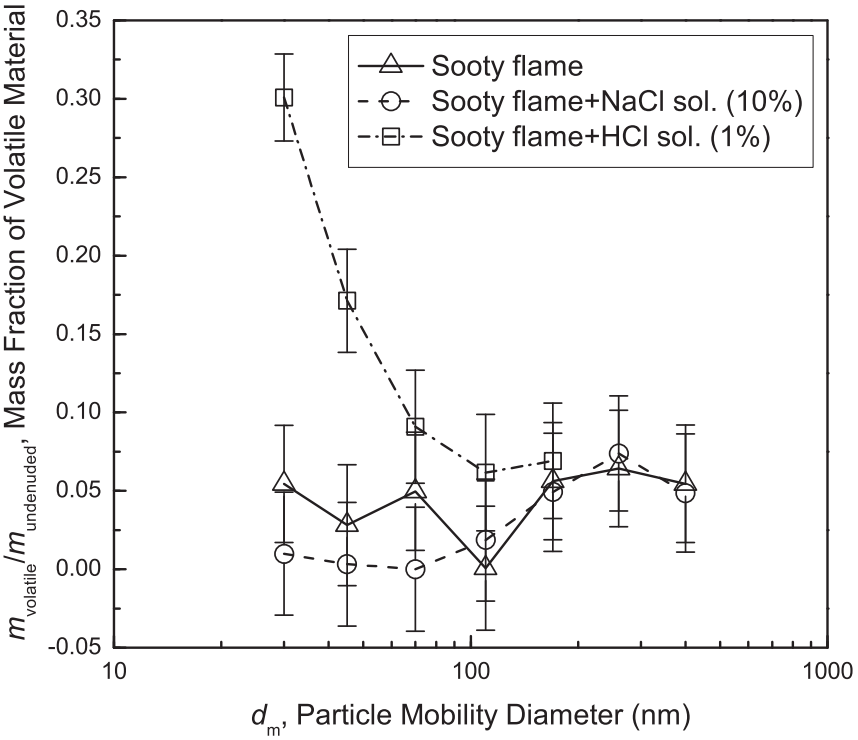

Figure 2.6. Mass fraction of volatile material on particles from a sooty flame without and with droplets of sodium chloride solution (10%) and hydrochloric acid solution (1%)

2.3.5 X-ray Photoelectron Spectroscopy of Particulate Matter

In this study, XPS was used to obtain a low-resolution wide-scan (survey) spectrum to determine the elemental composition of the particulate matter from the sooty flame and the sooty flame with droplets of NaCl solution ($w_{NaCl} = 0.10$). In a typical XPS survey scan, each major peak in binding energy corresponds to a certain electron orbital of a specific element. Peaks arising from secondary Auger electrons are specified by standard KL format.

Figure 2.7 shows the XPS spectrum obtained from the sooty flame and sooty flame with droplets of NaCl. (Samples of the sooty flame with either droplets of distilled water or HCl solution were not sufficient for reliable XPS analysis.) In the case of the sooty flame (Figure 2.7a), the majority of particles were composed of elemental carbon (in the form of soot). The small peak of oxygen is typical in XPS analysis and indicates contamination by surface oxygen.

For a sooty flame with droplets of NaCl (Figure 2.7b), major peaks corresponding to sodium and chlorine atoms could be observed. In this case, some chlorine atoms reacted with sodium atoms to form solid sodium chloride in agreement with the physical properties of these particles explained in earlier sections. The smaller peak of oxygen indicates contamination which is common in XPS analysis. The carbon peak is probably due to contamination or soot. Moreover, it should be noted that the observed NaCl and carbon cannot be quantified in this technique due to the effects of surface contamination typical for XPS results.

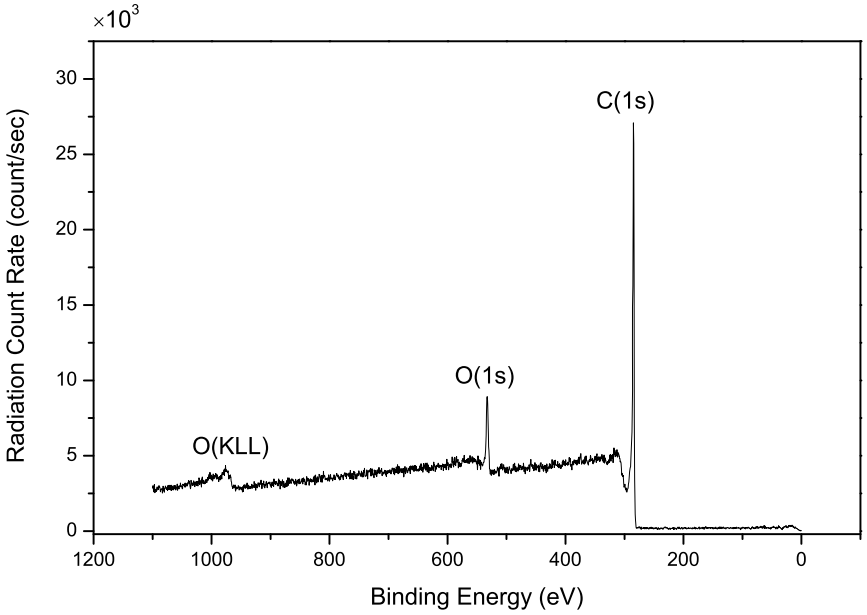

(a)

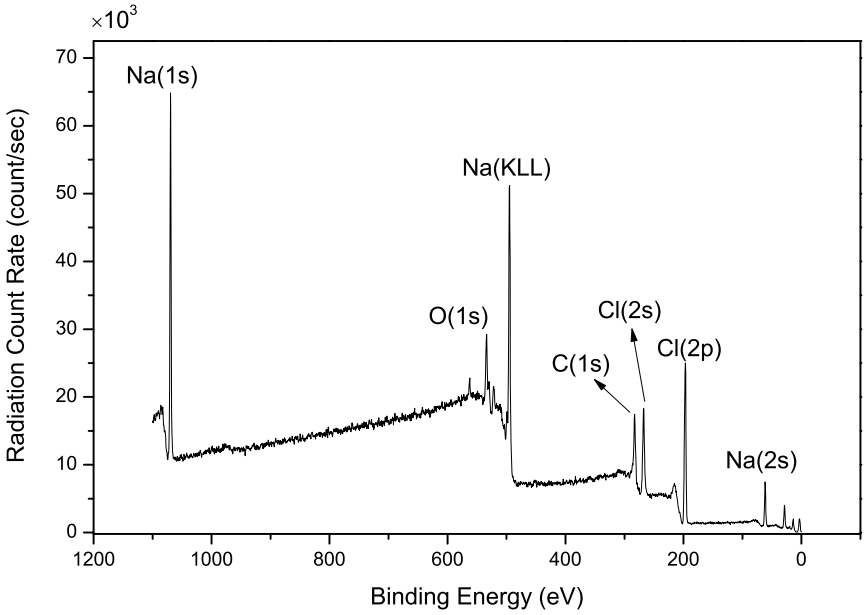

(b)

Figure 2.7. The XPS spectrum for (a) sooty flame, and (b) sooty flame with droplets of NaCl solution

2.4 Conclusion

The size distributions of particulate matter from a co-flow diffusion flame without and with injected droplets of distilled water, sodium chloride solution, and

hydrochloric acid solution were measured by DMA and CPC. For the non-sooty flame without and with distilled water droplets, total number concentrations of particles were very low; however, with droplets of sodium chloride solution a large concentration of particles were generated. For the sooty flame, the effect of distilled water and hydrochloric acid solution was to suppress particle number concentration by a factor of 0.001 and 0.05, respectively, compared to the base case. However, a sodium chloride solution of 10% by mass increased the particle number concentration by a factor of ~6. Lower concentrations of NaCl solution resulted in an approximately proportional reduction in the particulate mass concentration. The potential effects of sodium chloride solution on the particulate matter emission from both flames are complex, but these results suggest that the majority of the particulate matter emission is physically and elementally very similar to sodium chloride. Future work will attempt to quantify the proportional of the sodium chloride.

Thermodenuder, DMA-CPMA, and XPS analysis provided insight into the composition and mixing state of the particles. The results show that the particles from the sooty flame were primarily elemental carbon without any detectable amounts of condensed volatile material. The mass-mobility exponent of the particulate from this flame was also in agreement with typical fractal-like soot agglomerates. DMA-CPMA results suggested that the particles from the sooty flame with droplets of NaCl solution were predominately composed of pure NaCl particles with a smaller contribution of particles with a lower effective density (~1400 kg/m^3). The particles with lower effective density could be internal

mixtures of elemental carbon and NaCl or merely the coagulated particles of same or different species (NaCl or soot). DMA-CPMA results also showed that the particles from the sooty flame with HCl droplets were predominately composed of fractal-like soot internally mixed with a small amount of condensed volatile material.

CHAPTER 3

Effects of Distilled Water, Sodium Chloride Solution, and Hydrochloric Acid Solution on Particulate Emission of Flares

3.1 Introduction

In the oil and gas industry, it is common practice to burn off undesired flammable gases (*e.g.,* solution gas, sour gas, gases released during emergencies at a facility, etc.) in an open-atmosphere flame, which is a process known as flaring. Alternatively, unwanted gases may be simply released into the atmosphere, a process known as venting. Although the composition of flared gas of the upstream energy industry varies significantly from site to site, the main component is methane. The potential global warming of methane is ~25 times higher than carbon dioxide on a mass basis on a 100-year time-scale (Intergovernmental Panel on Climate Change, 2013). Therefore, flaring is often preferred over venting to mitigate greenhouse gas emissions. It is estimated, by use of satellite imagery,

that approximately 139 billion m^3 of gas is flared in the world annually (Elvidge et al., 2009). Other sources estimated that the amount of gas that was flared or vented globally in 2008 was 136.7 billion m^3 (U.S. Energy Information Administration, 2013).

Although flaring can reduce the greenhouse gas emissions compared to venting, it still has negative impacts on air quality due to the production of soot and other pollutants (Pohl et al., 1986; Johnson and Kostiuk, 2000; Strosher, 2000; JohnsonWilson et al., 2001). Soot has serious effects on human health and is linked to a variety of adverse health complications (U.S. Environmental Protection Agency, 2009). Soot has also been identified as a significant contributor to global warming (Hansen et al., 2000; Ramanathan and Carmichael, 2008; Intergovernmental Panel on Climate Change, 2013).

Fracturing fluids are used in the upstream oil and gas (UOG) industry to increase the extraction rates of oil and gas from reservoirs. Highly-pressurized fracturing fluid is injected into the wellbore to create cracks in rock layers, which provides access to oil and gas reservoirs that are trapped between the rock layers and are isolated from the well. Fracturing fluids currently used in the UOG industry have a wide range of composition based on geological data of the well site. The exact formulation of these fracturing fluids mostly remains proprietary. Some studies revealed that the main constituent of a fracturing fluid is water, with a wide range of chemical additive such as sodium chloride, acids (mostly hydrochloric acid), and polymers (U.S. Environmental Protection Agency, 2004; Arthur et al., 2008b; Gomaa et al., 2011; Waxman et al., 2011; New York State Department of

Environmental Conservation, 2011). The amount of chemicals (except water) used in hydraulic fracturing operations is significant and estimated to be 3 million m^3 (780 million US gallons) between 2005 and 2009 in the United States only (Waxman et al., 2011).

A possible scenario at oil-field battery sites is that during the separation process in the knock-out drum, droplets of produced water after fracturing operations and/or liquid hydrocarbons can enter the flare stream and combust in the flame (Strosher, 2000). Chemical analysis of the produced formation water following the hydraulic fracturing at two UOG sites in Eastern and Western U.S. showed that sodium chloride was the major constituent of non-hydrocarbon liquid; however, other fracturing chemicals were also present (McElreath, 2011).

Some researchers have investigated flare emissions by quantifying gas-phase carbon conversion efficiency (Siegel, 1980; Pohl et al., 1986; Johnson and Kostiuk, 2000; Kostiuk et al., 2000; Strosher, 2000; Johnson et al., 2001; Johnson and Kostiuk, 2002; Kostiuk et al., 2004). A few other researchers have studied and measured soot emissions from flares (McDaniel, 1983; Pohl et al., 1986; Johnson et al., 2010; Johnson et al., 2011; McEwen and Johnson, 2012; Devillers et al., 2012; Johnson et al., 2013). Siegel (1980) used a commercial flare with refinery relief gas (which contained 55% hydrogen on average) in his study but he could not determine the emission factor for soot reliably due to very high uncertainty in the results. McDaniel (1983) used a single sampling point above a pilot-scale flare to collect soot emissions on filters and to measure absolute soot concentration in the exhaust gas; However, he could not measure the dilution ratio

of the sample and, therefore, the emission factor was not calculated. Johnson et al. (2010, 2011) used the sky-LOSA technique for in-situ direct measurement of the mass rate of soot emitted from a visibly sooting flare. They reported soot mass emission rate of 2.0 ± 0.66 g/s for a large visibly sooting flare (Johnson et al., 2011). Johnson et al. (2013) also measured the soot mass emission rate for a gas flare at a turbocompressor station to be approximately 0.067 g/s. Another recent study conducted by McEwen and Johnson (2012) used laboratory-scale flares with different burner sizes and exit velocities to determine soot emission factors using gravimetric analysis and laser-induced incandescence (LII) system. They used 4- and 6-component fuel mixtures which represented associated-gas in the UOG industry and they reported soot emission factors between 50 to 550 mg soot/kg fuel for different burner diameters from 12.7 to 76.2 mm. McEwen and Johnson (2012) also obtained an empirical relationship between soot emission factor and fuel heating values for the conditions tested.

U.S. Environmental Protection Agency report AP-42 (Vol. I, 5th Ed.) used the results of McDaniel (1983) to report soot concentration values as 0 µg/L for non-smoking flares, 40 µg/L for lightly smoking flares, 177 µg/L for average smoking flares, and 274 µg/L for heavily smoking flares. These soot concentrations are reported per litre of exhaust products. McEwen and Johnson (2012) estimated soot emission factors (*i.e.,* mass per volume of fuel) based on these values (assuming no dilution and simple stoichiometry) to be 0, 0.9, 4.2, and 6.4 kg soot/10^3 m^3 fuel, respectively. In Canada, the Canadian Association of Petroleum Producers guide reported an emission factor of 2.56 kg soot/10^3 m^3

fuel for associated-gas flares (Canadian Association of Petroleum Producers, 2007). CAPP (2007) noted that this emission factor was calculated based on the PM (particulate matter) emission factor of 53 lb PM/10^6 ft^3 gas for flaring landfill gas (EPA, 1991) and was adjusted for a flare with _heating value of 45 MJ/m^3.

A few researchers have investigated the effect of non-hydrocarbon liquid droplets (*cf.*, Cotton et al., 1971; Bulewicz et al., 1975; Bonczyk, 1983, 1987, 1988; Mitchell and Miller, 1989) or vapors (*cf.*, Schug et al., 1980; Rao and Bardon, 1984) on soot formation mechanisms in flames or on PM emitted from diffusion flames. From these studies, very few researchers have focused on determining the properties of emitted PM from these flames. In Chapter 2, a small-scale co-flow methane diffusion flame was used to determine the size distribution and mass-mobility relationship of the PM when droplets of distilled water, sodium chloride solution, and hydrochloric acid solution were added to the fuel stream. The results showed a significant reduction in soot particle concentration when droplets of distilled water or HCl solution were added to the fuel stream. It was also concluded that PM concentration was increased when droplets of NaCl solution was added to the fuel stream; however, in this case, soot emissions were reduced while new NaCl particles were formed.

The current study is designed to bridge the previous studies of McEwen and Johnson (2012) and Chapter 2 in a pilot-scale experiment. The main objective of this study was to determine the morphology, size distributions, and emission factors of the particulate matter (PM) from turbulent diffusion flames with fuel composition and flow conditions similar to flares in the UOG industry when non-

hydrocarbon droplets composed of the major constituents found in the produced water and fracturing fluids were added to the fuel stream.

3.2 Experimental Setup

Experiments were carried out in a pilot-scale flare facility, which is shown schematically in. The facility consisted of a burner, fuel supply system, liquid delivery and droplet generation system, emission collection system, and the particle measurement suite, which included a scanning mobility particle sizer (SMPS) with thermodenuder, and a laser-induced incandescence (LII) system.

3.2.1 Burner

The burner used in the current study was designed based on the co-flow burner described in Chapter 2. The burner, comprised of a circular base with two ports at the bottom for fuel supply and another two ports at the bottom for draining accumulated liquid, was oriented vertically. An ultrasonic atomizer (Sono-Tek Corp., Model 06-04062) was fitted at the base of the burner to introduce 38 μm median diameter droplets into the fuel flow. The fuel was directed from the bottom of the burner to emerge around the atomizer tip, to support the entrainment of liquid droplets in the fuel flow. The top part of the burner consisted of a converging nozzle and the fuel exit tube with a diameter of 50.8 mm, where the turbulent diffusion flame was anchored. The fuel and liquid droplets mixed in the middle compartment of the burner before the nozzle and fuel exit tube and prior to combustion.

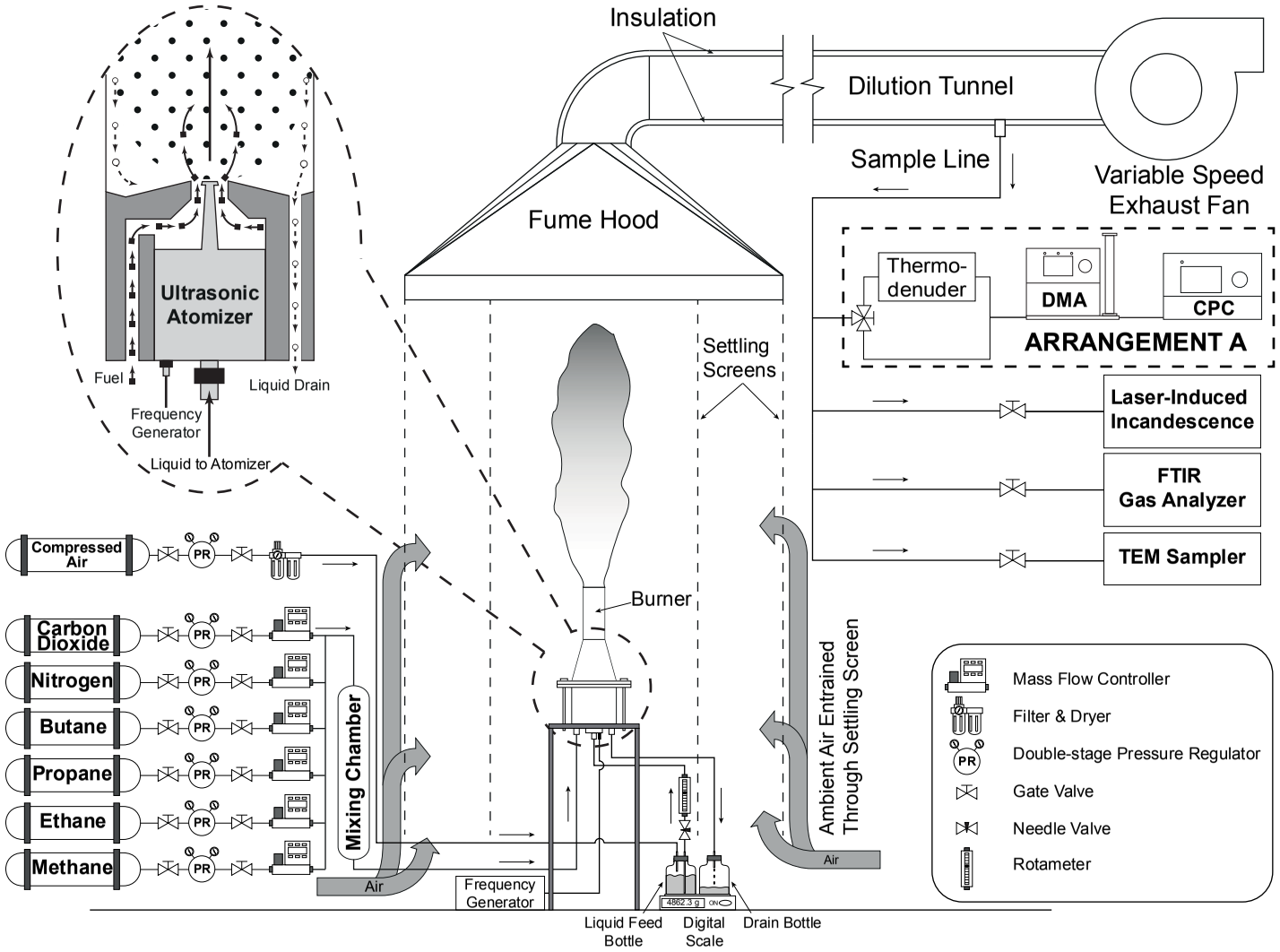

Figure 3.1: Schematic of the experiment setup with details of the diffusion flame burner

The behaviour of turbulent diffusion flame is described by Delichatsios (1993) who quantified flow conditions based on source Reynolds number (Re_s) and fuel gas Froude number (Fr_g). These two non-dimensional parameters are defined as

$$\mathrm{Re_s} = \frac{\rho_\infty u_e d_e}{\mu_\infty} \tag{3.1}$$

$$\mathrm{Fr_g} = \frac{u_e f_s^{3/2}}{(g d_e)^{1/2} \left(\frac{\rho_e}{\rho_\infty}\right)^{1/4}} \tag{3.2}$$

where u_e is the fuel gas exit velocity, d_e is the burner exit diameter, and ρ_∞ is the density of ambient air, μ_∞ is the dynamic viscosity of ambient air, f_s is the stoichiometric fuel fraction[1], g is the gravitational acceleration, and ρ_e is the fuel density.

In the current study, similar to the work of McEwen and Johnson (2012), the values of source Reynolds number and gas Froude number were chosen to be typical of flares in Alberta, Canada. These values span across "turbulent-buoyant transition-buoyant" and "turbulent-buoyant transition-shear" regimes in the regime map of turbulent diffusion flames proposed by Delichatsios (1993). Five different fuel gas flow rates with one burner exit diameter (50.8 mm) were tested.

[1] Stoichiometric fuel fraction (f_s) is the ratio of fuel mass flow rate to the fuel and air mixture mass flow rate. If we denote the stoichiometric air-to-fuel mass ratio by AF_s, the stoichiometric fuel fraction is

$$f_s = \frac{\dot{m}_{\mathrm{fuel}}}{\dot{m}_{\mathrm{fuel}} + \dot{m}_{\mathrm{air}}} \equiv \frac{1}{AF_s + 1}.$$

Table 3.1: Fuel flow rate, exit velocity, source Reynolds number, and gas Froude number of the 50.8-mm burner for the tested conditions

Fuel flow rate (SLPM[a])	Fuel exit velocity (m/s)	Source Reynolds number, Re_s	Gas Froude number, Fr_g
30.40	0.267	1080.1	0.00522
60.81	0.537	2160.5	0.01049
109.45	0.971	3888.6	0.01898
182.42	1.631	6480.8	0.03186
267.55	2.409	9505.2	0.04706

Note: [a] standard litres per minute (SLPM, evaluated at 0 °C and 1 atm)

Table 3.1 summarizes the fuel flow conditions with its corresponding gas Froude number and Reynolds number.

3.2.2 Fuel Mixture Supply

Fuel mixtures consisting of methane, ethane, propane, *n*-butane, carbon dioxide, and nitrogen was supplied by separate gas cylinders. The flow rate of each component was controlled and metered using mass flow controllers (Brooks, model 58XXS or SLA58XXS series). The fuel components were mixed in a mixing chamber before the fuel mixture was supplied to the base of the burner via its two fuel supply ports. Fuel flow rates were adjusted between ~30 SLPM and ~270 SLPM.

In this study, the fuel components and their concentrations in the mixture were chosen based on the data used by McEwen and Johnson (2012), which is representative of upstream oil and gas sites in Alberta, Canada. The fuel composition used in the current study is shown in Table 3.2 and matches the average 6-component fuel mixture used by McEwen and Johnson.

3.2.3 Liquid Composition and Delivery and Droplet Generation System

Three liquid types were used in this study: distilled water, sodium chloride solution, and hydrochloric acid solution. Droplets of NaCl solution were composed of an aqueous solution of 7.8% sodium chloride by mass. The sodium chloride mass concentration was selected based on the average concentration of sodium and chloride found in the fracturing fluid used in two UOG sites in Western and Eastern U.S. (McElreath, 2011). Droplets of HCl solution were composed of an aqueous solution of 1% hydrogen chloride by mass. The HCl mass concentration was chosen based on the typical maximum concentration of hydrochloric acid found in the fracturing fluid using an online chemical disclosure registry for UOG sites in the U.S. (Frac Focus, 2014).

In this study, similar to CHAPTER 2 2, an ultrasonic atomizer was used for generation of liquid droplets. Use of an ultrasonic atomizer had the advantage of generating liquid droplets where their mass flow rate was independent from the fuel gas flow rate. The ultrasonic atomizer equipped with a broadband ultrasonic generator (Model 06-05108), operating at 48 kHz, delivered a size distribution of droplets with a median diameter of 38 μm and geometric standard deviation of

Table 3.2: Fuel composition for the average 6-component mixture

Species	Gas Purity (%)	Average 6-Component Mixture (% SLPM)
Methane	99.0	85.24
Ethane	99.0	7.06
Propane	99.0	3.11
n-Butane	99.0	1.44
Carbon Dioxide	99.99	1.91
Nitrogen	99.999	1.24

1.84.

Liquid was delivered to the atomizer nozzle from a 4 L liquid feed bottle using 6 mm flexible tubing. Compressed air at approximately 14 kPa (gauge) displaced the liquid out of the bottle and the liquid flow rate delivered to the atomizer was set to 74 mL/min by a rotameter.

A portion of the liquid droplets did not exit the nozzle with the fuel due to collision with internal walls of the burner. This portion of droplets flowed back down to the drain bottle via the two drain ports located at the bottom of the burner base. To measure the net liquid flow rate added to the fuel stream, a technique similar to the one described in Chapter 2 was used. Using a digital scale, the combined mass of liquid in the feed and drain bottles was measured as a function of time. This mass and time were plotted and the slope of a fitted line was a measure of the net liquid flow rate added to the fuel stream (keeping in mind that a portion of this mass is in vapour phase due to the humidification of the fuel stream).

Penetration efficiency is the percentage of the net liquid mass flow rate added to the fuel stream to the mass flow rate of liquid droplets generated by the atomizer. A preliminary set of tests was conducted with different liquid input flow rates and gas flow rates to obtain insight into the penetration efficiency. The results showed that increasing the liquid input flow rate at gas flow rates of interest in this study, did not change the penetration efficiency considerably; *i.e.*, as more liquid was delivered to atomizer, the more liquid was drained from the burner base.

Therefore, in the current study, one liquid input flow rate was used (74 mL/min), which was the minimum flow rate that the rotameter could control stably.

It was further observed during the tests that the net liquid flow rate added to the fuel stream was not necessarily the same at a specified liquid input flow rate and fuel gas flow rate. Table 3.3 shows the net liquid flow rate and penetration efficiency of the three studied liquids (distilled water, NaCl solution, and HCl solution) obtained at different fuel gas flow rates at steady state. It is evident that the penetration efficiency is quite low, ranging from 2.7% to 6%. The same low penetration efficiency was reported in previous studies with similar liquid delivery and generation setups in Chapter 2 [efficiency of 4% and 6% for the two tested flow rates] and by Mitchell and Miller (1989) [efficiency of 3 – 4% for the tested conditions]. It can be shown[2] that in the burner's mixing chamber below the burner exit tube (*i.e.,* at 20 °C and 101.325 kPa), ~13% and ~84% of mass of distilled water droplets could be evaporated during mixing of droplets with dry fuel at 30.40 and 267.55 SLPM, respectively, if fuel saturated with water vapour is formed. (It is assumed that dry fuel has the properties of dry air for simplicity.) Theoretically, at atmospheric pressure, all water droplets could evaporate at ~55 °C and ~23 °C with dry fuel at 30.40 and 267.55 SLPM, respectively, if vapour-saturated fuel is formed. Liquid droplets were exposed to higher

[2] Humidity ratio, ω, is defined as, $\omega = \frac{\dot{m}_v}{\dot{m}_a} = \frac{0.622\,P_v}{P - P_v}$ where P_v is the vapour partial pressure and, for a saturated mixture, is equal to P_{sat} at certain temperature. At 20 °C, P_{sat}=2333 Pa and P=101325 Pa; therefore, $\omega = 0.01466$. Assuming $\dot{m}_a = \dot{m}_{fuel}$, the water vapour content of the saturated mixture can be obtained. For example, when fuel flow rate was 267.55 SLPM (i.e., $\dot{m}_{fuel} = 229.14$ g/min), $\dot{m}_v = 3.36$ g/min or ~84% of net liquid flow rate added to fuel stream.

Table 3.3: Net liquid flow rate added to fuel stream and penetration efficiency to the flame for different fuel gas flow rates and different liquids tested.

	Distilled water		NaCl solution		HCl solution	
Fuel gas flow rate (SLPM)	Net liquid flow rate (g/min)	Penetration efficiency (%)	Net liquid flow rate (g/min)	Penetration efficiency (%)	Net liquid flow rate (g/min)	Penetration efficiency (%)
30.40	2.96	4.0	2.03	2.7	2.67	3.6
60.81	2.20	3.0	3.56	4.8	3.50	4.7
109.45	2.65	3.6	2.86	3.9	4.39	5.9
182.42	3.10	4.2	3.53	4.8	4.36	5.9
267.55	4.02	5.4	4.46	6.0	3.88	5.2

temperatures due to flame radiation as they flew upward in the burner's fuel tube. Therefore, it would be likely that higher number (maybe all) of droplets evaporated before reaching the flame.

3.2.4 Emission Collection and Measurement

The emission collection system consisted of a large hexagon fume hood (circumscribed circle diameter 3.4 m), an insulated 406-mm round duct (dilution tunnel, DT), and a variable speed exhaust fan with extraction volume flow rate of approximately 100 m^3 per minute. The burner was fixed under the fume hood that captured the entire plume of combustion products and additional entrained ambient air.

Two open-ended cylindrical-shaped settling screens made from fine-sized wire-mesh with diameters of ~1.53 m and ~3.36 m were attached to the fume hood with a 0.3 m gap between their bottom and the floor. The two cylindrical settling screens surrounded the burner and the flame, and prevented the buffeting of flame from fluctuations in room air currents. The necessary air for combustion was

provided from ambient air entrained through the settling screens and the gap under them.

The variable speed exhaust fan at the end of the dilution tunnel drew the exhaust plume and emissions into the dilution tunnel and vented them outside the building. Emission samples were taken from the DT via the heated sample line and directed to instrument arrangement A, the LII, and the TEM sampling unit in Figure 3.1 (right).

It was crucial to ensure the complete mixing of combustion products and entrained dilution air occurred before sampling point. The Reynolds number in the dilution tunnel was higher than 4000, ensuring a turbulent flow regime. The sampling probe was traversed across the dilution tunnel to show that the extracted sample was independent of the radial position of the probe; hence, the combustion products and dilution air were fully mixed at the sampling point. Moreover, the sampling point on the dilution tunnel was chosen at a distance sufficiently far from the fume hood and any disturbances in the entrance to the dilution tunnel.

Another important factor in having an effective emission collection system was to ensure that the fume hood actually captured the entire combustion products plume. Six brackets each holding four thermocouples radiating outward were attached to the outside of the hood sides. The temperatures measured by thermocouples were monitored during each test. A sharp increase in the temperatures at the hood sides implied a leakage from the hot plume of exhaust gas to the space outside of the hood. Therefore, for each test, the speed of the

exhaust fan was adjusted to the minimum flow rate required to capture the entire plume. The minimum was chosen to keep concentration of exhaust products above the lower detection limit of the Fourier transform infrared spectroscopy (FTIR) gas analyzer. The measured dilution ratio in this study ranged from 20.5 for the highest fuel flow rate case to 104 for the lowest fuel flow rate. The fan speed was set in the range of 45 – 95% of its full speed to run the tests with different fuel gas flow rates used in this study.

Arrangement A in Figure 3.1 was used to measure the size distribution of the particulate matter by using a scanning mobility particle sizer (SMPS). The SMPS comprised of a differential mobility analyzer (DMA; TSI Inc., Model 3081) and a condensation particle counter (CPC; TSI Inc., Model 3025A). The aerosol and sheath air flow rates were 0.30 SLPM and 3.00 SLPM, respectively.

A thermodenuder (TD) similar to the one described by Ghazi and Olfert (2013) was used upstream of the SMPS with the purpose of removing any semi-volatile material on the particulate matter. The thermoduneder comprised of a 2.4-m stainless steel tubing with two sections: the 12.5-mm ID heating section was 1.6 m long and was maintained at 160°C using resistive heaters and a temperature controller, and the 3-mm ID cooling section was 0.8 m long and was maintained at room temperature. The emission sample was first heated up in the heating section and then cooled down in the cooling section. This process caused the condensation of PM volatile coating on the inner wall of the tubing in the cooling section. A small piece of conductive tubing was used to bypass the TD in this study. Therefore, some of the particles were lost in the TD due to diffusion or

thermophoresis and particle concentrations out of the TD must be corrected for these losses (see Appendix B for details). As discussed in Appendix B, undenuded and denuded particles had nearly identical total concentrations and count median diameters; hence, very little volatile material was observed on the particles from the flame without and with liquid droplets. Therefore, all of the results presented in this study were reported for undenuded particles.

A laser-induced incandescence system (LII; Artium Technologies Inc., Model LII200) was used to measure the soot volume fraction (f_v) in the emission sample in real time. In LII, a pulsed laser heats the soot particles in the sample to their sublimation temperature (4000–4500 K). As the soot particles cool, their incandescence is measured and related to soot volume fraction (Snelling et al., 2005). LII is not sensitive to NaCl particles because these particles do not absorb the radiation from the laser pulse, hence they do not sublime. (Refractive index of NaCl at laser excitation wavelength of 1064 nm is 1.5312 with no imaginary part and, therefore, NaCl is a non-absorbing particle.) The LII sample flow rate was ~13.6 SLPM and its sampling rate was 20 Hz in this study.

A transmission electron microscopy (TEM) particle sampling unit (ESP Nano, Model 100) was used to collect particulate matter emissions on TEM grids (NetMesh 01885-F). Particle sampling unit had a flow rate of 100 cm^3/min and pre-pumped the connecting tubing for 20 s before colleting samples on the grids for 2-4 s. Samples were stored in airtight bags with desiccant before analysis with TEM. The imaging was done using a transmission electron microscope (Hitachi, Model H7600) operating at 80 kV. Images were taken at high resolution with a

magnification range of 50,000 – 400,000 and from different positions on each TEM grid.

3.2.5 Emission Factor Calculations

Particulate matter emissions are typically described by emission factors in environmental regulations, which is the mass of PM emission per unit mass or unit volume of fuel. Occasionally, particulate emission factors are based on particle number (*e.g.,* the automotive industry; European Union regulation No. 715/2007).

In this study, the SMPS measured particle number concentration per unit volume of gas and the LII measured soot volume fraction. The calculations to obtain emission factors from measured values from SMPS and LII is shown in detail in Appendix C.

The molar flow rate of exhaust products ($\dot{n}_{\text{exh.prod.}}$) was calculated by balancing the stoichiometric combustion reaction assuming complete combustion (see Appendix C for details):

$$\dot{n}_{\text{exh.prod.}} = \left[\left(3.76\left(x+\frac{y}{4}\right)+x+\frac{y}{2}\right)X_{\text{C}_x\text{H}_y}+X_{\text{CO}_2}+X_{\text{N}_2}\right]\frac{\dot{m}_{\text{fuel}}}{M_{\text{fuel}}} \tag{3.3}$$

where $\dot{m}_{\text{fuel}}$ is the fuel mass flow rate, M_{fuel} is the fuel molar mass, $X_{\text{C}_x\text{H}_y,\text{fuel}}$, $X_{\text{CO}_2,\text{fuel}}$, and $X_{\text{N}_2,\text{fuel}}$ are the mole fractions of the hydrocarbon, CO_2, and N_2 in the fuel, respectively. Parameters x and y are the number of carbon and hydrogen atoms in the hydrocarbon in the fuel, respectively.

The results of the measured mass emission factor in this study suggested that soot accounted for less than 0.1% of the combusted carbon by mass (see section 3.3.4.1). Therefore, the molar flow rate of the diluted exhaust in the duct, assuming negligible soot mass is

$$\dot{n}_{\text{duct}} = \frac{\dot{n}_{\text{fuel}}}{\left(X_{\text{CO}_2,\text{duct}} - X_{\text{CO}_2,\infty}\right)} \times \left[x X_{\text{C}_x\text{H}_y,\text{fuel}} + X_{\text{CO}_2,\text{fuel}} - X_{\text{CO}_2,\infty} \frac{M_{\text{fuel}}}{M_\infty} - X_{\text{CO}_2,\infty} \times 4.76 \left(x + \frac{y}{4} \right) X_{\text{C}_x\text{H}_y,\text{fuel}} \right] \tag{3.4}$$

where the subscript "∞" indicates entrained air (composed of combustion and dilution air). Mole fraction of CO_2 in the duct and entrained air ($X_{\text{CO}_2,\text{duct}}$ and $X_{\text{CO}_2,\infty}$, respectively) were measured by a FTIR gas analyzer (MKS Instruments, Model Multigas 2030).

The soot mass emission factor measured by LII, Y_{LII}, can be obtained from,

$$Y_{\text{LII}} = \frac{\dot{m}_{\text{soot}}}{\dot{m}_{\text{fuel}}} = \frac{\rho_{\text{soot}}\, f_{v,\text{LII}}\, \dot{n}_{\text{duct}}\, R\, T_{\text{LII}}}{\dot{m}_{\text{fuel}}\, P_{\text{stat}}} \tag{3.5}$$

where ρ_{soot} is the density of soot, $f_{v,\text{LII}}$ is the soot volume fraction of the sample measured by LII, R is the ideal gas constant (8.314 J/mol·K), T_{LII} is the temperature of the measurement cell of LII (K), and P_{stat} is the static pressure in the duct. The density of soot is the material density of primary soot particles and was considered equal to 1800 kg/m^3 (Park et al., 2004).

Similarly, mass emission factor measured by SMPS can be calculated as

$$Y_{\mathrm{SMPS}} = \frac{(\text{mass of particles per volume of air } @T_{\mathrm{CPC}})\, \dot{n}_{\mathrm{duct}}\, R\, T_{\mathrm{CPC}}}{\dot{m}_{\mathrm{fuel}}\, P_{\mathrm{stat}}} \qquad (3.6)$$

where T_{CPC} is the temperature of the CPC manufacturer's standard conditions (21.1 °C), and mass of particles per volume of air is calculated by integrating the mass concentration distribution obtained from SMPS measurements (see section 3.3.4.3 for details).

Number emission factor, *i.e.,* total particle number per fuel mass, was calculated by a similar relationship to Equation (3.6) as

$$\frac{N_{\mathrm{PM}}}{m_{\mathrm{fuel}}} = \frac{(\text{number of particles per volume of air } @T_{\mathrm{CPC}})\, \dot{n}_{\mathrm{duct}}\, R\, T_{\mathrm{CPC}}}{\dot{m}_{\mathrm{fuel}}\, P_{\mathrm{stat}}} \qquad (3.7)$$

where number of particles per volume of air (*i.e.,* total particle concentration) is the integral of particle size distribution.

It should be noted that Equations (3.5), (3.6), and (3.7) assumed that the source of all the particulate matter was from the flare. This assumption was validated by measuring negligible particles in the system using CPC and LII when the flame was not present.

A detailed uncertainty analysis of the emission factors measured by LII and SMPS is presented in Appendix D. The calculated uncertainties are shown as error bars in the graphs illustrated in section 3.3.

3.3 Results and Discussion

3.3.1 TEM analysis

Transmission electron microscope (TEM) imaging was performed on the particulate matter samples collected from flames without and with liquid droplets at different fuel flow rates. The purpose of this imaging process was to investigate dependencies on the morphology of particles.

Figure 3.2 shows a sample of images from the four different cases: the flame without any liquid droplets (*i.e.,* the "dry flame"), the flame with distilled water droplets, the flame with NaCl solution droplets, and the flame with droplets of HCl solution. More images of particles from flames with different liquid mass ratios are showed in Appendix E.

Figure 3.2(a) shows particles from the flame with no add liquid droplets to it. The morphology of the particles was very typical of soot generated by combustion with an open, fractal-like structure. In addition to soot agglomerates, single particles were also observed in the images with mean diameter of 23 nm (and standard deviation of 8 nm) which is typical of primary soot particles.

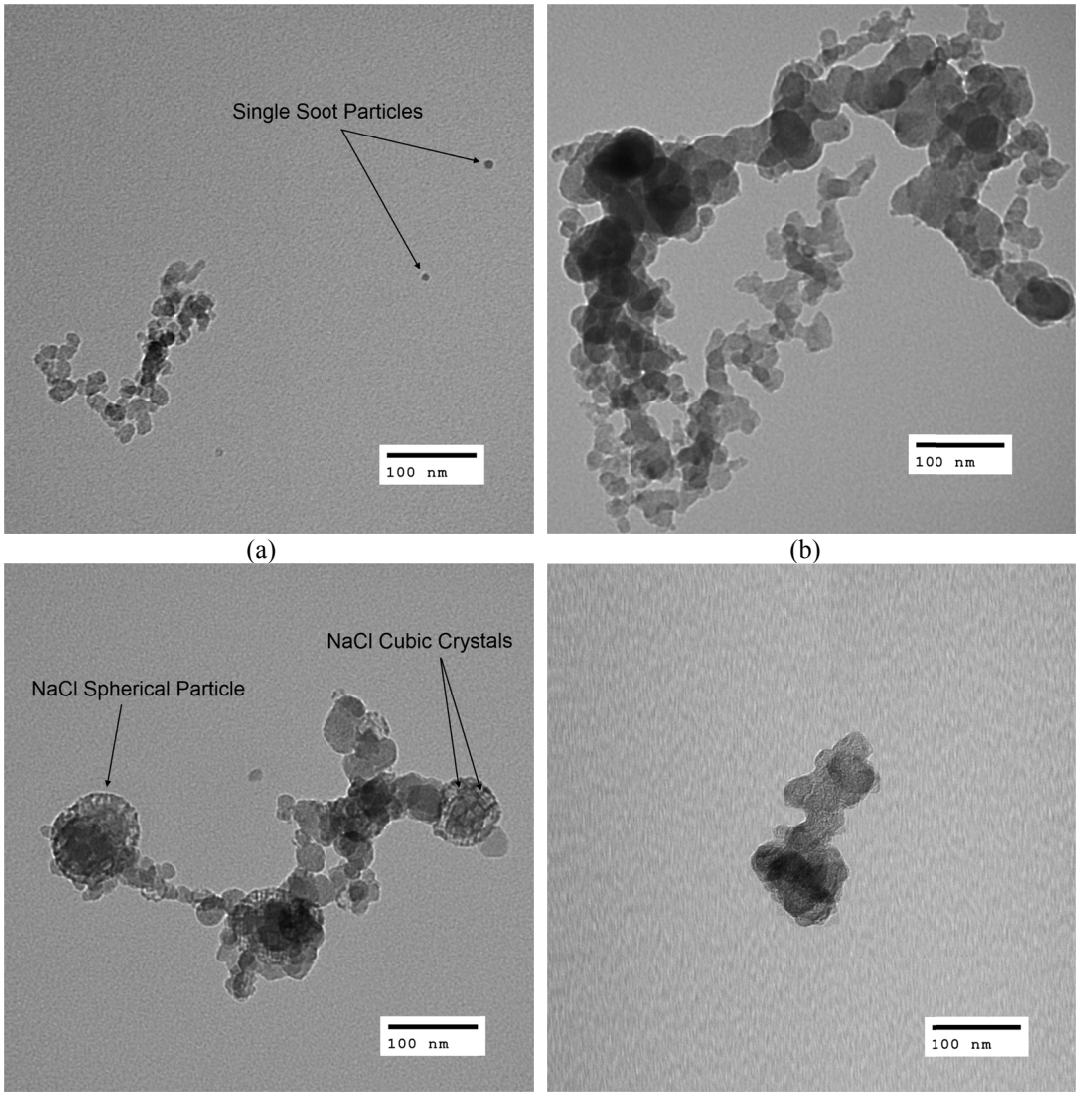

Figure 3.2: TEM imaging of samples from the flame with (a) no liquid, (b) distilled water, (c) NaCl solution, and (d) HCl solution.

Figure 3.2(b) shows particles from the flame with distilled water droplets. The morphology of particles was typical of combustion-generated soot agglomerates with the fractal-like structure. However, primary soot particles composing the agglomerates had very distinct sizes ranging from small (~8 nm) to quite large (~55 nm) diameters.

Figure 3.2(c) shows particles from the flame with droplets of NaCl solution. As illustrated, these particles were mainly composed of fractal-like soot aggregates and spherical particles containing NaCl crystals. The majority of these spherical structures, with embedded salt crystals, were attached to the soot aggregates; however, they were also been observed as single particles. Typical soot agglomerates with no attached NaCl particles were also observed (R. Dastanpour, personal communication, April 2014). These images show that NaCl particles can either be internally or externally mixed with soot aggregates in the flame with NaCl droplets. It was suggested in Chapter 2 that particle emission from such a flame were external and internal mixture of NaCl and soot particles based on particle mass-mobility measurements.

Figure 3.2(d) shows particles from the flame with droplets of HCl solution. The morphology of particles was similar to a fractal-like structure in most cases; however, the primary particles were not readily identifiable in these structures. Some single particles were also seen in addition to agglomerates. These single particles (with the size of typical primary soot particle, or ~20 nm) were like crumpled spheres. It seemed that these primary particles aggregated to form the large agglomerates with no distinguishable primary particle.

3.3.2 Effect of liquid droplet on particle size distribution from flare

Figure 3.3 shows the size distributions measured by SMPS for undenuded particles from the turbulent flame without and with droplets of distilled water, NaCl solution, and HCl solution.

To study the effect of liquid droplets on particle size distribution, the liquid mass ratio was defined as the ratio of liquid mass flow rate to fuel mass flow rate ($\dot{m}_{liquid}/\dot{m}_{fuel}$). Figure 3.3 shows the particle size distributions for flares with the highest and lowest liquid mass ratios (lowest and highest tested fuel flow rates, respectively). Particle size distributions for flares with other intermediate liquid mass ratios are shown in Appendix F. It is evident from Figure 3.3 that droplets of distilled water and HCl solution caused a modest reduction in particle concentration compared to the flare without any liquid droplets and the reduction in particle concentration is higher at larger liquid mass ratios (compare Figure 3.3(a) to Figure 3.3(b)). This result is in agreement with the results of Chapter 2 for a small-scale diffusion flame. In this case, droplets of distilled water and HCl solution were injected in a sooty diffusion flame; however, the liquid mass ratios in their study were quite high at approximately 0.25 and 0.33 kg liquid per kg of fuel (see Chapter 2). Other studies also suggest the effect of water on supressing soot from diffusion flames is mainly due to thermal effects (Schug et al., 1980). Droplets of distilled water and HCl solution also led to the generation of slightly smaller particles from the flare compared to the dry flame.

It can be seen in Figure 3.3(a) that droplets of HCl solution reduced the PM concentration from the flare to a level only slightly higher than the distilled water droplets. This result is expected as the HCl solution was very weak and 99% of its mass was distilled water.

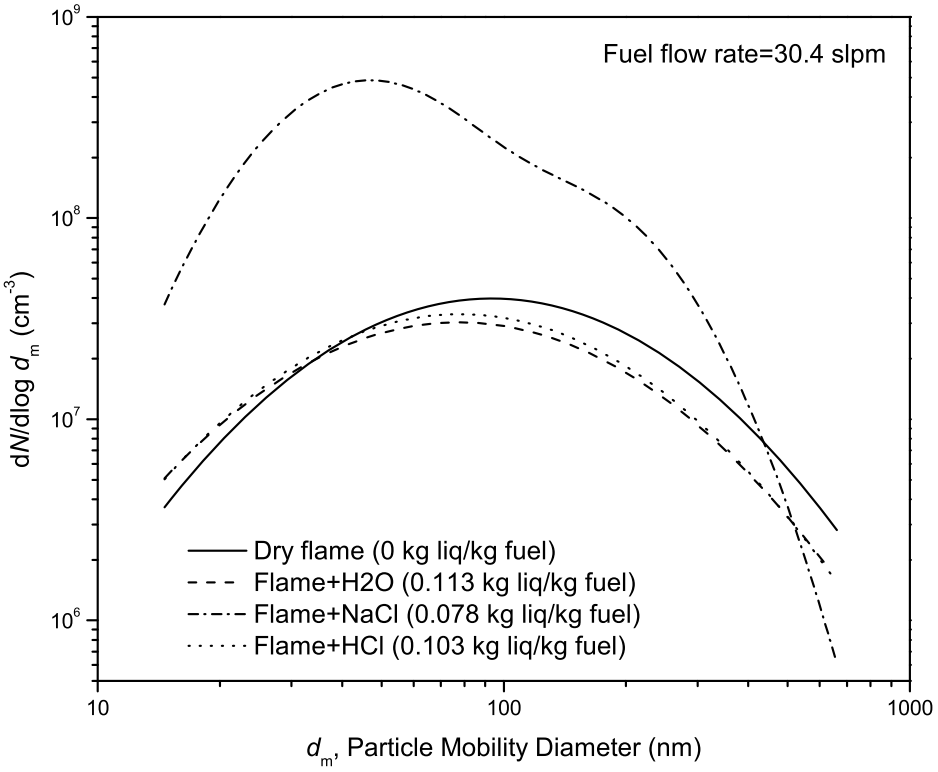

(a)

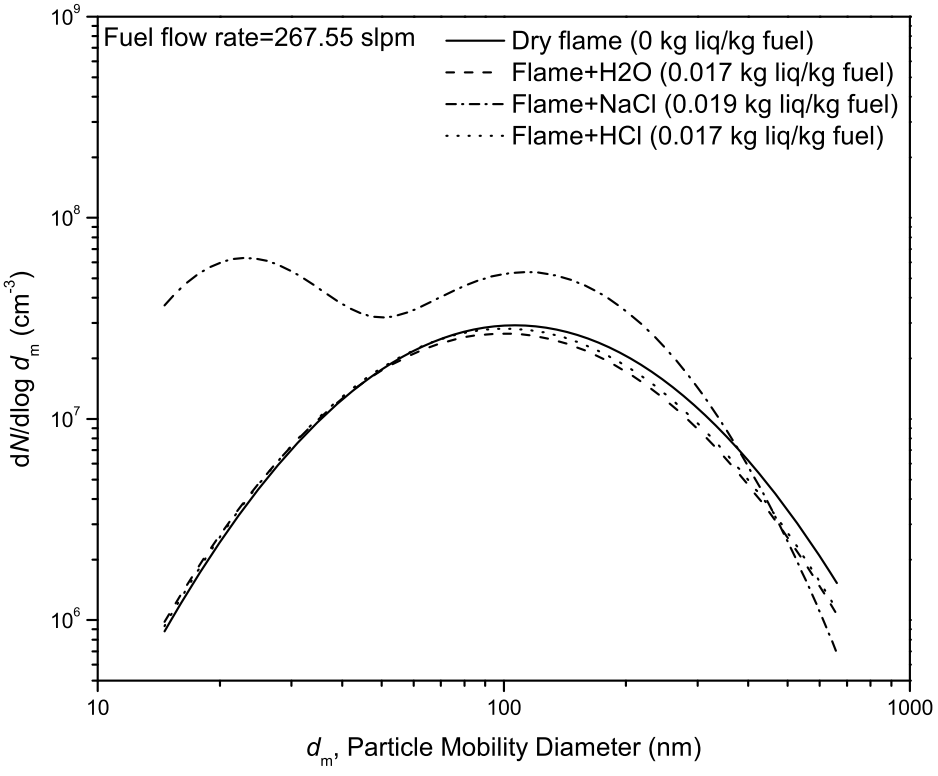

(b)

Figure 3.3: Particle size distribution for the flare without and with different liquid droplets with (a) highest liquid mass ratio, and (b) lowest liquid mass ratio

Figure 3.3(a) also shows that the droplets of NaCl solution increased particle concentration by an order of magnitude compared to the dry flame. The particle size distribution was bimodal in this case with a larger mode for smaller particle sizes. As the TEM analysis showed (see section 3.3.1), it is speculated that in the flame with droplets of NaCl solution, sodium chloride evaporates at high flame temperatures and then nucleates to generate at higher number of NaCl particles that are either internally or externally mixed with soot.

Figure 3.4 better illustrates the effect of NaCl solution mass ratios on particle size distribution. When the liquid mass ratio was highest, the size distribution was composed of one large dominant first mode and a small second mode. As the liquid mass ratio was decreased, the first mode became smaller and the second mode grew relatively larger. Considering the counter effect between the two modes, it is speculated that the first mode represented single NaCl particles and the second mode was mostly internally-mixed soot and NaCl particles as well as soot agglomerates not attached to NaCl crystals (see section 3.3.1). In a limiting case where NaCl solution mass ratio is close to zero, the vast majority of particles generated by the flare are soot. In the other extreme case where NaCl solution mass ratio is quite high, the majority of particles from the flare are NaCl particles. The latter case was studied in Chapter 2 where, for the NaCl solution mass ratio of 0.33 kg liquid per kg fuel, particles from the flame were mainly NaCl with only a small fraction of soot. It is also evident from Figure 3.4 that as the NaCl solution mass ratio decreased, the particle concentration also decreased.

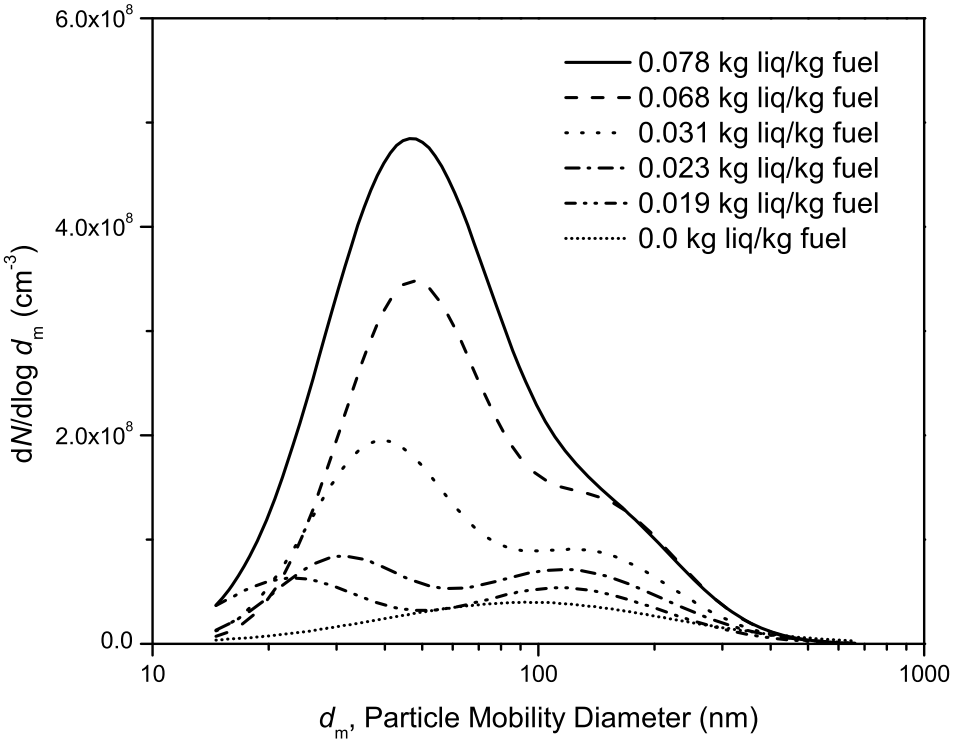

Figure 3.4: Particle size distribution for the flare with droplets of NaCl solution with different liquid mass ratios

Figures G.1–G.3 in Appendix G show the effect of liquid mass ratio on particle size distribution for distilled water and HCl solution, separately. (For the case of dry flame, the effect of fuel flow rate is shown.)

3.3.3 Comparison of mass concentration measured by the SMPS and LII

As discussed earlier, particle emissions were quantified in the form of mass emission factors defined by Equation (3.5) and (3.6) in this study. To obtain SMPS-measured mass emission factor from Equation (3.6), particle mass per volume air (*i.e.,* particle mass concentration) needs to be obtained. To calculate particle mass concentration, the particle size distribution fitted with a lognormal function was multiplied by the mobility-dependent mass function of particles from Equation (3.9) and integrated as follows:

$$M_{\text{tot}} = \int_0^{\infty} \left(\frac{dN}{d \log d_{\text{m}}} \right) m(d_{\text{m}})\, d \log d_{\text{m}} \tag{3.8}$$

where M_{tot} is the total particle mass concentration and $m(d_{\text{m}})$ is the mass-mobility function of particles determined from Equation (3.9) in each case.

As discussed in Chapter 2, a set of experiments with DMA-CPMA-CPC were conducted to determine mass-mobility relationship of particles from a methane turbulent diffusion flame without and with droplets of NaCl solution and HCl solution. These relationships were used in this study as follows:

$$\begin{aligned} &\text{For PM from dry flame: } m = 7.10 \times 10^{-6}\, d_{\text{m}}^{2.27} \\ &\text{For PM from flame+NaCl droplets: } m = 1.50 \times 10^{-6}\, d_{\text{m}}^{2.89} \\ &\text{For PM from flame+HCl droplets: } m = 6.01 \times 10^{-6}\, d_{\text{m}}^{2.30} \end{aligned} \tag{3.9}$$

where m is the particle mass (fg) and d_{m} is the particle mobility diameter (nm).

For the flame with distilled water droplets, it was assumed that the vast majority of particles were typical soot agglomerates as electron micrographs showed (see section 3.3.1) and the mass-mobility relationship for PM from dry flame was used in obtaining M_{tot}. For the flame with droplets of NaCl solution, particle size distribution was bimodal (refer to section 3.3.2). In this case, the particle size distribution was decomposed to two log-normal distributions with the first distribution (or mode) assumed to be NaCl particles mostly and the second distribution (or mode) assumed to be soot particles. This assumption introduced some uncertainty in the calculated M_{tot} because transmission electron micrographs

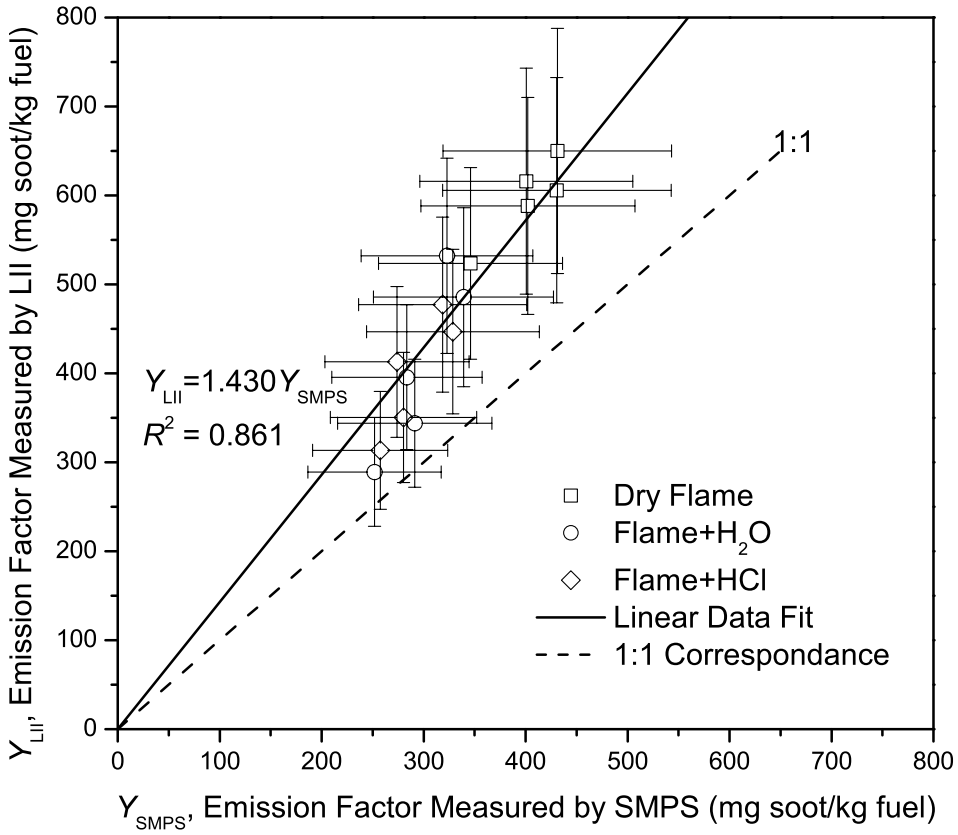

Figure 3.5: Comparison of soot mass emission factor measured by SMPS and LII for the dry flame and the flame with droplets of distilled water and HCl solution.

suggested that a portion of particulate matter was an internal mixture of NaCl and soot particles (see section 3.3.1). For the flame with droplets of HCl solution, the liquid mass ratio in the current study was not sufficient to cause semivolatile coating on the particles. Therefore, the mass-mobility relationship for the denuded particles from the flame with HCl solution was used from Chapter 2.

Figure 3.5 shows a comparison between soot mass emission factor measurements by SMPS and LII for the flame without and with droplets of distilled water and HCl solution. The particles from the flame with droplets of NaCl solution were not included in this comparison as the LII is only sensitive to soot particles. It is clear from the figure that the LII measured higher mass emission rates compared

to the SMPS. The linear data fit in Figure 3.5 shows that the LII measured ~43% higher mass emission factor on average. Therefore, there is an unidentified systematic error between mass emission factors measured by LII and SMPS.

3.3.4 Emission factors

In an effort to scale particulate matter emissions from a flame with its fuel flow conditions, the fire Froude number (Fr_f) was suggested as the important parameter by Delichatsios (1993) and used by McEwen and Johnson (2012). Some other researchers suggested other parameters, including the Richardson ratio (Becker and Liang, 1982) and soot generation efficiency normalized for smoke point (Canteenwalla, 2007). In this study, the fire Froude number was used as it presented a better correlation in scaling PM emissions.

The fire Froude number is similar to the fuel gas Froude number defined by Equation (3.2); however, it has a term for temperature ratio which accounts for flow acceleration resulting from buoyant forces. The fire Froude number is defined as

$$\mathrm{Fr_f} = \frac{u_e f_s^{3/2}}{\left(\frac{\Delta T_f}{T_\infty} g d_e\right)^{1/2} \left(\frac{\rho_e}{\rho_\infty}\right)^{1/4}} \tag{3.10}$$

where $\Delta T_f = T_{adb} - T_\infty$ is the adiabatic flame temperature (T_{adb}) minus the ambient temperature (T_∞).

3.3.4.1 Comparing soot mass emission factor results from dry flame with previous studies

Figure 3.6 shows the comparison of soot mass emission factor from the dry flames measured by LII and SMPS in the current study with those reported by McEwen and Johnson (2012). Both studies used an average 6-component fuel mixture based on methane with a composition described in Table 3.2; however, McEwen and Johnson used three different burner sizes.

Figure 3.6 shows that the current study extended the range of fire Froude numbers studied. The trend of change in soot emission factor with increasing fire Froude number was quite different between the two studies. In the current study, the LII-

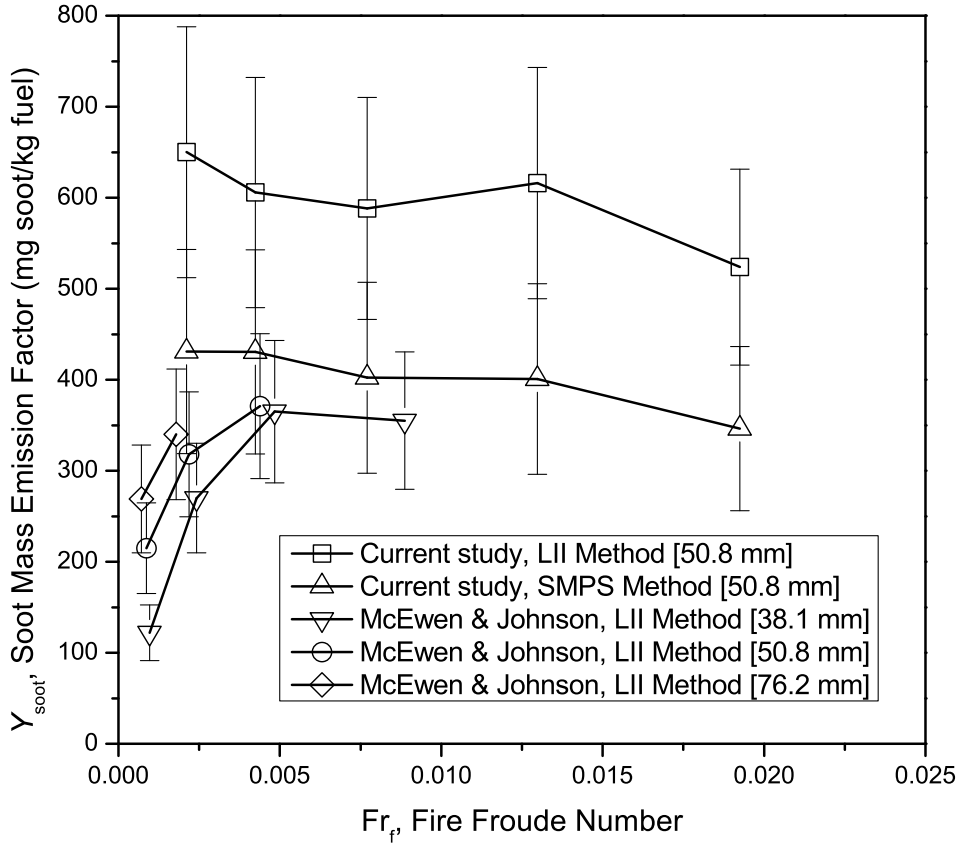

Figure 3.6: Soot mass emission factor as a function of fire Froude number for dry flames – comparison of current study with previous studies

and SMPS-measured soot emission factors appeared to decrease as the fire Froude number increased. The average soot emission factor measured by SMPS and LII over the studied range of fire Froude number (from 0.002 to 0.02) was ~400 ± 40 and ~600 ± 60 mg soot/kg fuel, respectively. In contrast, with increasing fire Froude number, the LII-measured soot emission factors by McEwen and Johnson (2012) increased for all three burner sizes to an apparent constant value. They suggested that the soot emission factor had an increasing trend to a horizontally asymptotic value of ~400 mg soot/kg fuel for the three burner sizes.

Figure 3.6 also shows the unidentified systematic difference between LII and SMPS measurements as explained in section 3.3.3. The extent of uncertainties involved in both measurements makes it difficult to explain this systematic difference; however, future work is required to deploy other methods to improve these uncertainties.

3.3.4.2 Effect of liquid mass ratio on mass emission factor

To investigate the effect of liquid droplets on the flame's particulate matter emissions, the particle mass emission factors measured by SMPS and LII were plotted as a function of liquid mass ratio in Figure 3.7. The figure shows the average particle mass emission factor for the dry flame (*i.e.,* 0 kg liquid/kg fuel) measured by SMPS and LII as 402 and 597 mg soot/kg fuel, respectively.

When droplets of distilled water or HCl solution were added to the flame, the SMPS-measured mass emission factor decreased compared to that of the dry flame. The mass emission factor continued to decrease modestly as the liquid

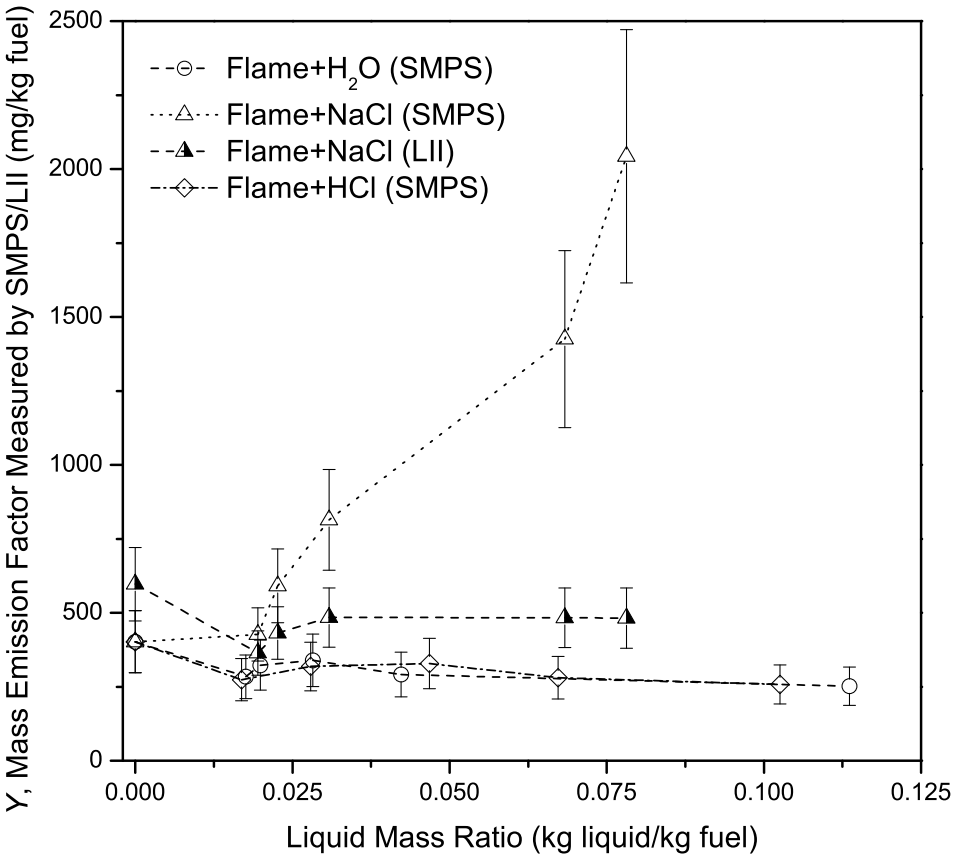

Figure 3.7: Particulate matter emission factor as a function of liquid mass ratio for the flame with liquid droplets

mass ratio increased. This result shows that water acted as a suppressant for soot production. Similar effect from distilled water on impairing soot emissions from a methane diffusion flame was reported by Schug et al. (1980), Rao and Bardon (1984), and in Chapter 2. Moreover, the similarity in the emission factor trend of distilled water and HCl solution cases was mostly because the HCl solution used in the current study was 99% distilled water by mass. However, droplets of HCl solution did not decrease emission factor to the same level of distilled water.

When droplets of NaCl solution were injected in the flame, as the liquid mass ratio increased, the particle mass emission factor measured by SMPS sharply elevated to about 5 times of the average mass emission factor of the dry flame. On

the other hand, the mass emission factor measured by LII was notably lower than the mass emission factor measured by SMPS, particularly at high liquid mass ratios. The higher mass emission factor measured by SMPS was due to the presence of a species of particles other than soot to which the LII was insensitive. As the TEM imaging showed (see section 3.3.1), these particles are newly-formed NaCl particles in the flame. LII can only detect the soot part of total particulate matter emission. The difference between the mass emission factor measured by SMPS and LII gives an estimate of NaCl emission factor. Table 3.4 summarizes the mass ratio of NaCl emitted as particles ($m_{NaCl,out}$) to NaCl injected into the flame ($m_{NaCl,in}$). Input mass of NaCl into the flame per unit mass of fuel was obtained from the liquid mass ratio and mass concentration of NaCl solution. To calculate $m_{NaCl,out}/m_{NaCl,in}$, the NaCl emission factor was divided by the input mass of NaCl into the flame per unit mass of fuel. Approximately 26% and 4% of the mass of NaCl injected into the flame was turned into NaCl particles for the highest and lowest NaCl solution mass ratios, respectively. Table 3.4 shows that as more NaCl solution was injected into the flame, more of the dissolved NaCl turned into particles measured by SMPS. It seems that as more NaCl is vaporised in the flame, the likelihood of nucleation and formation of NaCl particle increases

Table 3.4: Ratio of NaCl turned into particle to NaCl injected into the flame

Liquid Mass Ratio (kg NaCl sol/kg fuel)	Input Mass of NaCl into Flame per Unit Mass of Fuel (g NaCl/kg fuel)	$\frac{m_{NaCl,out}}{m_{NaCl,in}}$
0.078	6.09	0.26
0.068	5.33	0.18
0.031	2.40	0.14
0.023	1.76	0.09
0.019	1.51	0.04

and, therefore, more of NaCl is turned into particle.

Another significant result from Figure 3.7 is that the soot emission factor from the flame with NaCl solution droplets was lower than that of the dry flame. This result is in agreement with other studies in the literature that suggested aqueous solution of alkali salts (including NaCl) have a suppressing effect on soot produced by diffusion flames (Bulewicz et al., 1975; Haynes et al., 1979; Bonczyk, 1983; Bonczyk, 1988; Mitchell and Miller, 1989). Therefore, the effect of droplets of NaCl solution on the flame was suppressing the soot and the formation of significantly more particulate matter of which the majority was NaCl particles.

3.3.4.3 Number emission factor measured by SMPS

Figure 3.8 shows the particle number emission factor, defined by Equation (3.7), as a function of the fire Froude number. It is apparent from Figure 3.8 that number emission factor generally had a decreasing trend for the flame without and with liquid droplets as the fire Froude number increased. Moreover, flames with droplets of different liquids showed another common trend: the particle number emission factor appeared to be decreasing to that of the dry flame when the fire Froude number increased. This trend can be attributed to the fact that at larger fire Froude numbers, the liquid mass ratio was lower and, therefore, the liquid droplets had less effect on the particle emissions.

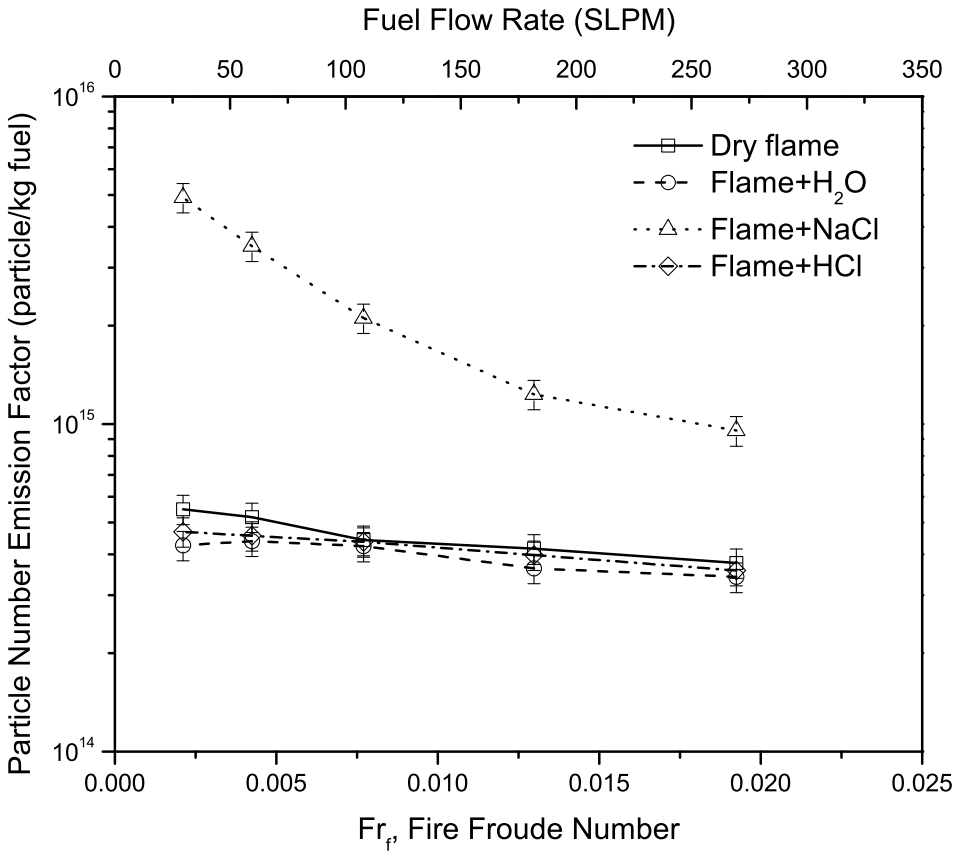

Figure 3.8: Particle number emission factor for the flame with no liquid droplets and with droplets of distilled water, NaCl solution, and HCl solution.

It is also clear from Figure 3.8 that the droplets of distilled water and HCl solution had an effect on impairing particulate matter emissions from the flame; however, droplets of HCl solution did not reduce PM emissions to the same level as the distilled water droplets and the difference between the two PM emissions was within the uncertainty of the measurements. This result is shown in Figure 3.8 with the data points for the flame with HCl droplets was sandwiched between the data points for the dry flame and the flame with distilled water droplets. At lower fire Froude numbers, the difference between number emission factor of the dry flame and the flame with droplets of distilled water or HCl solution was more noticeable due to higher liquid mass ratio.

3.4 Conclusions

The current study was an investigation into the potential effects of major non-hydrocarbon liquids found during and after hydraulic fracturing process on particulate emissions of flares. The flaring process was simulated by a pilot-scale diffusion flame having similar flow conditions typical of Alberta flares with a 6-component methane-based fuel mixture representative of flared gases in the UOG industry. Measurements by SMPS and LII indicated that droplets of distilled water and dilute HCl solution decreased soot emissions and mass and number emission factors compared to those of a similar flame with no liquid droplets. The extent of soot reduction was dependent on liquid mass ratio with a large liquid mass ratio having the strongest effect on soot suppression.

SMPS-measured mass emission factors for the dry flame were slightly decreasing with respect to the fire Froude number. The average soot emission factor for the dry flame for a range of fire Froude number from 0.002 to 0.02 was ~400 ± 40 and ~600 ± 60 mg soot/kg fuel measured by SMPS and LII, respectively. There was an unidentified systematic error between SMPS- and LII-measured mass emission factors considering the uncertainties.

The effects of NaCl solution on particulate emissions of the flame are complex, but the results showed that in this case, the mass and number emission factors and the particle emissions were increased by order of magnitude compared to the dry flame. TEM images, bimodal particle size distribution, and LII soot measurements provided more insight into the mixing state of particles. The emitted particles composed of fractal soot aggregates internally or externally

mixed with NaCl spherical particles with embedded crystals. These results showed that NaCl aqueous solution reduced soot formation compared to the dry flame; however, new NaCl particles were formed which increased the total particle emissions significantly. The mass and number emission factors sharply elevated as the liquid mass ratio increased.

CHAPTER 4

Conclusions and Recommendations

4.1 Summary and Conclusions

This study consisted of two sets of experiments at different physical scales to investigate the effects of non-hydrocarbon liquid droplets typically found in the produced water after hydraulic fracturing operations on particulate emissions from gas flares. Three liquids were considered in this study: distilled water, aqueous sodium chloride solution, and hydrochloric acid solution. In the first experiment, a small-scale (pipe diameter of 9.45 mm) methane diffusion flame operating either above or below the smoke point was used to explore the potential effects of aforementioned liquids on particle emissions from the flame. In the second experiment, pilot-scale turbulent diffusion flames (pipe diameter of 50.8 mm) with flow conditions and fuel compositions similar to flares in the UOG industry were used. The purpose of the second experiment was to mimic typical flares in Alberta to obtain relevant emission factors to compare to those currently

in emissions inventories. It should be noted that the results from both experiments should be interpreted within the studied ranges of the following: The median diameters of liquid droplets were 19 μm and 38 μm for small- and pilot-scale experiments, respectively, and the droplets were log-normally distributed with GSD of 1.84. The concentration of NaCl and HCl solutions were 7.8%-10% and 1%, respectively, which represents typical concentrations of these compounds in the produced water. Furthermore, both experiments studied a range of liquid mass ratios from ~0.017 to ~0.343 kg liquid/kg fuel.

Particle size distributions from the small-scale experiment suggested that distilled water and dilute HCl solution reduce total particle emission by orders of magnitude compared to the flame with no droplet injection. However, NaCl solution caused a significant increase in particle emission by approximately an order of magnitude. Lower concentrations of NaCl solution resulted in proportionally reduced particle mass concentrations.

Previous studies suggested that soot formation in NaCl-doped flames is reduced; therefore, it was suggested in the current study that from the high concentration of particle emissions from such a flame, the majority was due to the generation of high numbers of relatively small NaCl particles. This result was supported by elemental analysis using XPS and mass-mobility measurements using DMA-CPMA. The elemental analysis showed that sodium and chlorine in the form of solid NaCl was produced in the samples collected from NaCl-doped flame. DMA-CPMA results showed that the majority of particles emitted from such a flame had similar effective density to pure dried NaCl particles (~2200 to ~1600 kg/m^3)

with a smaller contribution from larger particles with lower density (~1400 kg/m^3). The large particles with lower effective density could be internal mixture of soot and NaCl or merely coagulated particles.

The mass-mobility relationship for the particulate emissions from the flame with no liquid droplet showed that the particles were fractal soot aggregates similar to particles from other combustion sources. DMA-CPMA results for the HCl-doped flame showed that the emitted particles from the flame were fractal-like soot aggregates internally mixed with a small amount of condensed semi-volatile material on smaller particles.

SMPS and LII measurements in the pilot-scale experiment revealed that distilled water and HCl solution decreased particle emissions and mass and number emission factors compared to those of similar unseeded diffusion flames. This result was similar to the results from the small-scale flame. Moreover, liquid mass ratio influenced the extent of emission reduction with high liquid mass ratios having the strongest effect.

There was an unidentified systematic error between SMPS- and LII-measured mass emission factors. The average soot emission factors from unseeded flames over a wide range of fire Froude number (from 0.002 to 0.02) were ~400 ± 40 and ~600 ± 60 mg soot/kg fuel measured by SMPS and LII, respectively.

The pilot-scale experiment provided an insight into the mixing state of particles from NaCl-doped diffusion flames. One of the important differences between this experiment and the small-scale flame was that the liquid mass ratio was ~3 to ~20

times lower in the pilot-scale experiment. The unimodal log-normal size distribution observed in the small-scale experiment, turned into a bimodal size distribution for the pilot-scale experiment which implied the existence of two types of particles in the emissions. Furthermore in the pilot-scale, TEM images showed that emitted particles from NaCl-doped flames were fractal-like soot aggregates internally and externally mixed with NaCl spherical particles with embedded NaCl crystals. SMPS measurements showed that, for the NaCl-doped flames, particle emissions, and mass and number emission factors increased significantly compared to similar unseeded flames. LII results showed that soot emission was reduced in this case; however, new NaCl particles were formed which increased particle emissions considerably. This result was similar to the results of small-scale flame. With increasing liquid mass ratio, the particle emissions and emission factors elevated sharply. Considering the results of both experiments, when the liquid mass ratio was small, more soot particles existed in the emissions along with NaCl particles; however, in the small-scale flame where the liquid mass ratio was several times higher, the vast majority of emitted particles were single NaCl particles and only a small fraction of them were internally mixed with soot.

4.2 Recommendations for future work

Future work on the topic of this study can be summarized as below:

1. With known effects of distilled water, NaCl solution, and HCl solution on the particle emissions from diffusion flames, future work can study the combined effect of these liquids as a more realistic substitution for produced water after

fracturing operation. In the ideal situation, real samples of produced water from oil battery sites can be used for future studies. Detailed chemical analysis of such samples could be the topic of a separate study.

2. There is currently a knowledge gap about the real mass ratio of possible liquid droplets in the flared gas flow. This study examined a wide range of liquid mass ratios from ~0.017 to ~0.343 kg liquid/kg fuel. Realistic liquid mass ratios could be outside the studied range. Most knock-out drums used for liquid-gas separation are designed for more than 99% efficiency. However, after long-term service and possible poor maintenance, the separation efficiency could drop and the chance of more liquid get into the flared gas flow increases. In-situ measurements of the actual liquid content of gas directed to the flare stack can fill this knowledge gap and help with studying the effect of liquid mass ratios that are more realistic and relevant to industry and regulators.

3. The gas Froude number and Reynolds numbers used for gas flow conditions in the current study only covered a small area of the Reynolds-Froude number regime map for turbulent diffusion flames. The estimated area that represents typical upstream oil and gas flares with solution gas on this regime map is much larger with relatively large burner sizes (from 76.2 mm to 254 mm). Future studies should consider using various burner sizes, including large burners, to cover different subregimes which represent realistic flares. Using large burners requires larger facilities compared to the pilot-scale experiment used in this study. One issue would be huge consumption of fuel for such a

facility to reach desired Reynolds and gas Froude numbers. The current flare facility used in this study uses gas bottles to precisely meter each component of fuel before mixing. Larger facilities would probably need to run on commercial natural gas supply with constant composition over time. The exact fuel composition representing average flares can be obtained by conditioning the fuel with metered flow of certain components from bottles.

4. In the pilot-scale experiment, mass emission factors were estimated by using the mass-mobility relationships obtained from small-scale flame. As discussed before, this method introduces an error in the calculated emission factors, especially for NaCl doped flames. In the small-scale experiment, the emitted particles were mostly single NaCl particles; however, in the pilot-scale flame, the second mode of the bimodal size distribution is presumably internal mixture of soot and NaCl. Future work should include simultaneous DMA-CPMA measurements to determine the actual mass-mobility relationship of particles from all studied flames.

5. To quantify the mixing of various species of particles in the emissions from the flames, a robust analytical technique must be used in any future study. Any possible semi-volatile and volatile compound in the emissions was lost in the XPS analysis used in this study. Possible better methods include gas chromatography mass spectroscopy. High resolution XPS scans can also be used for bonding states between different elements in solid phase. Energy-dispersive X-ray spectroscopy (EDS or EDX) is another analytical technique

used for elemental analysis and provides a more reliable average of particles in the sample compared to XPS.

6. With the current emission collection system used in the pilot-scale experiment, there is a chance of losing solid particles that do not necessarily follow the plume of exhaust gas into the hood. Improvements in the emission collection system leads to capturing the majority of (heavier) particles and the efficiency of such a system can be evaluated by tracking the input and output mass of compounds that are not combustion products (*e.g.* sodium chloride).

Bibliography

Alberta Energy Regulator. (2013). *Upstream Petroleum Industry Flaring and Venting Report: Industry Performance for Year Ending December 31, 2012* (No. ST60B-2013). Calgary, AB, Canada: Alberta Energy Regulator.

American Petroleum Institute. (2010). *Freeing Up Energy. Hydraulic Fracturing: Unlocking America's Natural Gas Resources.* American Petroleum Institute.

Arthur, J. D., Bohm, B., Coughlin, B. J., Layne, M., Cornue, D. (2008a). *Evaluating the Environmental Implications of Hydraulic Fracturing in Shale Gas Reservoirs.* ALL Consulting LLC.

Arthur, J. D., Bohm, B., & Layne, M. (2008b). Hydraulic fracturing considerations for natural gas wells of the marcellus shale. Paper presented at the *Ground Water Protection Council Annual Forum.* Cincinnati.

Becker, H. A., and Liang, D. (1982). Total Emission of Soot and Thermal Radiation by Free Turbulent Diffusion Flames. *Combustion and Flame,* 44(1-3):305-318.

Bonczyk, P. A. (1983). In-Situ Optical Measurement of Additive Effects on Particulates in a Sooting Diffusion Flame. *Combustion and Flame,* 51:219-229.

Bonczyk, P. A. (1987). The Influence of Alkaline-Earth Additives on Soot and Hydroxyl Radicals in Diffusion Flames. *Combustion and Flame,* 67(2):179-184.

Bonczyk, P. A. (1988). Suppression of Soot in Flames by Alkaline-Earth and Other Metal Additives. *Combustion Science and Technology,* 59(1-3):143-163.

Bulewicz, E. M., Evans, D. G., Padley, P. J. (1975). Effect of Metallic Additives on Soot Formation Processes in Flames. *Symposium (International) on Combustion,* 15(1):1461-1470.

Canadian Association of Petroleum Producers. (2007). *A Recommended Approach to Completing the National Pollutant Release Inventory (NPRI) for the Upstream Oil and Gas Industry*. Calgary, AB, Canada: Canadian Association of Petroleum Producers.

Canteenwalla, P. M. (2007). *Soot emissions from turbulent diffusion flames burning simple alkane fuels.* Master's degree dissertation, Carleton University, Ottawa, ON.

Charlez, P. A. (1997). *Rock mechanics: Petroleum applications*. Vol. 2. Paris: Editions Technip.

Choi, M. Y., Hamins, A., Mulholland, G. W., Kashiwagi, T. (1994). Simultaneous Optical Measurement of Soot Volume Fraction and Temperature in Premixed Flames. *Combustion and Flame,* 99(1):174-186.

Choi, M. Y., Mulholland, G. W., Hamins, A., Kashiwagi, T. (1995). Comparisons of the Soot Volume Fraction using Gravimetric and Light Extinction Techniques. *Combustion and Flame,* 102(1-2):161-169.

Clearstone Engineering Ltd. (2002). *Estimation of flaring and venting volumes from upstream oil and gas facilities* Canadian Association of Petroleum Producers.

Cotton, D. H., Friswell, N. J., Jenkins, D. R. (1971). The Suppression of Soot Emission from Flames by Metal Additives. *Combustion and Flame,* 17(1):87-98.

Cross, E. S., Onasch, T. B., Ahern, A., Wrobel, W., Slowik, J. G., Olfert, J. et al. (2010). Soot Particle Studies-Instrument Inter-Comparison-Project Overview. *Aerosol Science and Technology,* 44(8):592-611.

Delichatsios, M. A. (1993). Transition from Momentum to Buoyancy-Controlled Turbulent Jet Diffusion Flames and Flame Height Relationships. *Combustion and Flame,* 92(4):349-364.

Devillers, R. W., Thomson, K. A., & Johnson, M. R. (2012). Soot emission measurement in flares by sky-LOSA: Reduction of uncertainty in field

measurements. Paper presented at the *Proceedings of the Air and Waste Management Association's Annual Conference and Exhibition, AWMA, , 3*. pp. 2141-2146. Retrieved from SCOPUS database.

Dobbins, R. A., Mulholland, G. W., Bryner, N. P. (1994). Comparison of a Fractal Smoke Optics Model with Light Extinction Measurements. *Atmospheric Environment,* 28(5):889-897.

Dockery, D. W., Pope, C. A., Xu, X., Spengler, J. D., Ware, J. H., Fay, M. E. et al. (1993). An Association between Air Pollution and Mortality in Six US Cities. *New England Journal of Medicine,* 329(24):1753-1759.

Elvidge, C. D., Ziskin, D., Baugh, K. E., Tuttle, B. T., Ghosh, T., Pack, D. W. et al. (2009). A Fifteen Year Record of Global Natural Gas Flaring Derived from Satellite Data. *Energies,* 2(3):595-622.

European Commission. (2007). *REGULATION (EC) No 715/2007 of 20 June 2007 on Type Approval of Motor Vehicles with Respect to Emissions from Light Passenger and Commercial Vehicles (Euro 5 and Euro 6) and on Access to Vehicle Repair and Maintenance Information*. European Union: Official Journal of the European Union (OJ L 171, 29.6.2007, p. 1).

Frac Focus. *Chemical disclosure registry - find a well.* Retrieved March 28, 2014, from www.fracfocusdata.org/DisclosureSearch/

Ghazi, R., and Olfert, J. S. (2013). Coating Mass Dependence of Soot Aggregate Restructuring due to Coatings of Oleic Acid and Dioctyl Sebacate. *Aerosol Science and Technology,* 47(2):192-200.

Ghazi, R., Tjong, H., Soewono, A., Rogak, S. N., Olfert, J. S. (2013). Mass, Mobility, Volatility, and Morphology of Soot Particles Generated by a Mckenna and Inverted Burner. *Aerosol Science and Technology,* 47(4):395-405.

Gomaa, A. M., Mahmoud, M. A., Nasr-El-Din, H. A. (2011). Effect of Shear Rate on the Propagation of Polymer-Based in-Situ-Gelled Acids Inside Carbonate Cores. *SPE Production and Operations,* 26(1):41-54.

Hansen, J., Sato, M., Ruedy, R., Lacis, A., Oinas, V. (2000). Global Warming in the Twenty-First Century: An Alternative Scenario. *Proceedings of the National Academy of Sciences of the United States of America,* 97(18):9875-9880.

Haynes, B. S., Jander, H., Wagner, H. G. (1979). The Effect of Metal Additives on the Formation of Soot in Premixed Flames. *Symposium (International) on Combustion,* 17(1):1365-1374.

Hinds, W. C. (1999). *Aerosol technology: Properties, behavior, and measurement of airborne particles* (2nd ed.). John Wiley & Sons.

Holmen, A., Rokstad, O. A., Solbakken, A. (1976). High-Temperature Pyrolysis of Hydrocarbons .1. Methane to Acetylene. *Industrial & Engineering Chemistry Process Design and Development,* 15(3):439-444.

Housiadas, C., and Drossinos, Y. (2005). Thermophoretic Deposition in Tube Flow. *Aerosol Science and Technology,* 39(4):304-318.

Intergovernmental Panel on Climate Change. (2013). *Climate change 2013-the physical science basis: Working group I contribution to the fifth assessment report of the IPCC*. Vol. 4 Cambridge University Press.

Johnson, M. R., Devillers, R. W., Thomson, K. A. (2011). Quantitative Field Measurement of Soot Emission from a Large Gas Flare using Sky-LOSA. *Environmental Science and Technology,* 45(1):345-350.

Johnson, M. R., Devillers, R. W., Thomson, K. A. (2013). A Generalized Sky-LOSA Method to Quantify Soot/Black Carbon Emission Rates in Atmospheric Plumes of Gas Flares. *Aerosol Science and Technology,* 47(9):1017-1029.

Johnson, M. R., Devillers, R. W., Yang, C., Thomson, K. A. (2010). Sky-Scattered Solar Radiation Based Plume Transmissivity Measurement to Quantify Soot Emissions from Flares. *Environmental Science and Technology,* 44(21):8196-8202.

Johnson, M. R., and Kostiuk, L. W. (2000). Efficiencies of Low-Momentum Jet Diffusion Flames in Crosswinds. *Combustion and Flame,* 123(1-2):189-200.

Johnson, M. R., and Kostiuk, L. W. (2002). A Parametric Model for the Efficiency of a Flare in Crosswind. *Proceedings of the Combustion Institute,* 29(2):1943-1950.

Johnson, M. R., Kostiuk, L. W., Spangelo, J. L. (2001). A Characterization of Solution Gas Flaring in Alberta. *Journal of the Air and Waste Management Association,* 51(8):1167-1177.

Johnson, M. R., Kostiuk, L. W., Spangelo, J. L. (2001). A Characterization of Solution Gas Flaring in Alberta. *Journal of the Air and Waste Management Association,* 51(8):1167-1177.

Johnson, M. R., Wilson, D. J., Kostiuk, L. W. (2001). A Fuel Stripping Mechanism for Wake-Stabilized Jet Diffusion Flames in Crossflow. *Combustion Science and Technology,* 169(1):155-174.

Kostiuk, L. W., Johnson, M. R., Thomas, G. P. (2004). *University of Alberta Flare Research Project Final Report November 1996 – September 2004*. Edmonton, AB: University of Alberta.

Kostiuk, L. W., Majeski, A. J., Poudenx, P., Johnson, M. R., Wilson, D. J. (2000). Scaling of Wake-Stabilized Jet Diffusion Flames in a Transverse Air Stream. *Symposium (International) on Combustion,* 28(1):553-559.

Krewski, D., Burnett, R. T., Goldberg, M. S., Hoover, K., Siemiatycki, J., Jerrett, M. et al. (2000). Reanalysis of the Harvard Six Cities Study and the American Cancer Society Study of Particulate Air Pollution and Mortality. *Cambridge, MA: Health Effects Institute,* 295

Maricq, M. M., and Xu, N. (2004). The Effective Density and Fractal Dimension of Soot Particles from Premixed Flames and Motor Vehicle Exhaust. *Journal of Aerosol Science,* 35(10):1251-1274.

McDaniel, M. (1983). *Flare Efficiency Study* (No. EPA/600/2-83-052). Research Triangle Park, NC: US Environmental Protection Agency.

McElreath, D. (2011). Comparison of hydraulic fracture fluid composition with produced formation water quality following fracturing - implications for fate and transport. *Proceedings of the Technical Workshops for the Hydraulic Fracturing Study: Fate and Transport,* Washington, DC. pp. 22-27.

McEwen, J. D. N. (2010). *Soot emission factors from lab-scale flares burning solution gas mixtures.* Master's degree dissertation, Carleton University, Ottawa, ON.

McEwen, J. D. N., and Johnson, M. R. (2012). Black Carbon Particulate Matter Emission Factors for Buoyancy-Driven Associated Gas Flares. *Journal of the Air and Waste Management Association,* 62(3):307-321.

McMurry, P. H., Wang, X., Park, K., Ehara, K. (2002). The Relationship between Mass and Mobility for Atmospheric Particles: A New Technique for Measuring Particle Density. *Aerosol Science and Technology,* 36(2):227-238.

Mitchell, J. B. A., and Miller, D. J. M. (1989). Studies of the Effects of Metallic and Gaseous Additives in the Control of Soot Formation in Diffusion Flames. *Combustion and Flame,* 75(1):45-55.

Ndubizu, C. C., and Zinn, B. T. (1982). Effects of Metallic Additives upon Soot Formation in Polymer Diffusion Flames. *Combustion and Flame,* 46(C):301-314.

New York State Department of Environmental Conservation. (2011). *Revised Draft Supplemental Generic Environmental Impact Statement on the Oil, Gas and Solution Mining Regulatory Program*. Albany, NY: New York State Department of Environmental Conservation.

Olfert, J. S., Reavell, K. S., Rushton, M. G., Collings, N. (2006). The Experimental Transfer Function of the Couette Centrifugal Particle Mass Analyzer. *Journal of Aerosol Science,* 37(12):1840-1852.

Park, K., Cao, F., Kittelson, D., McMurry, P. (2003). Relationship between Particle Mass and Mobility for Diesel Exhaust Particles. *Environmental Science & Technology,* 37(3):577-583.

Park, K., Kittelson, D. B., Zachariah, M. R., McMurry, P. H. (2004). Measurement of Inherent Material Density of Nanoparticle Agglomerates. *Journal of Nanoparticle Research,* 6(2-3):267-272.

Pohl, J. H., Lee, J., Payne, R., Tichenor, B. A. (1986). Combustion Efficiency of Flares. *Combustion Science and Technology,* 50(4-6):217-231.

Powell, R. J., McCabe, M. A., Slabaugh, B. F., Terracina, J. M., Yaritz, J. G., Ferrer, D. (1999). Applications of a New, Efficient Hydraulic Fracturing Fluid System. *SPE Production and Facilities,* 14(2):139-143.

Ramanathan, V., and Carmichael, G. (2008). Global and Regional Climate Changes due to Black Carbon. *Nature Geoscience,* 1(4):221-227.

Rao, V. K., and Bardon, M. F. (1984). The Effect of Water on Gas Phase Soot Formation in Laminar Diffusion Flames. *Combustion and Flame,* 55(1):73-78.

Rissler, J., Messing, M. E., Malik, A. I., Nilsson, P. T., Nordin, E. Z., Bohgard, M. et al. (2013). Effective Density Characterization of Soot Agglomerates from various Sources and Comparison to Aggregation Theory. *Aerosol Science and Technology,* 47(7):792-805.

Schug, K. P., Manheimer-Timnat, Y., Yaccarino, P., Glassman, I. (1980). Sooting Behaviour of Gaseous Hydrocarbon Diffusion Flames and the Influence of Additives. *Combustion Science and Technology,* 22(5-6):235-250.

Siegel, K. D. (1980). *Degree of conversion of flare gas in refinery high flares.* PhD degree dissertation, University of Karlesruhe, Germany.

Snelling, D. R., Smallwood, G. J., Liu, F., Gülder, Ö L., Bachalo, W. D. (2005). A Calibration-Independent Laser-Induced Incandescence Technique for Soot Measurement by Detecting Absolute Light Intensity. *Applied Optics,* 44(31):6773-6785.

Strosher, M. T. (2000). Characterization of Emissions from Diffusion Flare Systems. *Journal of the Air and Waste Management Association,* 50(10):1723-1733.

U.S. Department of Energy. (2009). *Modern Shale Gas Development in the United States: A Primer.* Office of Fossil Energy and National Energy Technology Laboratory, United States Department of Energy.

U.S. Energy Information Administration. *International energy statistics: Natural gas production.* Retrieved October 28, 2013, from http://www.eia.gov/cfapps/ipdbproject/iedindex3.cfm?tid=3&pid=43&aid=1

U.S. Environmental Protection Agency. (1991). *Data from Flaring Landfill Gas* (Confidential Report No. ERC-55). U.S. Environmental Protection Agency.

U.S. Environmental Protection Agency. (1995). *AP-42 – Compilation of Air Pollutant Emission Factors* (Volume I, 5 ed.). Research Triangle Park, NC: U.S. Environmental Protection Agency.

U.S. Environmental Protection Agency. (2004). *Evaluation of Impacts to Underground Sources of Drinking Water by Hydraulic Fracturing of Coalbed Methane Reservoirs* (No. EPA/816/R-04/003). Washington, DC: U.S. Environmental Protection Agency.

U.S. Environmental Protection Agency. (2009). *Integrated Science Assessment for Particulate Matter (Final Report)* (No. EPA/600/R-08/139F). Washington, DC: U.S. EPA.

Waxman, H. A., Markey, E. J., DeGette, D. (2011). Chemicals used in Hydraulic Fracturing. *United States House of Representatives, Committee on Energy and Commerce,*

Wu, J. S., Krishnan, S. S., Faeth, G. M. (1997). Refractive Indices at Visible Wavelengths of Soot Emitted from Buoyant Turbulent Diffusion Flames. *Journal of Heat Transfer,* 119(2):230-237.

Appendix A

A.1 Calculation of Distribution for_ Dried Sodium Chloride Droplets

It is possible to obtain the frequency distribution for droplets of sodium chloride solution (mass fraction of 10%) based on the specifications of the ultrasonic atomizer (Sono-Tek Corp). The operating instructions for ultrasonic atomizer model 06-04022 stated that the atomized droplet size distribution typically followed a log-normal distribution. At the operating frequency of 120 kHz, the count median diameter (CMD) of this distribution was 19 μm with the geometric standard deviation (σ_g) of 1.84. Using this data, the frequency distribution function was obtained by substituting above values in the following equation:

$$\frac{df}{d\log d_m} = \frac{1}{\sqrt{2\pi}\log\sigma_g}\exp\left(-\frac{(\log d_m - \log \mathrm{CMD})^2}{2(\log\sigma_g)^2}\right) \qquad (A.1)$$

The resulting frequency distribution for droplets of sodium chloride solution generated by the ultrasonic atomizer is plotted in solid line in Figure A.1.

By knowing the density of sodium chloride solution (w_{NaCl} = 0.10) as 1070.7 kg/m^3, the mass of each droplet can be calculated for different droplet sizes. We know that the mass of sodium chloride in each droplet is 10% of the droplet mass. Therefore, assuming spherical particles, the expected diameter for dried sodium chloride particles can be easily obtained from its mass. Figure A.1 also shows the expected frequency distribution for dried sodium chloride particles with the dashed line. The vast majority of dried NaCl particles are expected to be

larger than 1 μm, with the count median diameter of approximately 7 μm. In Figure 2.2 and for the case of injected sodium chloride solution with no diffusion flame, the small particle concentration and its rising trend on the right-hand side, is presumably the left-hand tail of the distribution predicted in Figure A.1. Therefore, the high particle concentration measured when droplets of sodium chloride solution were burned can be attributed to the generation of new particles and not merely the dried droplets passing through the flame.

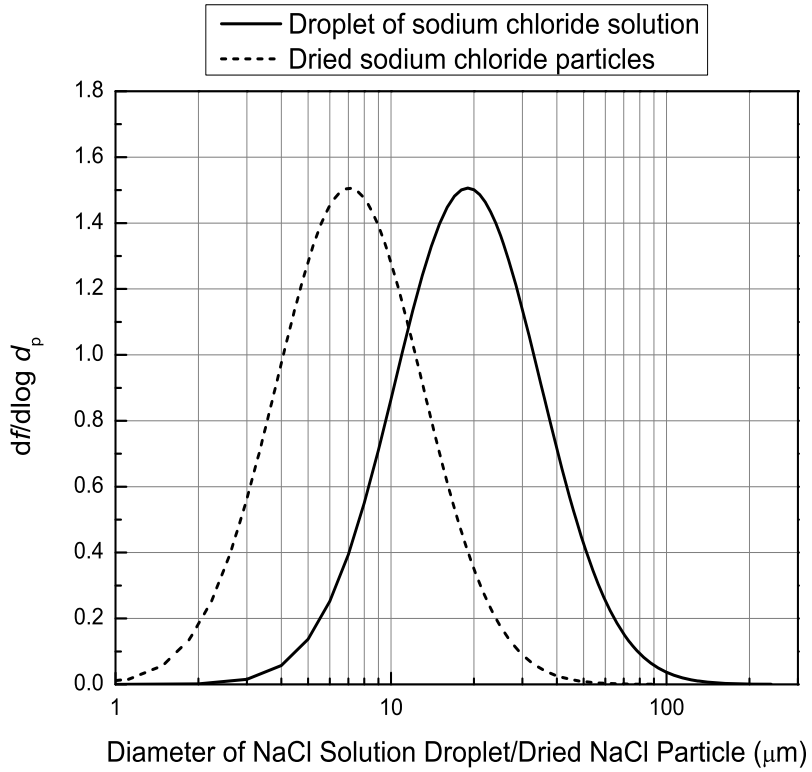

Figure A.1: Frequency distribution for droplets of sodium chloride solution and for dried sodium chloride particles

A.2 Effects of Liquid Flow Rate on the Particle Size Distribution of the Sooty Flame

As mentioned in the experiment setup, two different liquid flow rates were studied for the sooty flame. Liquid mass ratio is defined as the ratio of liquid mass to fuel mass, or m_{liquid}/m_{fuel}. The lower net liquid flow rate (0.132 mL/min) corresponds to the liquid mass ratio of 25%. The higher net liquid flow rate (0.180 mL/min) corresponds to the liquid mass ratio of 34%. (This range of liquid mass ratios was limited by the atomizer.) The results presented in section 3.2 were for the higher liquid mass ratio. Figures A.2–A.3 show size distributions for the sooty flame (base case), and the sooty flame with distilled water, NaCl solution, and HCl solution injected at two different liquid mass ratios. Figure A.5 shows total number concentrations for the same conditions. In the case of distilled water (Figure A.2), the concentration of soot particles increased when liquid mass ratio was reduced. Lower liquid mass ratio showed less effect on soot suppression and caused a bi-modal particle size distribution, however, the total concentration of soot particles still remained very low. In the case of droplets with NaCl (Figure A.3), the increase in liquid mass ratio caused a slight change in concentration of particles but with a slightly larger median diameter (i.e., larger particles are generated). This result was expected as more sodium chloride was available for nucleation when the liquid mass ratio was higher. In the case of hydrochloric acid (Figure A.4), the reduction in liquid mass ratio generated larger particles; however, the total particle concentrations corresponding to the low and high liquid mass ratio cannot be compared directly because the SMPS did not measure the same range of mobility diameter. Therefore, total number

concentrations are reported in Figure A.5 for the overlapping range of mobility diameter of both liquid mass ratios (i.e., 15-225 nm).

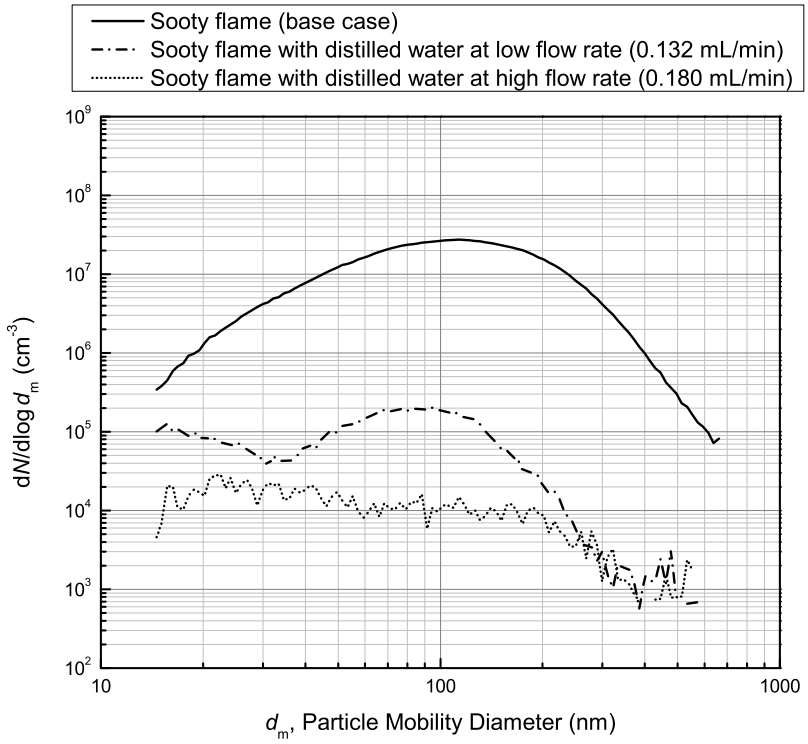

Figure A.2: Particle size distribution for the sooty flame (base case) and sooty flame with low and high distilled water loading

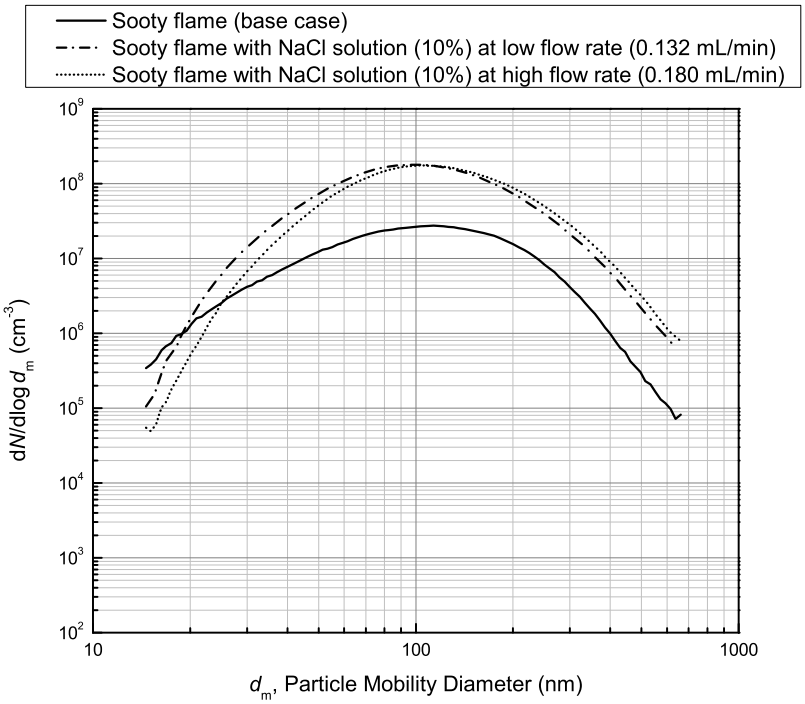

Figure A.3: Particle size distribution for the sooty flame (base case) and sooty flame with low and high loading of sodium chloride solution

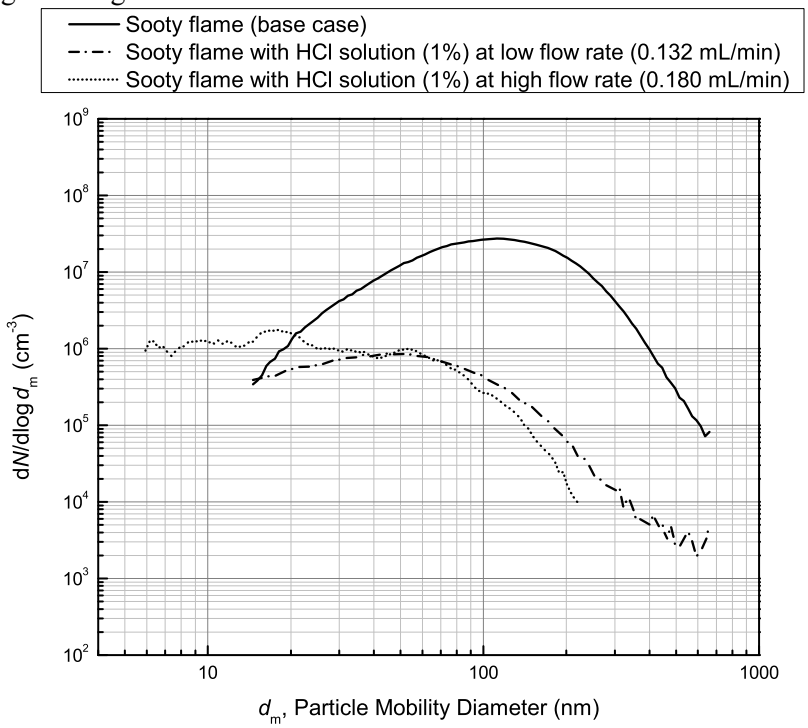

Figure A.4: Particle size distribution for the sooty flame (base case) and sooty flame with low and high loading of hydrochloric acid solution

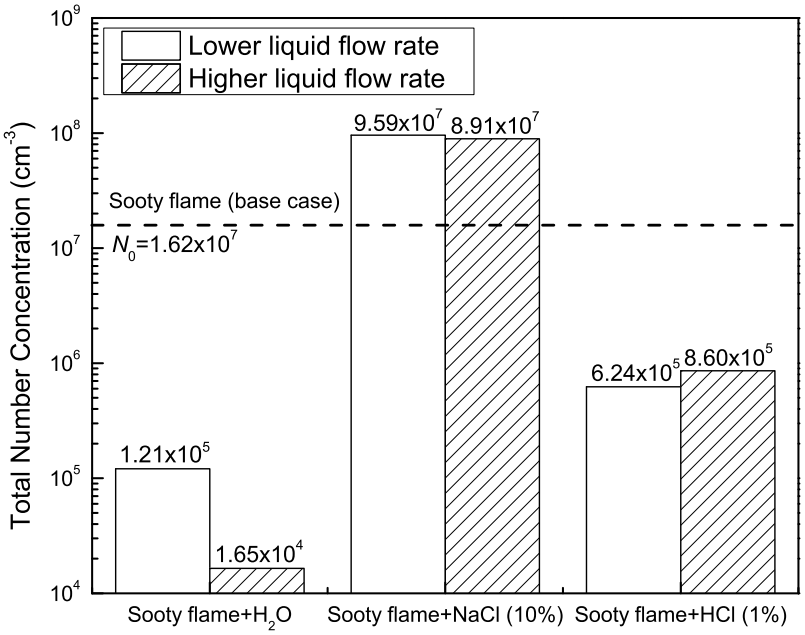

Figure A.5: Total number concentration for sooty flame with various liquid droplets at two different liquid mass ratios

A.3 Mass-Mobility Relationships for Sooty Flame with Various Liquids

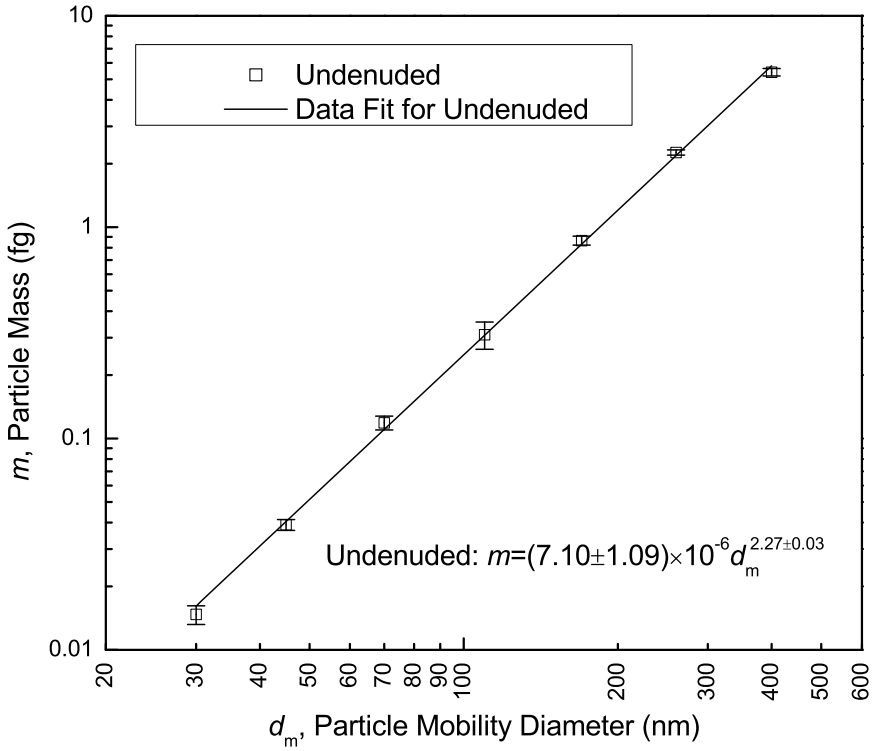

Figure A.6: Mass-mobility measurements for particles from a sooty flame

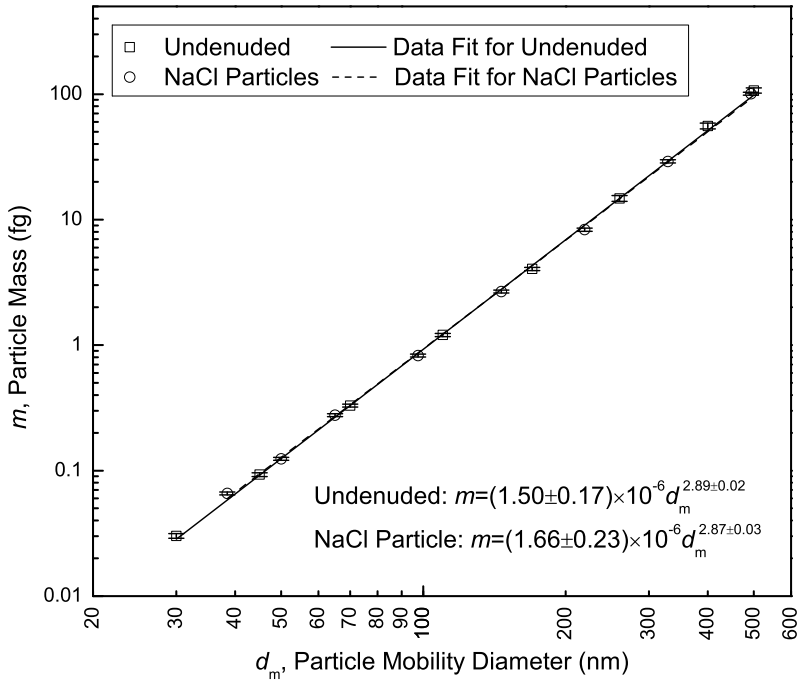

Figure A.7: Mass-mobility measurements for particles from a sooty flame with droplets of sodium chloride solution (10%)

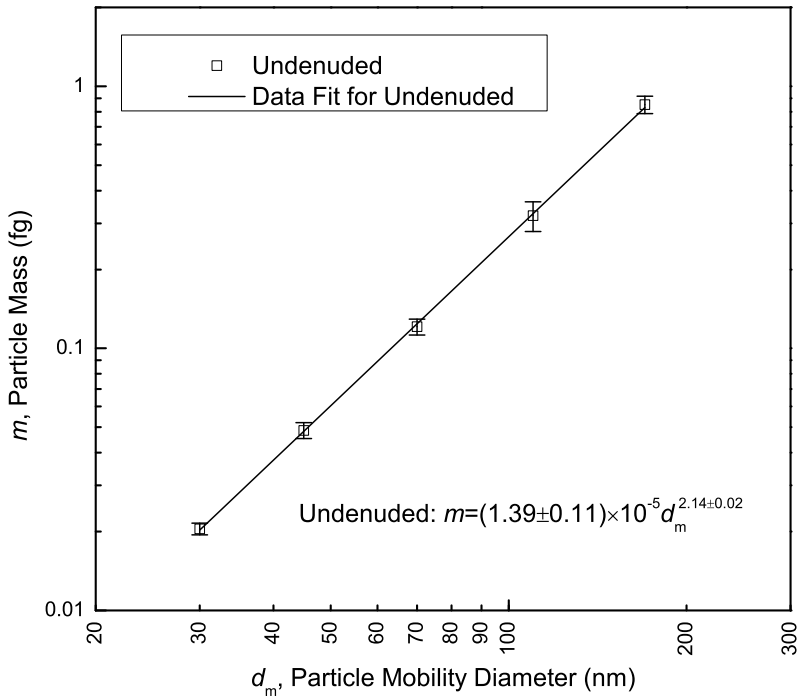

Figure A.8: Mass-mobility measurements for particles from a sooty flame with droplets of hydrochloric acid solution (1%)

A.4 Detection of Multi-species Particles from a Sooty Flame with Sodium Chloride Droplets

A typical mass spectrum from the CPMA (particle concentration with respect to m_p^*) usually consists of one large peak corresponding to singly-charged particles and one or several significantly smaller peaks on its right-hand side for multiply-charged particles. Figure A.9 shows a typical mass spectrum from CPMA for particles with mobility diameter of 110 nm sampled from the sooty diffusion flame with droplets of sodium chloride solution (10%). In this spectrum, the mass of particles with mobility diameter of 110 nm was considered to be equal to the peak value of the large log-normal distribution. This situation was almost the case for particles with relatively small mobility diameter (<250 nm).

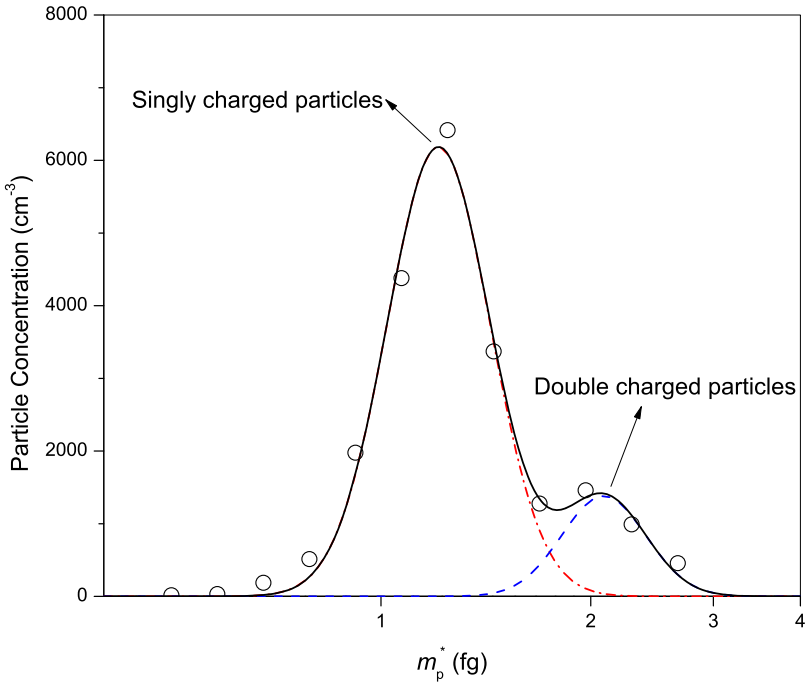

Figure A.9: A typical mass spectrum from CPMA for multiply-charged particles

However, it was noticed in this study that for particles with mobility diameter equal to or larger than 260 nm (*i.e.* 260 nm, 400 nm, and 500 nm), the mass spectrum from the CPMA was skewed to the left-hand side. Figures A.10–A.12 shows mass spectra for particles with mentioned mobility diameter for an arbitrary test. In these figures, the mass spectrum is de-convoluted to obtain two log-normal distributions with two different count median diameters. Presumably, such mass spectrum suggests the presence of two species scanned by CPMA. Assuming that the peak value of each log-normal distribution in the mass spectrum corresponds to the mass of a particle with certain species, the effective density of that species can be obtained based on the known mobility diameter. Table A.1 summarizes the effective density of each species for different scans and mobility diameters.

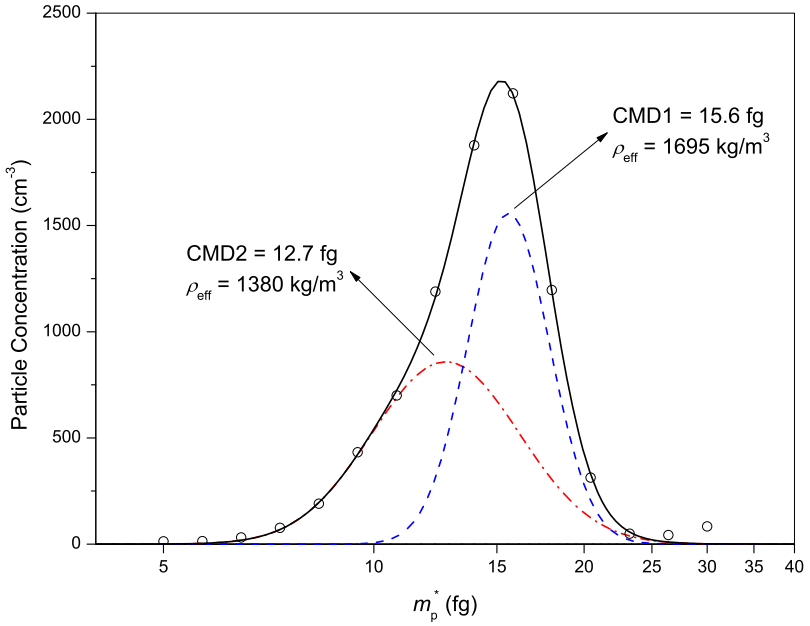

Figure A.10: CPMA mass spectrum for particles with mobility diameter of 260 nm from a sooty flame with droplets of sodium chloride solution (10%)

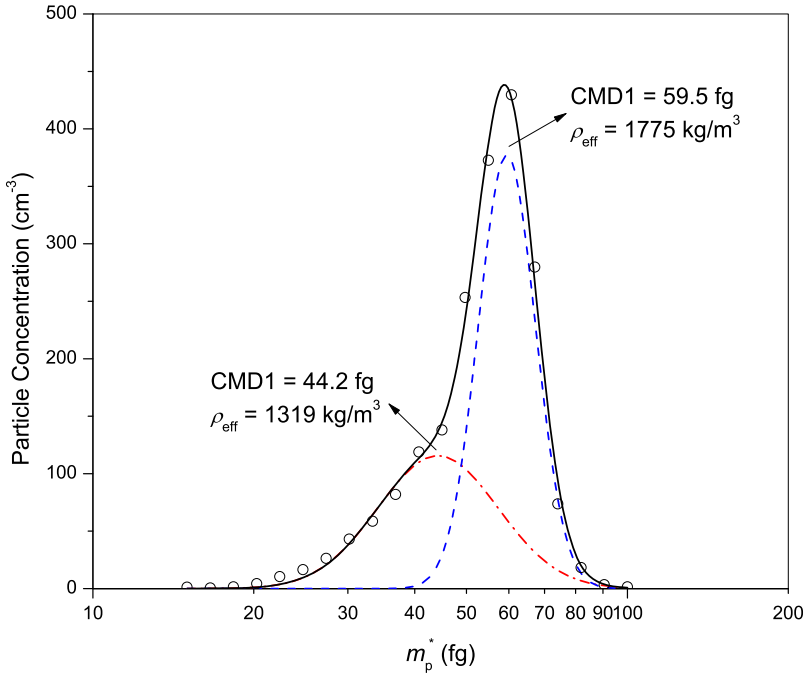

Figure A.11: CPMA mass spectrum for particles with mobility diameter of 400 nm from a sooty flame with droplets of sodium chloride solution (10%)

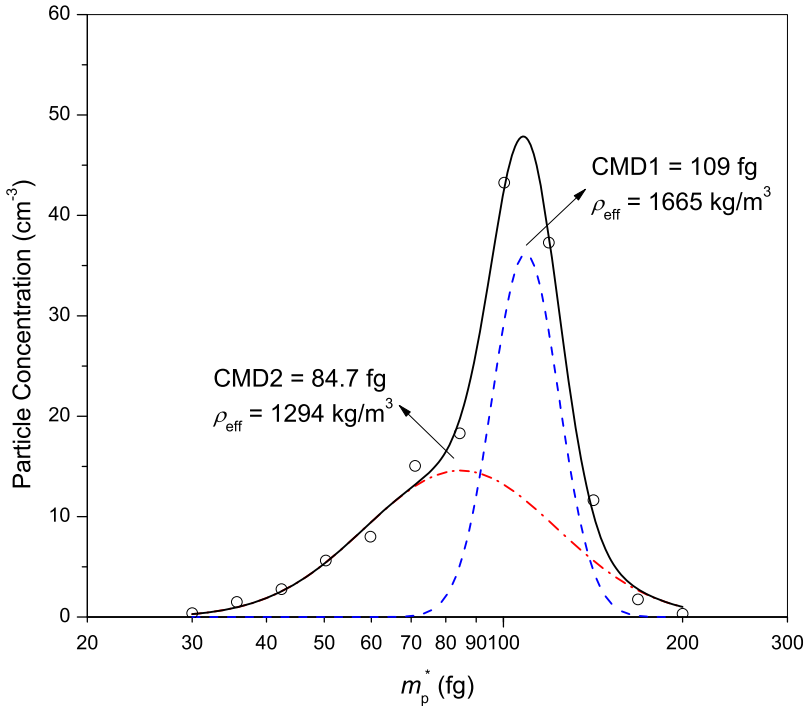

Figure A.12: CPMA mass spectrum for particles with mobility diameter of 500 nm from a sooty flame with droplets of sodium chloride solution (10%)

Table A.1: Effective density of two different species in large particles (260-500 nm) generated in a sooty flame with droplets of NaCl (10%) solution

Mobility diameter (nm)	Effective density of heavier species (kg/m^3)			Effective density of lighter species (kg/m^3)		
	Scan #1	Scan #2	Scan #3	Scan #1	Scan #2	Scan #3
260	1695	1650	1702	1380	1467	1394
400	1775	1666	1740	1319	1326	1339
500	1700	1665	1684	1371	1294	1394

The effective density of the heavier species was close to the density of sodium chloride particles with the same corresponding mobility diameter (see Figure 2.5b). However, the lighter species had an effective density which was between that of sodium chloride (1500-1600 kg/m^3) and soot particles (160-250 kg/m^3) for the concerned particle sizes. Presumably, relatively large particles (~250-500 nm) generated from a sooty diffusion flame with droplets of sodium chloride (10%) consisted of an internal mixture of sodium chloride and soot.

Appendix B Study of volatile material on particulate matter

Arrangement A in the pilot-scale experimental setup (Figure 3.1) was used to investigate the effect of thermodenuding on the particle size distribution. The thermodenuder had a longer tube than the bypass line and the particle numbers had to be corrected for the diffusion and thermophoretic losses in the thermodenuder tube. The penetration, *P*, of the tube is defined as the ratio of the number of particles exiting the tube to the number of particles entering it. The number of particles from the dry flame without and with the thermodenuder at different gas flow rates was determined to obtain the penetration of the thermodenuder at various particles sizes. Figure B.1 shows the average penetration for the thermodenuder at 160°C and flow rate of 0.30 SLPM, along with the fitted curve for the data points.

It was assumed that the dry flame conditions did not produce significant volatile coating on the particles as well as externally mixed semi-volatile particles, hence not interfering with the penetration calculations. Rogak (2014) measured the penetration of the TD used in this study at different flow rates using the inverted burner (S. Rogak, personal communication, February 10, 2014). The inverted burner settings were not expected to produce significant semi-volatile material (Ghazi et al., 2013). The penetration measured by Rogak (2014) for the flow rate of 0.30 SLPM and at 150 °C agreed reasonably with the penetration measured in the current study. This result supported the assumption of non-volatile particles from the studied dry flame.

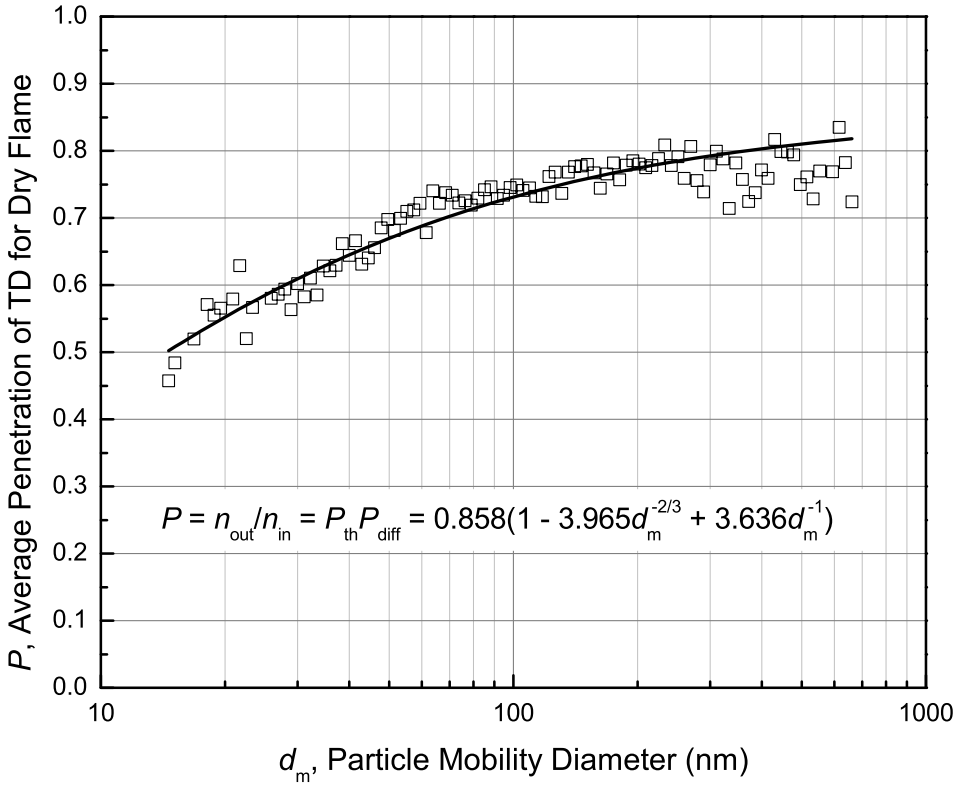

Figure B.1: Average penetration of the thermodenuder measured at 160°C and flow rate of 0.30 SLPM for the dry flames at 5 different fuel flow rates

Thermophoretic losses in laminar pipe flow are nearly independent of flow rate or particle size, and a simple expression for penetration is given by (Housiadas and Drossinos, 2005):

$$P_{\mathrm{th}} = \left(\frac{T_{\mathrm{w}}}{T_0}\right)^{K\,\mathrm{Pr}} \tag{B.1}$$

where T_{w} is the tube wall temperature in the cooling section (~293 K), T_0 is the bulk inlet temperature to the cooling section (i.e. exit temperature of the thermodenuder heating section, or 433 K), K is the thermophoretic coefficient (~0.55 for particles in the transition regime), and Pr is the Prandtl number for air

(~0.71). Substituting the above values in Equation (B.1) results in a constant thermophoretic penetration of $P_{th} = 0.858$.

Diffusion losses, P_{diff}, for a laminar flow in the tube was modeled using the polynomial equation suggested by Hinds (1999) for $\mu = \frac{DL}{Q} < 0.009$, where D is the diffusion coefficient of air, L is the tube length, and Q is the flow rate in the tube.

Housiadas and Drossinos (2005) indicated that it is reasonably accurate to assume that diffusion and thermophoretic losses are not interacting with each other. Therefore, the total penetration of the thermodenuder tube was considered as multiplication of diffusion and thermophoretic penetration. This model was used when fitting the data in Figure B.1. The average penetration function for the thermodenuder was obtained as

$$P = P_{th}P_{diff} = 0.858(1 - 3.965d_m^{-2/3} + 3.636d_m^{-1}) \quad \text{(B.2)}$$

where d_m is the particle mobility diameter. Equation (B.2) was used to correct the size distribution of denuded particles for the effects of diffusion and thermophoretic losses. It should be noted that Equation (B.2) is independent of particle composition and is valid for soot, NaCl, or other particles.

Figures B.2 and B.3 show the undenuded and denuded particles' total concentration and count median diameter (CMD), respectively, for flames without and with liquid droplets. In the case of flame with droplets of NaCl solution, the size distributions were bimodal and the CMD of each mode is compared

separately. It is obvious that the total particle number and count median diameter were almost the same for undenuded and denuded cases. This result suggests that no or very little volatile material was coated on the emitted particles.

References

Housiadas, C., and Drossinos, Y. (2005). Thermophoretic Deposition in Tube Flow. *Aerosol Science and Technology,* 39(4):304-318.

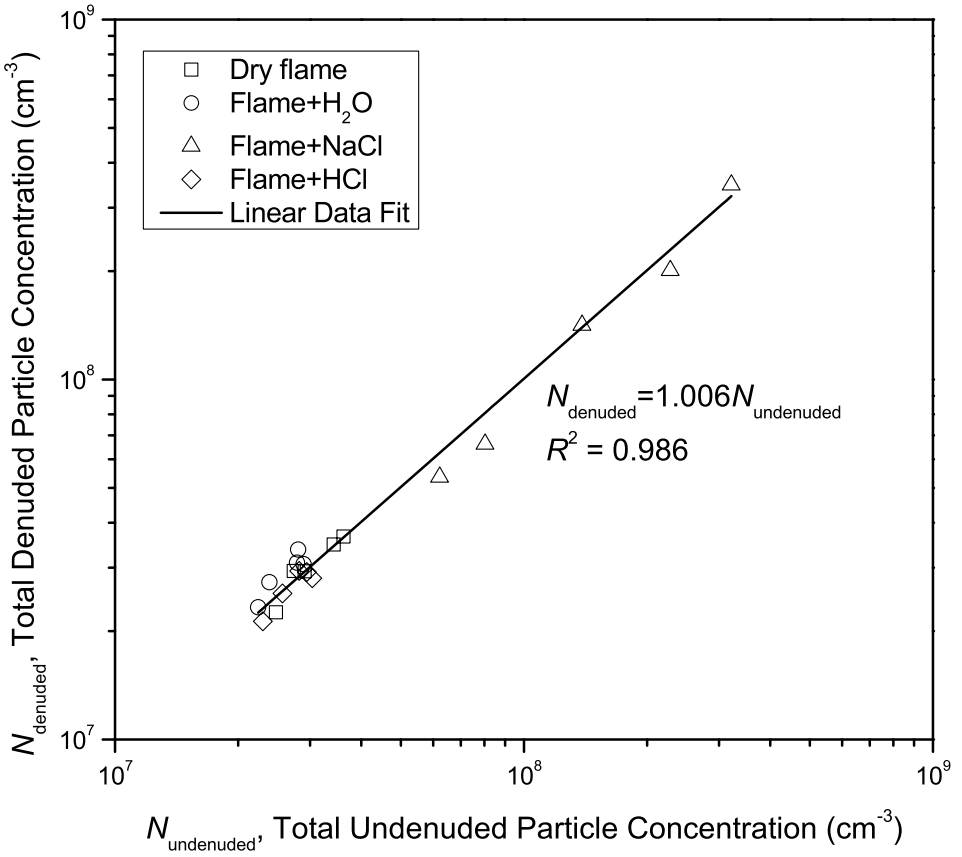

Figure B.1: Undenuded and denuded particles' total concentration for the flame without and with liquid droplets

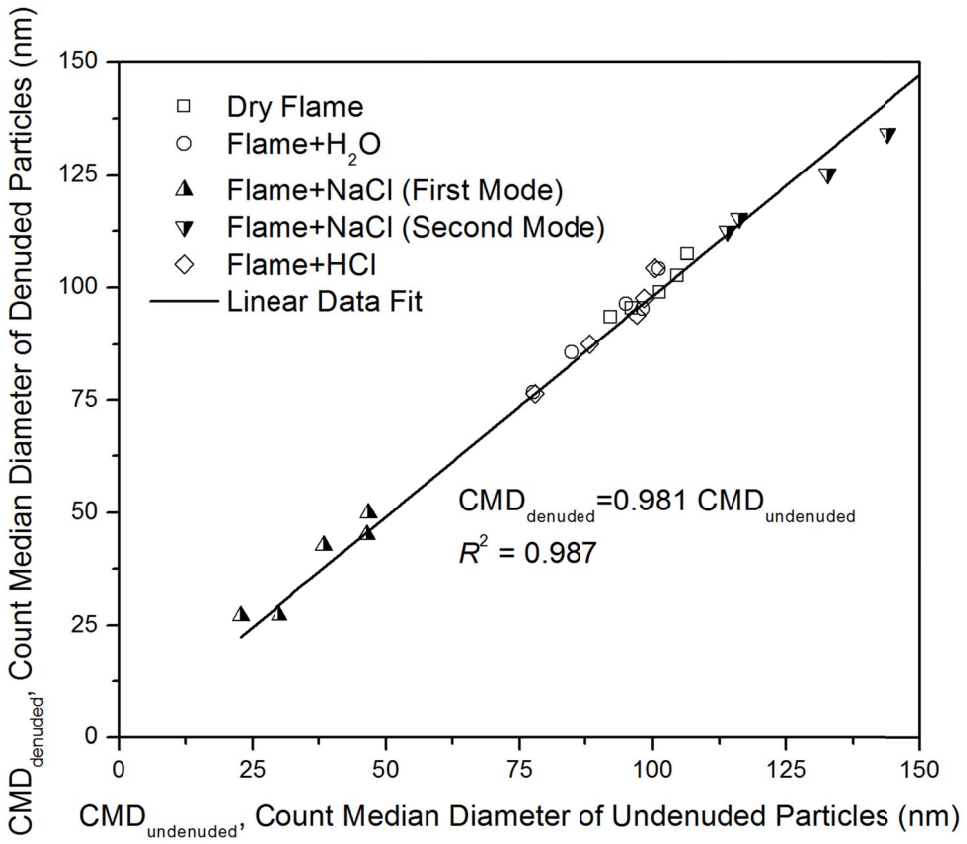

Figure B.2: Undenuded and denuded particles' count median diameter for the flame without and with liquid droplets

Appendix C Calculating molar flow rate of exhaust products, diluted sample in the duct, and particulate matter emission factor

The objective of this section is to find an expression for the molar flow rate of exhaust products and the diluted exhaust mixture in the duct for the pilot-scale flare facility. It was assumed that combustion reaction of flare gas was complete. The assumption of complete combustion was valid because the calculated carbon conversion efficiencies (*i.e.,* combustion efficiencies) in all tested conditions were above 99.8%.

Figure C.1 shows a simple schematic of the combustion process in the flame and the mixing of exhaust products with dilution air in the duct. Two control volumes were considered: Control volume 1 is shown in dashed line, and control volume 2 is shown in dotted line. Subscripts "fuel", "∞", and "duct" indicate fuel mixture, entrained air (defined below), and diluted exhaust mixture in the duct, respectively. Mass is shown by m and mass flow rate is indicated by $\dot{m}$.

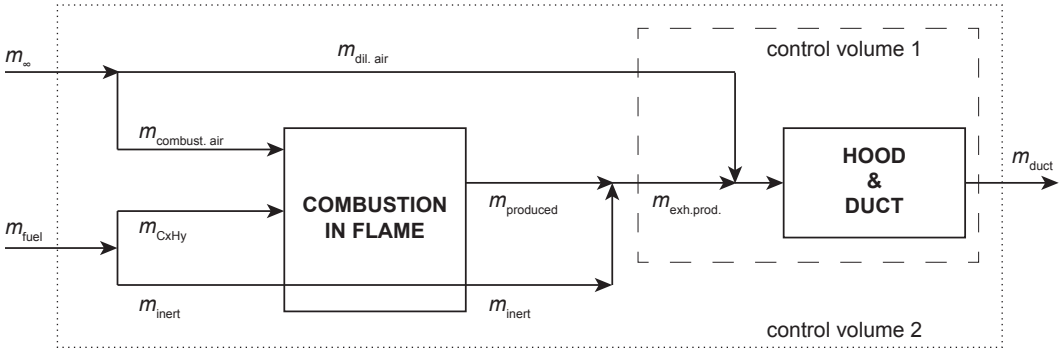

Figure C.1: Schematic of the combustion and diluting processes with the control volumes 1 and 2

In the present study, the fuel mixture was composed of two groups of species: The first group consisted of a mixture of hydrocarbons (its mass simply denoted by $m_{C_xH_y}$) and the second group consisted of inert species of CO_2 and N_2 that passed through the flame without reaction (its mass denoted by m_{inert}). Therefore,

$$\dot{m}_{\text{fuel}} = \dot{m}_{C_xH_y} + \dot{m}_{\text{inert}} \tag{C.1}$$

From Figure C.1, the mass of exhaust products ($m_{\text{exh.prod.}}$) was the sum of mass of the species produced by combustion reaction (m_{produced}) and mass of the inert species in the fuel (m_{inert}). Therefore,

$$\dot{m}_{\text{produced}} + \dot{m}_{\text{inert}} = \dot{m}_{\text{exh.prod.}} \tag{C.2}$$

Figure C.1 also shows that the mass of entrained air (m_{∞}) was the sum of mass of the air required for complete combustion ($m_{\text{comb.air}}$) and mass of the dilution air ($m_{\text{dil.air}}$). Therefore,

$$\dot{m}_{\infty} = \dot{m}_{\text{comb.air}} + \dot{m}_{\text{dil.air}} \tag{C.3}$$

Mass conservation across the boundaries of control volume 1 (dashed line in Figure C.1) yields

$$\dot{m}_{\text{exh.prod.}} + \dot{m}_{\text{dil.air}} = \dot{m}_{\text{duct}} \tag{C.4}$$

Equations (C.1) to (C.4) can be combined to obtain

$$\left(\dot{m}_{\text{produced}} + \dot{m}_{\text{inert}}\right) + (\dot{m}_{\infty} - \dot{m}_{\text{comb.air}}) = \dot{m}_{\text{duct}} \tag{C.5}$$

$$\left(\dot{m}_{\text{produced}} + \dot{m}_{\text{fuel}} - \dot{m}_{\text{C}_x\text{H}_y}\right) + (\dot{m}_{\infty} - \dot{m}_{\text{comb.air}}) = \dot{m}_{\text{duct}} \tag{C.6}$$

Each flow stream (arrowed line in Figure C.1) consisted of various species. For a defined species of choice, denoted by *i*, Equation (C.6) can be written as

$$\left(\dot{m}_{i,\text{produced}} + \dot{m}_{i,\text{fuel}} - \dot{m}_{i,\text{C}_x\text{H}_y}\right) + \left(\dot{m}_{i,\infty} - \dot{m}_{i,\text{comb.air}}\right) = \dot{m}_{i,\text{duct}} \tag{C.7}$$

$$\left(\dot{m}_{i,\text{produced}} + Y_{i,\text{fuel}}\dot{m}_{\text{fuel}} - Y_{i,\text{C}_x\text{H}_y}\dot{m}_{\text{C}_x\text{H}_y}\right) + \left(Y_{i,\infty}\dot{m}_{\infty} - Y_{i,\text{comb.air}}\dot{m}_{\text{comb.air}}\right) = Y_{i,\text{duct}}\dot{m}_{\text{duct}} \tag{C.8}$$

where Y_i is the mass fraction of an arbitrary species *i.* To do a carbon balance, we needed to consider the species in the combustion products of a complete combustion that contains carbon. CO_2 is the only carbon-containing species in the products when a hydrocarbon is combusted completely. The complete combustion of hydrocarbon fuel (C_xH_y) in the dry air was balanced as follows:

$$\text{C}_x\text{H}_y + \left(x + \frac{y}{4}\right)(\text{O}_2 + 3.76\text{N}_2) \rightarrow x\text{CO}_2 + \frac{y}{2}\text{H}_2\text{O} + 3.76\left(x + \frac{y}{4}\right)\text{N}_2 \tag{C.9}$$

For this reaction equation, it was assumed for simplicity that the combustion air was dry and consisted of oxygen and nitrogen only, as shown in Equation (C.9), but the CO_2 in the combustion is included in the mass balances.

Equation (C.8) was re-written for CO_2 as the species of interest as discussed above. The mass fraction of CO_2 in the hydrocarbon part of the fuel is zero (*i.e.,*

$Y_{CO_2,C_xH_y} = 0$). Also, the combustion air and dilution air had the same composition as entrained air. Therefore, for i=CO_2, Equation (C.8) became

$$\dot{m}_{CO_2,\text{produced}} + Y_{CO_2,\text{fuel}}\dot{m}_{\text{fuel}} + Y_{CO_2,\infty}\dot{m}_{\infty} - Y_{CO_2,\infty}\dot{m}_{\text{comb.air}} = Y_{CO_2,\text{duct}}\dot{m}_{\text{duct}} \tag{C.10}$$

In Equation (C.10), it was assumed that any trace species (such as CO_2) present in the entrained air that was a constituent of $\dot{m}_{\infty}$ did not react.

It is more convenient to state Equation (C.10) in terms of mole fraction (X) and molar flow rate ($\dot{n}$), because gas analyzers measure volume fraction of gas species. For an ideal gas, the volume fraction of a species is equal to its mole fraction. To express Equation (C.10) in terms of mole fraction and molar flow rate, the following intermediate relationships between mass fraction and mole fraction of CO_2 in any arbitrary mixture were used,

$$\dot{m}_{CO_2} = Y_{CO_2,\text{mixture}}\dot{m}_{\text{mixture}} \tag{C.11}$$

$$\dot{m}_{CO_2} = \dot{n}_{CO_2}M_{CO_2} = \left(X_{CO_2,\text{mixture}}\dot{n}_{\text{mixture}}\right)M_{CO_2} \tag{C.12}$$

$$Y_{CO_2,\text{mixture}}\dot{m}_{\text{mixture}} = \left(X_{CO_2,\text{mixture}}\dot{n}_{\text{mixture}}\right)M_{CO_2} \tag{C.13}$$

where M_{CO_2} is the molar mass of CO_2 (g/mol). Equations (C.13) and (C.10) were combined and M_{CO_2} was factored from both sides to obtain

$$\dot{n}_{CO_2,\text{produced}} + X_{CO_2,\text{fuel}}\dot{n}_{\text{fuel}} + X_{CO_2,\infty}\dot{n}_{\infty} - X_{CO_2,\infty}\dot{n}_{\text{comb.air}} = X_{CO_2,\text{duct}}\dot{n}_{\text{duct}} \quad \text{(C.14)}$$

The first term on the left-hand-side of Equation (C.14) expresses the molar flow rate of CO_2 produced from the combustion process. According to the stoichiometric reaction shown in Equation (C.9), for one mole of hydrocarbon (C_xH_y) in the fuel, x mole of CO_2 was produced. Therefore,

$$\dot{n}_{CO_2,\text{produced}} = x\dot{n}_{C_xH_y,\text{fuel}} = xX_{C_xH_y,\text{fuel}}\dot{n}_{\text{fuel}} \quad \text{(C.15)}$$

where $\dot{n}_{C_xH_y,\text{fuel}}$ is the molar flow rate of hydrocarbon part of the fuel, which was equal to the mole fraction of hydrocarbon in the fuel multiplied by molar flow rate of the fuel. Similarly,

$$\dot{n}_{\text{comb.air}} = 4.76\left(x + \frac{y}{4}\right)\dot{n}_{C_xH_y,\text{fuel}} = 4.76\left(x + \frac{y}{4}\right)X_{C_xH_y,\text{fuel}}\dot{n}_{\text{fuel}} \quad \text{(C.16)}$$

Equations (C.15) and (C.16) were substituted in Equation (C.14) to obtain

$$xX_{C_xH_y,\text{fuel}}\dot{n}_{\text{fuel}} + X_{CO_2,\text{fuel}}\dot{n}_{\text{fuel}} + X_{CO_2,\infty}\dot{n}_{\infty} - X_{CO_2,\infty} \times 4.76\left(x + \frac{y}{4}\right)X_{C_xH_y,\text{fuel}}\dot{n}_{\text{fuel}} = X_{CO_2,\text{duct}}\dot{n}_{\text{duct}} \quad \text{(C.17)}$$

In Equation (C.17), number of carbon atoms in the hydrocarbon (x), mole fraction of hydrocarbon part in the fuel ($X_{C_xH_y,\text{fuel}}$) molar flow rate of fuel ($\dot{n}_{\text{fuel}}$), mole fraction of the inert CO_2 in the fuel ($X_{CO_2,\text{fuel}}$), mole fraction of CO_2 in the

entrained air or ambient air ($X_{CO_2,\infty}$), mole fraction of CO_2 in the duct ($X_{CO_2,duct}$) were known. Molar flow rate of entrained air ($\dot{n}_\infty$) was not known and we were interested to calculate $\dot{n}_{duct}$. Therefore, it was necessary to omit $\dot{n}_\infty$ in Equation (C.17).

To omit $\dot{n}_\infty$, the general mass conservation for control volume 2 (dotted line in Figure C.1) was used:

$$\dot{n}_{fuel} M_{fuel} + \dot{n}_\infty M_\infty = \dot{n}_{duct} M_{duct} \tag{C.18}$$

Equation (C.18) was re-arranged to obtain $\dot{n}_\infty$ as

$$\dot{n}_\infty = \dot{n}_{duct} \frac{M_{duct}}{M_\infty} - \dot{n}_{fuel} \frac{M_{fuel}}{M_\infty} \tag{C.19}$$

Molar mass in the duct (M_{duct}) depended on dilution ratio and chemical composition of the exhaust products. One way to calculate M_{duct} was to do a mass balance on another element, such as oxygen or hydrogen. Alternatively, we could assume that in the case of the present study with a nearly complete combustion with efficiency above 99.8% and high dilution ratio of 20 to 100, the molar mass in the duct was basically equal to molar mass of ambient air, i.e. $M_{duct} = M_\infty$, and this assumption led to negligible error. For a case with combustion efficiency of 80% and dilution ratio of 10, the deviation in calculated molar mass of diluted exhaust in the duct versus that of air was less than 0.5%. With this simplifying assumption, Equation (C.19) became

$$\dot{n}_{\infty} = \dot{n}_{\text{duct}} - \dot{n}_{\text{fuel}} \frac{M_{\text{fuel}}}{M_{\infty}} \tag{C.20}$$

Substituting Equation (C.20) in Equation (C.17) resulted in

$$\begin{aligned} & X_{\text{CO}_2,\text{duct}} \dot{n}_{\text{duct}} = \\ & x X_{\text{C}_x\text{H}_y,\text{fuel}} \dot{n}_{\text{fuel}} + X_{\text{CO}_2,\text{fuel}} \dot{n}_{\text{fuel}} + X_{\text{CO}_2,\infty} \left(\dot{n}_{\text{duct}} - \dot{n}_{\text{fuel}} \frac{M_{\text{fuel}}}{M_{\infty}} \right) - \\ & X_{\text{CO}_2,\infty} \times 4.76 \left(x + \frac{y}{4} \right) X_{\text{C}_x\text{H}_y,\text{fuel}} \dot{n}_{\text{fuel}} \end{aligned} \tag{C.21}$$

Equation (C.21) was re-grouped for $\dot{n}_{\text{duct}}$ to have

$$\begin{aligned} & \left(X_{\text{CO}_2,\text{duct}} - X_{\text{CO}_2,\infty} \frac{M_{\text{duct}}}{M_{\infty}} \right) \dot{n}_{\text{duct}} = \\ & x X_{\text{C}_x\text{H}_y,\text{fuel}} \dot{n}_{\text{fuel}} + X_{\text{CO}_2,\text{fuel}} \dot{n}_{\text{fuel}} - X_{\text{CO}_2,\infty} \dot{n}_{\text{fuel}} \frac{M_{\text{fuel}}}{M_{\infty}} - \\ & X_{\text{CO}_2,\infty} \times 4.76 \left(x + \frac{y}{4} \right) X_{\text{C}_x\text{H}_y,\text{fuel}} \dot{n}_{\text{fuel}} \end{aligned} \tag{C.22}$$

Equation (C.22) was solved for $\dot{n}_{duct}$:

$$\begin{aligned} & \dot{n}_{\text{duct}} = \frac{\dot{n}_{\text{fuel}}}{X_{\text{CO}_2,\text{duct}} - X_{\text{CO}_2,\infty}} \times \\ & \left[x X_{\text{C}_x\text{H}_y,\text{fuel}} + X_{\text{CO}_2,\text{fuel}} - X_{\text{CO}_2,\infty} \frac{M_{\text{fuel}}}{M_{\infty}} - X_{\text{CO}_2,\infty} \times 4.76 \left(x + \frac{y}{4} \right) X_{\text{C}_x\text{H}_y,\text{fuel}} \right] \end{aligned} \tag{C.23}$$

The molar flow rate of exhaust products could be obtained from Equation (C.9). For one mole of hydrocarbon (C_xH_y), x mole of CO_2, $\frac{y}{2}$ mole of H_2O, and $3.76\left(x+\frac{y}{4}\right)$ mole of N_2 was produced. For the known molar flow rates of hydrocarbon ($\dot{n}_{C_xH_y,\text{fuel}}$) and inert species ($\dot{n}_{CO_2,\text{fuel}}$, $\dot{n}_{N_2,\text{fuel}}$) in the fuel,

$$\dot{n}_{\text{exh.prod.}} = \left(3.76\left(x+\frac{y}{4}\right)+x+\frac{y}{2}\right)\dot{n}_{C_xH_y,\text{fuel}} + \dot{n}_{CO_2,\text{fuel}} + \dot{n}_{N_2,\text{fuel}} \qquad \text{(C.24)}$$

The molar flow rate of the hydrocarbon part of the fuel was equal to the mole fraction of hydrocarbon in the fuel multiplied by molar flow rate of the fuel. Therefore,

$$\dot{n}_{\text{exh.prod.}} = \left(3.76\left(x+\frac{y}{4}\right)+x+\frac{y}{2}\right)X_{C_xH_y}\dot{n}_{\text{fuel}} + X_{CO_2}\dot{n}_{\text{fuel}} + X_{N_2}\dot{n}_{\text{fuel}} \qquad \text{(C.25)}$$

Equation (C.25) could be re-stated in terms of mass flow rates which were readily measurable in this study:

$$\dot{n}_{\text{exh.prod.}} = \left[\left(3.76\left(x+\frac{y}{4}\right)+x+\frac{y}{2}\right)X_{C_xH_y} + X_{CO_2} + X_{N_2}\right]\frac{\dot{m}_{\text{fuel}}}{M_{\text{fuel}}} \qquad \text{(C.26)}$$

Furthermore, dilution ratio (DR) was defined as

$$\text{DR} = \frac{\dot{n}_{\text{dil.air}}}{\dot{n}_{\text{exh.prod.}}} = \frac{\dot{n}_{\text{duct}}}{\dot{n}_{\text{exh.prod.}}} - 1 \qquad \text{(C.27)}$$

where $\dot{n}_{\text{dil.air}}$ is the mole flow rate of dilution air, $\dot{n}_{\text{exh.prod.}}$ is the mole flow rate of exhaust products, and $\dot{n}_{\text{duct}}$ is the mole flow rate of the diluted exhaust products in the duct which is the sum of $\dot{n}_{\text{dil.air}}$ and $\dot{n}_{\text{exh.prod.}}$

The soot volume fraction of a sample measured by LII, $f_{v,\text{LII}}$, is defined as $f_{v,\text{LII}} = V_{\text{soot}}/V_{\text{sample air}}$, where V_{soot} is the volume of soot in the sample air analyzed by LII and $V_{\text{sample air}}$ is the volume of sample air. Because of the difference in the temperature between the measurement cell of LII and the duct, the actual soot volume fraction in the duct was calculated as follows assuming ideal gas behaviour:

$$f_{v,\text{duct}} = f_{v,\text{LII}} \left(\frac{T_{\text{LII}}}{T_{\text{duct}}} \right) \tag{C.28}$$

where $f_{v,\text{duct}}$ is the soot volume fraction in the duct, T_{LII} is the temperature of the measurement cell of LII (K), and T_{duct} is the temperature of the diluted exhaust products in the duct (K). By using the ideal gas law, the mass emission rate of soot in the duct was further obtained as

$$\dot{m}_{\text{soot}} = \rho_{\text{soot}} \, f_{v,\text{duct}} \, \frac{\dot{n}_{\text{duct}} \, R \, T_{\text{duct}}}{P_{\text{stat}}} \tag{C.29}$$

where ρ_{soot} is the density of soot (kg/m^3), R is the ideal gas constant (8.314 J/mol·K), and P_{stat} is the static pressure.

Soot mass emission factor, Y_{LII}, which is defined as the mass of soot particles per mass of fuel, could be found by combining Equations (C.28) and (C.29).

$$Y_{\mathrm{LII}} = \frac{\dot{m}_{\mathrm{soot}}}{\dot{m}_{\mathrm{fuel}}} = \frac{\rho_{\mathrm{soot}}\ f_{v,\,\mathrm{LII}}\ \dot{n}_{\mathrm{duct}}\ R\ T_{\mathrm{LII}}}{\dot{m}_{\mathrm{fuel}}\ P_{\mathrm{stat}}} \tag{C.30}$$

Particle mass emission factor measured by SMPS, Y_{SMPS}, could be obtained in a similar way, considering ideal gas behaviour and correcting for temperature difference between the CPC manufacturer's standard conditions (21.1 °C) and the duct. After measuring PM mass distribution and integrating to obtain the PM mass per unit volume of air at 21.1 °C (see section 3.3.4.3 for details), the emission factor measured by SMPS can be calculated as

$$Y_{\mathrm{SMPS}} = \frac{\dot{m}_{\mathrm{PM}}}{\dot{m}_{\mathrm{fuel}}} = \frac{\dfrac{m_{\mathrm{PM}}}{V_{\mathrm{air@}T_{\mathrm{duct}}}} \times \dfrac{\dot{n}_{\mathrm{duct}}\ R\ T_{\mathrm{duct}}}{P_{\mathrm{stat}}}}{\dot{m}_{\mathrm{fuel}}} \tag{C.31}$$

$$V_{\mathrm{air@}T_{\mathrm{duct}}} = V_{\mathrm{air@}T_{\mathrm{CPC}}} \left(\frac{T_{\mathrm{duct}}}{T_{\mathrm{CPC}}} \right) \tag{C.32}$$

$$\begin{aligned} Y_{\mathrm{SMPS}} &= \frac{\dfrac{m_{\mathrm{PM}}}{V_{\mathrm{air@}T_{\mathrm{CPC}}}}\ \dot{n}_{\mathrm{duct}}\ R\ T_{\mathrm{CPC}}}{\dot{m}_{\mathrm{fuel}}\ P_{\mathrm{stat}}} \\ &= \frac{(\text{mass of PM per volume of air } @T_{\mathrm{CPC}})\ \dot{n}_{\mathrm{duct}}\ R\ T_{\mathrm{CPC}}}{\dot{m}_{\mathrm{fuel}}\ P_{\mathrm{stat}}} \end{aligned} \tag{C.33}$$

Number emission factor was calculated similar to Equation (C.33) as

$$\frac{N_{\mathrm{PM}}}{\dot{m}_{\mathrm{fuel}}} = \frac{(\text{number of PM per volume of air } @T_{\mathrm{CPC}})\ \dot{n}_{\mathrm{duct}}\ R\ T_{\mathrm{CPC}}}{\dot{m}_{\mathrm{fuel}}\ P_{\mathrm{stat}}} \tag{C.34}$$

where number of PM per volume of air (i.e. total particle concentration) is the integral of particle size distribution curves shown in Figure 3.3.

Appendix D Uncertainty analysis of emission factors

A comprehensive uncertainty analysis of the reported emission factors was conducted based on ANSI/ASME Measurement Uncertainty Standard (1985). According to this standard, total uncertainty of a measurement consists of contributions from "bias" uncertainty (also known as systematic or instrument error) and "precision" uncertainty (alternatively called repeatability uncertainty). The bias uncertainty is the error of the instrument to read the correct value of a measurement. The precision uncertainty represents the scatter in repeated measurements of a quantity. In the current study with pilot-scale flare experiment, each experiment was conducted only once and, therefore, only bias uncertainty is considered.

The bias uncertainty of each instrument (or measurement) is propagated through to the final reported value for emission factors. In this appendix, the detailed calculations for propagation of uncertainty are described.

D.1 Bias uncertainty in molar flow rate of diluted products in the duct

The molar flow rate of diluted exhaust products in the duct ($\dot{n}_{\text{duct}}$) appears in all emission factor calculations and, therefore, it is worth obtaining the bias uncertainty of this quantity first. As described in Appendix C, the molar flow rate of diluted products in the duct is expressed as

$$\dot{n}_{\text{duct}} = \frac{\dot{n}_{\text{fuel}}}{X_{\text{CO}_2,\text{duct}} - X_{\text{CO}_2,\infty}} \times \left[x X_{\text{C}_x\text{H}_y,\text{fuel}} + X_{\text{CO}_2,\text{fuel}} - X_{\text{CO}_2,\infty} \frac{M_{\text{fuel}}}{M_\infty} - X_{\text{CO}_2,\infty} \times 4.76 \left(x + \frac{y}{4} \right) X_{\text{C}_x\text{H}_y,\text{fuel}} \right] \tag{D.1}$$

Assuming that molecular masses (M), x, and y are constant and do not have any bias uncertainty, we can propagate the uncertainty as follows:

$$\begin{aligned} &(\Delta \dot{n}_{\text{duct}})^2 \\ &= \left(\frac{\partial \dot{n}_{\text{duct}}}{\partial \dot{n}_{\text{fuel}}} \right)^2 (\Delta \dot{n}_{\text{fuel}})^2 + \left(\frac{\partial \dot{n}_{\text{duct}}}{\partial X_{\text{CO}_2,\text{duct}}} \right)^2 \left(\Delta X_{\text{CO}_2,\text{duct}} \right)^2 \\ &+ \left(\frac{\partial \dot{n}_{\text{duct}}}{\partial X_{\text{CO}_2,\infty}} \right)^2 \left(\Delta X_{\text{CO}_2,\infty} \right)^2 + \left(\frac{\partial \dot{n}_{\text{duct}}}{\partial X_{\text{C}_x\text{H}_y,\text{fuel}}} \right)^2 \left(\Delta X_{\text{C}_x\text{H}_y,\text{fuel}} \right)^2 \\ &+ \left(\frac{\partial \dot{n}_{\text{duct}}}{\partial X_{\text{CO}_2,\text{fuel}}} \right)^2 \left(\Delta X_{\text{CO}_2,\text{fuel}} \right)^2 \end{aligned} \tag{D.2}$$

By substituting Equation (D.1), the five terms in Equation (D.2) can be expanded as

Term 1:

$$\left[\frac{x X_{\text{C}_x\text{H}_y,\text{fuel}} + X_{\text{CO}_2,\text{fuel}} - X_{\text{CO}_2,\infty} \frac{M_{\text{fuel}}}{M_\infty} - X_{\text{CO}_2,\infty} \times 4.76 \left(x + \frac{y}{4} \right) X_{\text{C}_x\text{H}_y,\text{fuel}}}{X_{\text{CO}_2,\text{duct}} - X_{\text{CO}_2,\infty}} \right]^2 \times (\Delta \dot{n}_{\text{fuel}})^2 \tag{D.3}$$

Term 2:

$$\left[\frac{-\dot{n}_{\text{fuel}} \, \Delta X_{\text{CO}_2,\text{duct}}}{\left(X_{\text{CO}_2,\text{duct}} - X_{\text{CO}_2,\infty} \right)^2} \right]^2 \times \left[x X_{\text{C}_x\text{H}_y,\text{fuel}} + X_{\text{CO}_2,\text{fuel}} - X_{\text{CO}_2,\infty} \frac{M_{\text{fuel}}}{M_\infty} - X_{\text{CO}_2,\infty} 4.76 \left(x + \frac{y}{4} \right) X_{\text{C}_x\text{H}_y,\text{fuel}} \right]^2 \tag{D.4}$$

Term 3:

$$\left[\frac{\dot{n}_{\text{fuel}}\,\Delta X_{\text{CO}_2,\infty}}{\left(X_{\text{CO}_2,\text{duct}}-X_{\text{CO}_2,\infty}\right)^2}\right]^2 \times\left[\left(-\frac{M_{\text{fuel}}}{M_\infty}-4.76\left(x+\frac{y}{4}\right)X_{\text{C}_x\text{H}_y,\text{fuel}}\right)\left(X_{\text{CO}_2,\text{duct}}-X_{\text{CO}_2,\infty}\right)+ xX_{\text{C}_x\text{H}_y,\text{fuel}}+X_{\text{CO}_2,\text{fuel}}-X_{\text{CO}_2,\infty}\frac{M_{\text{fuel}}}{M_\infty}-X_{\text{CO}_2,\infty}4.76\left(x+\frac{y}{4}\right)X_{\text{C}_x\text{H}_y,\text{fuel}}\right]^2 \tag{D.5}$$

Term 4:

$$\left[\frac{\dot{n}_{\text{fuel}}x-4.76\left(x+\frac{y}{4}\right)X_{\text{CO}_2,\infty}}{X_{\text{CO}_2,\text{duct}}-X_{\text{CO}_2,\infty}}\right]^2\times\left(\Delta X_{\text{C}_x\text{H}_y,\text{fuel}}\right)^2 \tag{D.6}$$

Term 5:

$$\left[\frac{\dot{n}_{\text{fuel}}}{X_{\text{CO}_2,\text{duct}}-X_{\text{CO}_2,\infty}}\right]^2\times\left(\Delta X_{\text{CO}_2,\text{fuel}}\right)^2 \tag{D.7}$$

The bias uncertainty of mole fraction of CO_2 in the duct and in the ambient air ($X_{\text{CO}_2,\text{duct}}$ and $X_{\text{CO}_2,\infty}$, respectively) measured by the gas analyzer was the larger of 2% of measured value or the lowest detectable limit. Therefore, the uncertainty of $X_{\text{CO}_2,\text{duct}}$ and $X_{\text{CO}_2,\infty}$ was in the order of 10^{-4} and 10^{-5}, respectively. Based on this, Equations (D.4) and (D.5) become at least of the order of 10^{-8} and 10^{-10}, respectively, which are negligible compared to Equations (D.3), (D.6), and (D.7). Therefore, Equation (D.2) simplifies as

$$(\Delta\dot{n}_{\text{duct}})^2 = \left[\frac{xX_{C_xH_y,\text{fuel}} + X_{CO_2,\text{fuel}} - X_{CO_2,\infty}\frac{M_{\text{fuel}}}{M_\infty} - X_{CO_2,\infty} \times 4.76\left(x+\frac{y}{4}\right)X_{C_xH_y,\text{fuel}}}{X_{CO_2,\text{duct}} - X_{CO_2,\infty}}\right]^2 \times (\Delta\dot{n}_{\text{fuel}})^2 + \left[\frac{\dot{n}_{\text{fuel}}x - 4.76\left(x+\frac{y}{4}\right)X_{CO_2,\infty}}{X_{CO_2,\text{duct}} - X_{CO_2,\infty}}\right]^2 \times \left(\Delta X_{C_xH_y,\text{fuel}}\right)^2 + \left[\frac{\dot{n}_{\text{fuel}}}{X_{CO_2,\text{duct}} - X_{CO_2,\infty}}\right]^2 \times \left(\Delta X_{CO_2,\text{fuel}}\right)^2 \quad \text{(D.8)}$$

In Equation (D.8), the bias uncertainty in $\dot{n}_{\text{fuel}}$ can be obtained by

$$\Delta\dot{n}_{\text{fuel}} = \frac{\Delta\dot{m}_{\text{fuel}}}{M_{\text{fuel}}} \quad \text{(D.9)}$$

The fuel mass flow rate is

$$\dot{m}_{\text{fuel}} = \dot{m}_{CH_4} + \dot{m}_{C_2H_6} + \dot{m}_{C_3H_8} + \dot{m}_{C_4H_{10}} + \dot{m}_{CO_2} + \dot{m}_{N_2} \quad \text{(D.10)}$$

Therefore, the uncertainty in fuel mass flow rate ($\Delta\dot{m}_{\text{fuel}}$) is

$$\Delta\dot{m}_{\text{fuel}} = \sqrt{\left(\Delta\dot{m}_{CH_4}\right)^2 + \left(\Delta\dot{m}_{C_2H_6}\right)^2 + \left(\Delta\dot{m}_{C_3H_8}\right)^2 + \left(\Delta\dot{m}_{C_4H_{10}}\right)^2 + \left(\Delta\dot{m}_{CO_2}\right)^2 + \left(\Delta\dot{m}_{N_2}\right)^2} \quad \text{(D.11)}$$

The relative bias uncertainty of each mass flow controller was 1.25% of the set point. Therefore, Equation (D.11) can be simplified as

$$\Delta\dot{m}_{\text{fuel}} = 0.0125\sqrt{\left(\dot{m}_{CH_4}\right)^2 + \left(\dot{m}_{C_2H_6}\right)^2 + \left(\dot{m}_{C_3H_8}\right)^2 + \left(\dot{m}_{C_4H_{10}}\right)^2 + \left(\dot{m}_{CO_2}\right)^2 + \left(\dot{m}_{N_2}\right)^2} \quad \text{(D.12)}$$

In Equation (D.8), the bias uncertainty of $X_{C_xH_y,\text{fuel}}$ can be obtained as

$$X_{C_xH_y,\text{fuel}} = \frac{\frac{\dot{m}_{C_xH_y,\text{fuel}}}{M_{C_xH_y}}}{\frac{\dot{m}_{\text{fuel}}}{M_{\text{fuel}}}} = \frac{M_{\text{fuel}}}{M_{C_xH_y}} \times \frac{\dot{m}_{C_xH_y,\text{fuel}}}{\dot{m}_{\text{fuel}}} \tag{D.13}$$

$$\begin{aligned} &\left(\Delta X_{C_xH_y,\text{fuel}}\right)^2 \\ &= \left(\frac{M_{\text{fuel}}}{M_{C_xH_y}\dot{m}_{\text{fuel}}}\right)^2 \left(\Delta\dot{m}_{C_xH_y,\text{fuel}}\right)^2 + \left(\frac{-M_{\text{fuel}}\dot{m}_{C_xH_y,\text{fuel}}}{M_{C_xH_y}(\dot{m}_{\text{fuel}})^2}\right)^2 (\Delta\dot{m}_{\text{fuel}})^2 \end{aligned} \tag{D.14}$$

where $\Delta\dot{m}_{C_xH_y,\text{fuel}}$ is calculated similar to Equation (D.12):

$$\Delta\dot{m}_{C_xH_y,\text{fuel}} = 0.0125\sqrt{\left(\dot{m}_{CH_4}\right)^2 + \left(\dot{m}_{C_2H_6}\right)^2 + \left(\dot{m}_{C_3H_8}\right)^2 + \left(\dot{m}_{C_4H_{10}}\right)^2} \tag{D.15}$$

Similarly, the bias uncertainty in $X_{CO_2,\text{fuel}}$ can be obtained as

$$\begin{aligned} &\left(\Delta X_{CO_2,\text{fuel}}\right)^2 = \\ &\left(\frac{M_{\text{fuel}}}{M_{CO_2}\dot{m}_{\text{fuel}}}\right)^2 \left(\Delta\dot{m}_{CO_2,\text{fuel}}\right)^2 + \left(\frac{-M_{\text{fuel}}\dot{m}_{CO_2,\text{fuel}}}{M_{CO_2}(\dot{m}_{\text{fuel}})^2}\right)^2 (\Delta\dot{m}_{\text{fuel}})^2 \end{aligned} \tag{D.16}$$

where $\Delta\dot{m}_{CO_2,\text{fuel}}$ is

$$\Delta\dot{m}_{CO_2,\text{fuel}} = 0.0125\,\dot{m}_{CO_2,\text{fuel}} \tag{D.17}$$

D.2 Bias uncertainty in mass emission factor measured by LII

As shown in Appendix C, the mass emission factor measured by LII is calculated as follows

$$Y_{\mathrm{LII}} = \frac{\dot{m}_{\mathrm{soot}}}{\dot{m}_{\mathrm{fuel}}} = \frac{\rho_{\mathrm{soot}}\ f_{v,\,\mathrm{LII}}\ \dot{n}_{\mathrm{duct}}\ R\ T_{\mathrm{LII}}}{\dot{m}_{\mathrm{fuel}}\ P_{\mathrm{stat}}} \tag{D.18}$$

Equation (D.18) is a purely multiplicative formula; therefore, the relative bias uncertainty of the mass emission factor can be obtained as

$$\frac{\Delta Y_{\mathrm{LII}}}{Y_{\mathrm{LII}}} = \sqrt{\left(\frac{\Delta\rho_{\mathrm{soot}}}{\rho_{\mathrm{soot}}}\right)^2 + \left(\frac{\Delta f_{v,\,\mathrm{LII}}}{f_{v,\,\mathrm{LII}}}\right)^2 + \left(\frac{\Delta\dot{n}_{\mathrm{duct}}}{\dot{n}_{\mathrm{duct}}}\right)^2 + \left(\frac{\Delta T_{\mathrm{LII}}}{T_{\mathrm{LII}}}\right)^2 + \left(\frac{\Delta\dot{m}_{\mathrm{fuel}}}{\dot{m}_{\mathrm{fuel}}}\right)^2 + \left(\frac{\Delta P_{\mathrm{stat}}}{P_{\mathrm{stat}}}\right)^2} \tag{D.19}$$

In Equation (D.19), the uncertainty of soot true density ($\Delta\rho_{\mathrm{soot}}$) is considered as 70 kg/m^3, which is the precision uncertainty of reported values for soot density in the literature with a 95% confidence interval (Dobbins et al., 1994; Choi et al., 1994; Choi et al., 1995; Wu et al., 1997; Park et al., 2004). Although this value did not account for the systematic error in the measurement of soot density, it was the best estimate for the associated uncertainty. The relative bias uncertainty of soot volume fraction measured by LII is considered as 20% (McEwen, 2010). The bias uncertainties of $\dot{n}_{\mathrm{duct}}$ and $\dot{m}_{\mathrm{fuel}}$ are calculated from Equations (D.8) and (D.12), respectively. The uncertainty in temperature (ΔT) and static pressure (ΔP_{stat}) was 2.2 K and 15 Pa, respectively.

D.3 Bias uncertainty in mass emission factor measured by SMPS

It was shown in Appendix C that the mass emission factor measured by SMPS is calculated by

$$Y_{\mathrm{SMPS}} = \frac{(\text{PM mass concentration } @T_{\mathrm{CPC}})\, \dot{n}_{\mathrm{duct}}\, R\, T_{\mathrm{CPC}}}{\dot{m}_{\mathrm{fuel}}\, P_{\mathrm{stat}}} \tag{D.20}$$

Total PM mass concentration, M_{tot}, is obtained from Equation (3.8). Therefore, the relative bias uncertainty of the emission factor expressed in Equation (D.20) can be obtained by

$$\frac{\Delta Y_{\mathrm{SMPS}}}{Y_{\mathrm{SMPS}}} = \sqrt{\left(\frac{\Delta M_{\mathrm{tot}}}{M_{\mathrm{tot}}}\right)^2 + \left(\frac{\Delta \dot{n}_{\mathrm{duct}}}{\dot{n}_{\mathrm{duct}}}\right)^2 + \left(\frac{\Delta T_{\mathrm{LII}}}{T_{\mathrm{LII}}}\right)^2 + \left(\frac{\Delta \dot{m}_{\mathrm{fuel}}}{\dot{m}_{\mathrm{fuel}}}\right)^2 + \left(\frac{\Delta P_{\mathrm{stat}}}{P_{\mathrm{stat}}}\right)^2} \tag{D.21}$$

The last four terms in Equation (D.21) can be calculated similar to section D.2. The bias uncertainty of total PM mass concentration (ΔM_{tot}) can be obtained as follows:

$$M_{\mathrm{tot}} = \sum_{i=1}^{n} m_{\mathrm{bin},i} \tag{D.22}$$

where $m_{\mathrm{bin},i}$ is the mass of particles in size bin i and n is the number of size bins in the particle size distribution. However, $m_{\mathrm{bin},i}$ can be expressed as

$$m_{\mathrm{bin},i} = m_{\mathrm{p,bin}\,i} \times N_{\mathrm{bin},i} \tag{D.23}$$

where $N_{\mathrm{bin},i}$ is the number of particles in bin i and $m_{\mathrm{p,bin}\,i}$ is the mass of each particle in bin i, which is obtained from the mass-mobility relationships shown in Equation (3.9). In general, the mass-mobility relationship has the following form:

$$m_{\mathrm{p,bin}\,i} = k\, d_{\mathrm{m}}^{D_m} \tag{D.24}$$

where k is a coefficient, d_{m} is the particle mobility diameter, and D_m is the mass-mobility exponent. By propagating the uncertainty of each of these three quantities, the total bias uncertainty of $m_{\mathrm{p,bin}\,i}$ can be obtained as

$$\begin{aligned}&\left(\Delta m_{\mathrm{p,bin}\,i}\right)^2 = \\ &\left(\frac{\partial m_{\mathrm{p,bin}\,i}}{\partial k}\right)^2 (\Delta k)^2 + \left(\frac{\partial m_{\mathrm{p,bin}\,i}}{\partial d_{\mathrm{m}}}\right)^2 (\Delta d_{\mathrm{m}})^2 + \left(\frac{\partial m_{\mathrm{p,bin}\,i}}{\partial D_m}\right)^2 (\Delta D_m)^2\end{aligned} \tag{D.25}$$

Equation (D.25) can be expanded as

$$\begin{aligned}&\left(\Delta m_{\mathrm{p,bin}\,i}\right)^2 = \\ &\left(d_{\mathrm{m}}^{D_m}\right)^2 (\Delta k)^2 + \left(k D_m d_{\mathrm{m}}^{D_m-1}\right)^2 (\Delta d_{\mathrm{m}})^2 + \left(k d_{\mathrm{m}}^{D_m} \ln d_{\mathrm{m}}\right)^2 (\Delta D_m)^2\end{aligned} \tag{D.26}$$

It is obvious that the uncertainty of $m_{\mathrm{p,bin}\,i}$ is dependent on mobility diameter and, therefore, is different for each size bin.

By propagating the uncertainty in Equation (D.23),

$$\frac{\Delta m_{\mathrm{bin},i}}{m_{\mathrm{bin},i}} = \sqrt{\left(\frac{\Delta m_{\mathrm{p,bin}\,i}}{m_{\mathrm{p,bin}\,i}}\right)^2 + \left(\frac{\Delta N_{\mathrm{bin},i}}{N_{\mathrm{bin},i}}\right)^2} \tag{D.27}$$

where the relative bias uncertainty in particle number of each bin, *i.e.* $\frac{\Delta N_{\mathrm{bin},i}}{N_{\mathrm{bin},i}}$, is 10% according to the CPC manufacturer and $\Delta m_{\mathrm{p,bin}\,i}$ can be calculated from Equation (D.26).

The bias uncertainty in total particle mass concentration (ΔM_{tot}) is the sum of bias uncertainty of the particle mass in each size bin, *i.e.*,

$$\Delta M_{\text{tot}} = \sum_{i=1}^{n} \Delta m_{\text{bin},i} \tag{D.28}$$

By combining Equations (D.22), (D.27), and (D.28), the relative bias uncertainty of M_{tot} can be calculated as follows:

$$\frac{\Delta M_{\text{tot}}}{M_{\text{tot}}} = \frac{\sum_{i=1}^{n} \Delta m_{\text{bin},i}}{\sum_{i=1}^{n} m_{\text{bin},i}} \tag{D.29}$$

The relative bias uncertainty of mass emission factor can be simply obtained by substituting Equation (D.29) in Equation (D.21).

D.4 Bias uncertainty in number emission factor measured by SMPS

As shown in Appendix C, number emission factor measured by SMPS can be calculated from

$$\frac{N_{\text{PM}}}{\dot{m}_{\text{fuel}}} = \frac{(\text{number of PM per volume of air } @T_{\text{CPC}})\, \dot{n}_{\text{duct}}\, R\, T_{\text{CPC}}}{\dot{m}_{\text{fuel}}\, P_{\text{stat}}} \tag{D.30}$$

Similar to Equations (D.19) and (D.21), the relative bias uncertainty of number emission factor can be obtained as

$$\frac{\Delta\left(\frac{N_{PM}}{\dot{m}_{fuel}}\right)}{\left(\frac{N_{PM}}{\dot{m}_{fuel}}\right)} = \frac{}{\sqrt{\left(\frac{\Delta N}{N}\right)^2 + \left(\frac{\Delta \dot{n}_{duct}}{\dot{n}_{duct}}\right)^2 + \left(\frac{\Delta T_{LII}}{T_{LII}}\right)^2 + \left(\frac{\Delta \dot{m}_{fuel}}{\dot{m}_{fuel}}\right)^2 + \left(\frac{\Delta P_{stat}}{P_{stat}}\right)^2}} \quad \text{(D.31)}$$

where N is the number of PM per volume. The relative bias uncertainty in particle number concentration is 10% based on the CPC specifications, *i.e.* $\frac{\Delta N}{N} = 0.10$. The other four terms in Equation (D.31) can be calculated similar to the methods explained in sections D.1 and D.2.

References

Choi, M. Y., Hamins, A., Mulholland, G. W., Kashiwagi, T. (1994). Simultaneous Optical Measurement of Soot Volume Fraction and Temperature in Premixed Flames. *Combustion and Flame,* 99(1):174-186.

Choi, M. Y., Mulholland, G. W., Hamins, A., Kashiwagi, T. (1995). Comparisons of the Soot Volume Fraction using Gravimetric and Light Extinction Techniques. *Combustion and Flame,* 102(1-2):161-169.

Dobbins, R. A., Mulholland, G. W., Bryner, N. P. (1994). Comparison of a Fractal Smoke Optics Model with Light Extinction Measurements. *Atmospheric Environment,* 28(5):889-897.

Park, K., Kittelson, D. B., Zachariah, M. R., McMurry, P. H. (2004). Measurement of Inherent Material Density of Nanoparticle Agglomerates. *Journal of Nanoparticle Research,* 6(2-3):267-272.

Wu, J. S., Krishnan, S. S., Faeth, G. M. (1997). Refractive Indices at Visible Wavelengths of Soot Emitted from Buoyant Turbulent Diffusion Flames. *Journal of Heat Transfer,* 119(2):230-237.

Appendix E Transmission electron micrographs for samples of particles from different flames

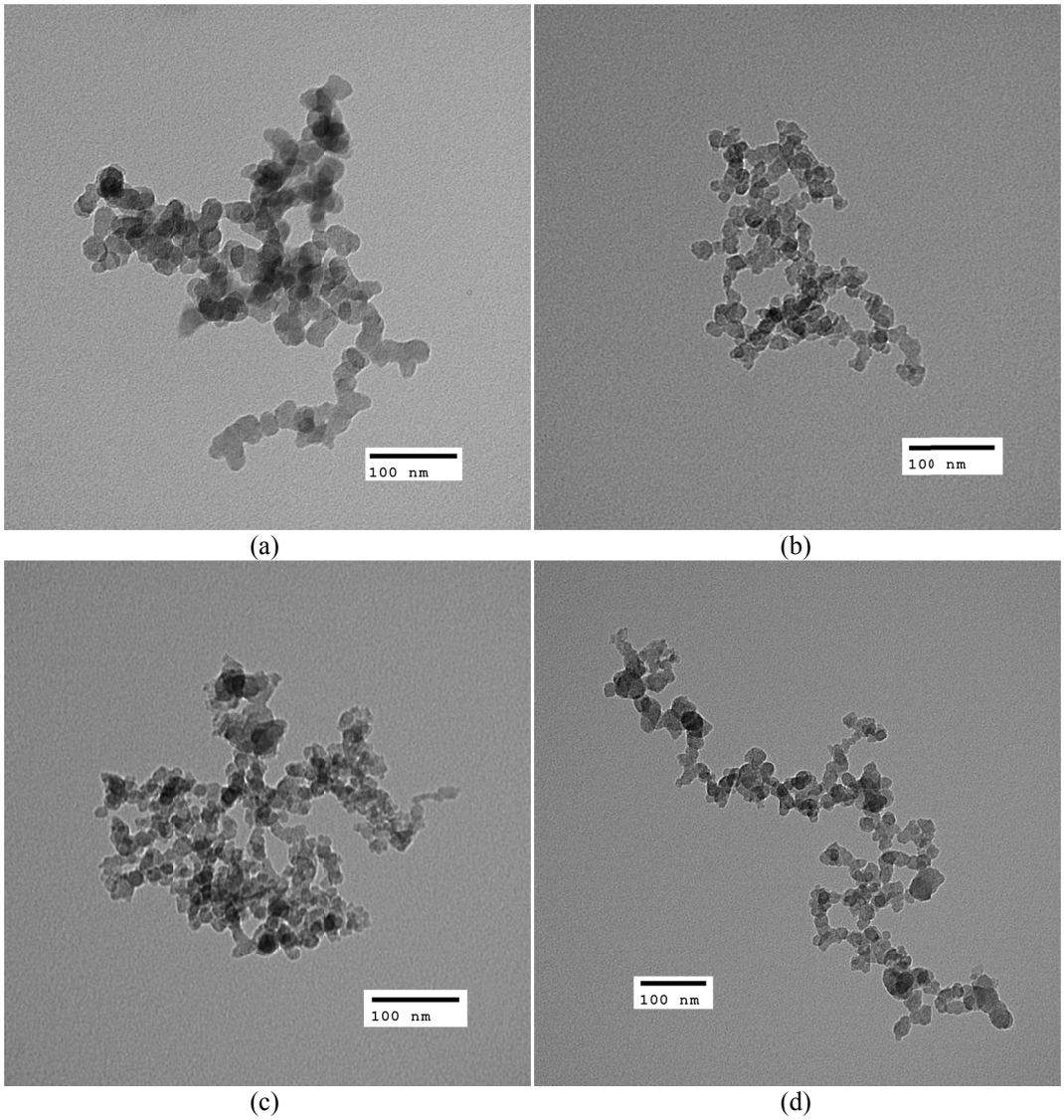

(a) (b)

(c) (d)

Figure E.1: Morphology of particles from flames with no liquid droplets

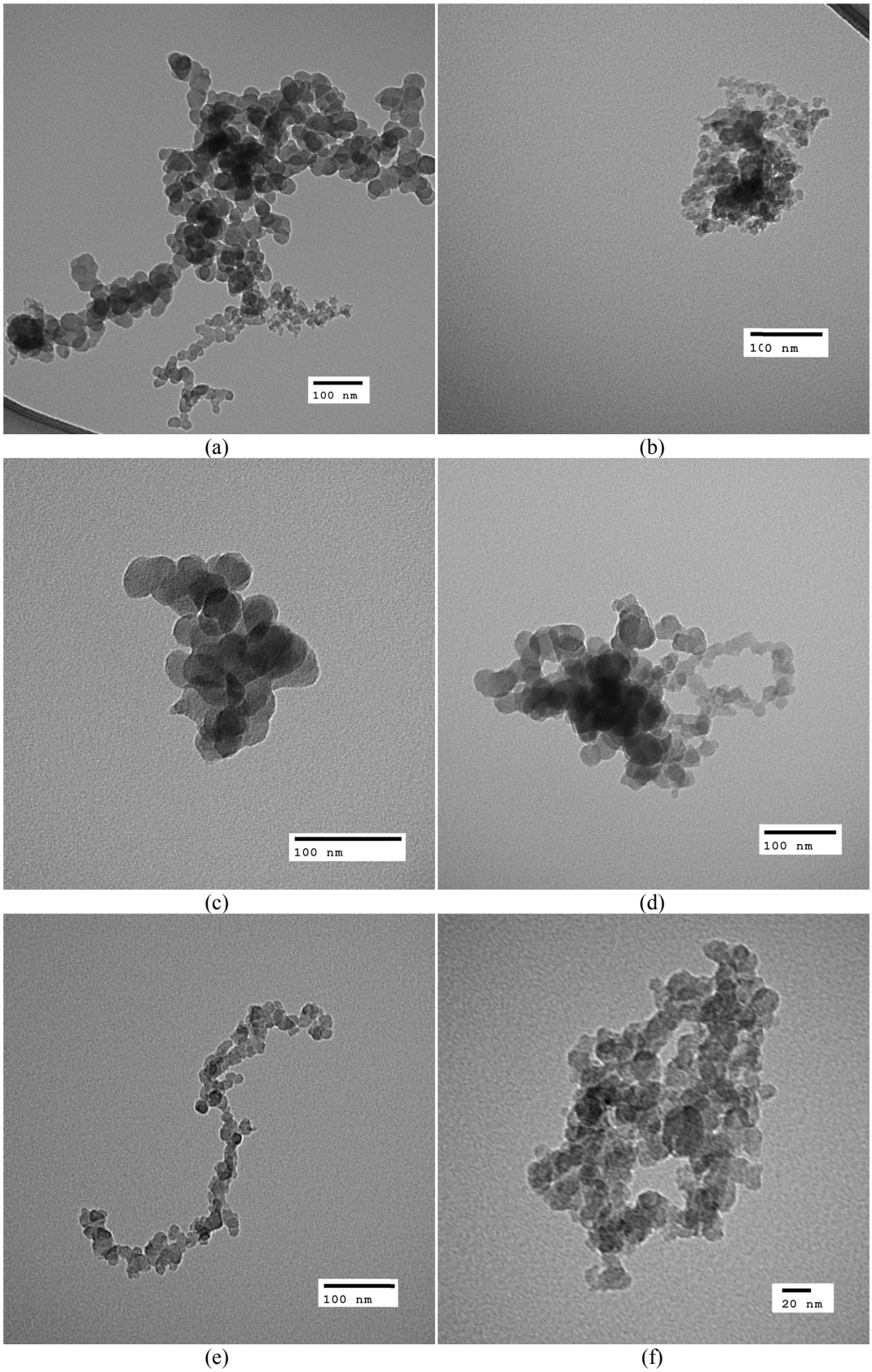

(a) (b)

(c) (d)

(e) (f)

Figure E.2: Morphology of particles from flames with distilled water droplets

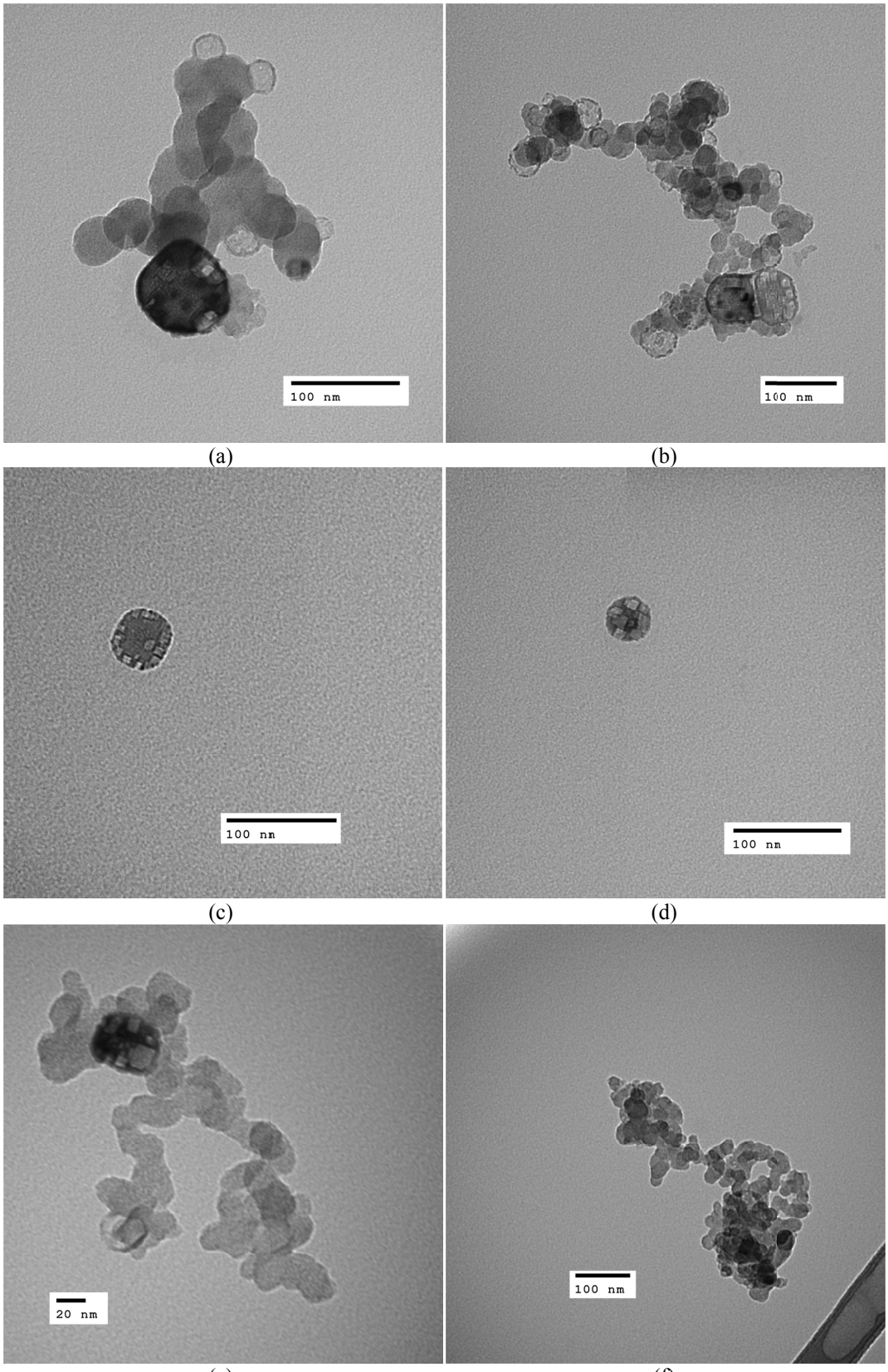

(a) (b)

(c) (d)

(e) (f)

Figure E.3: Morphology of particles from flames with droplets of NaCl solution

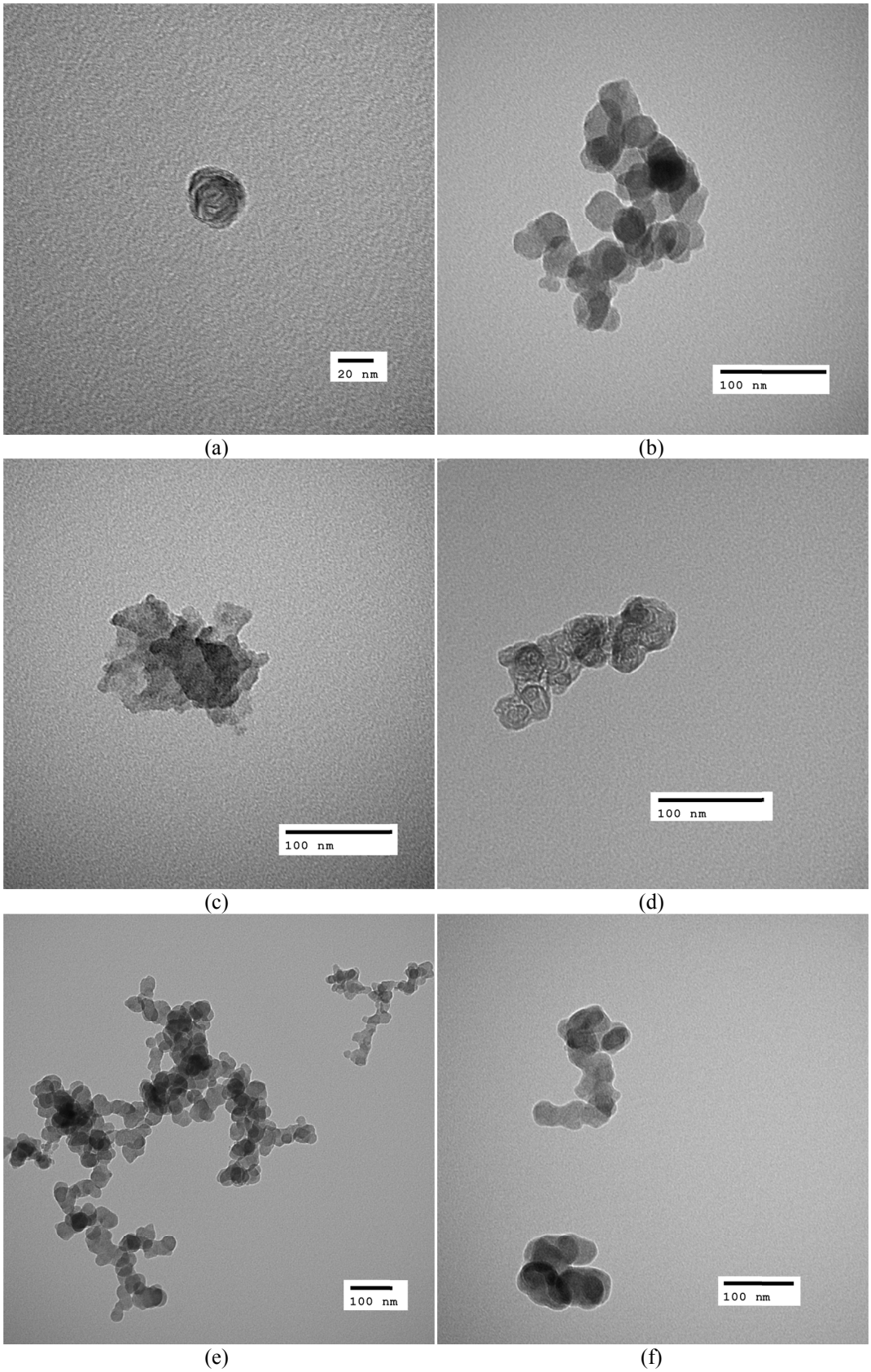

(a) (b)

(c) (d)

(e) (f)

Figure E.4: Morphology of particles from flames with HCl solution droplets

Appendix F Particle size distribution for various liquid mass ratios

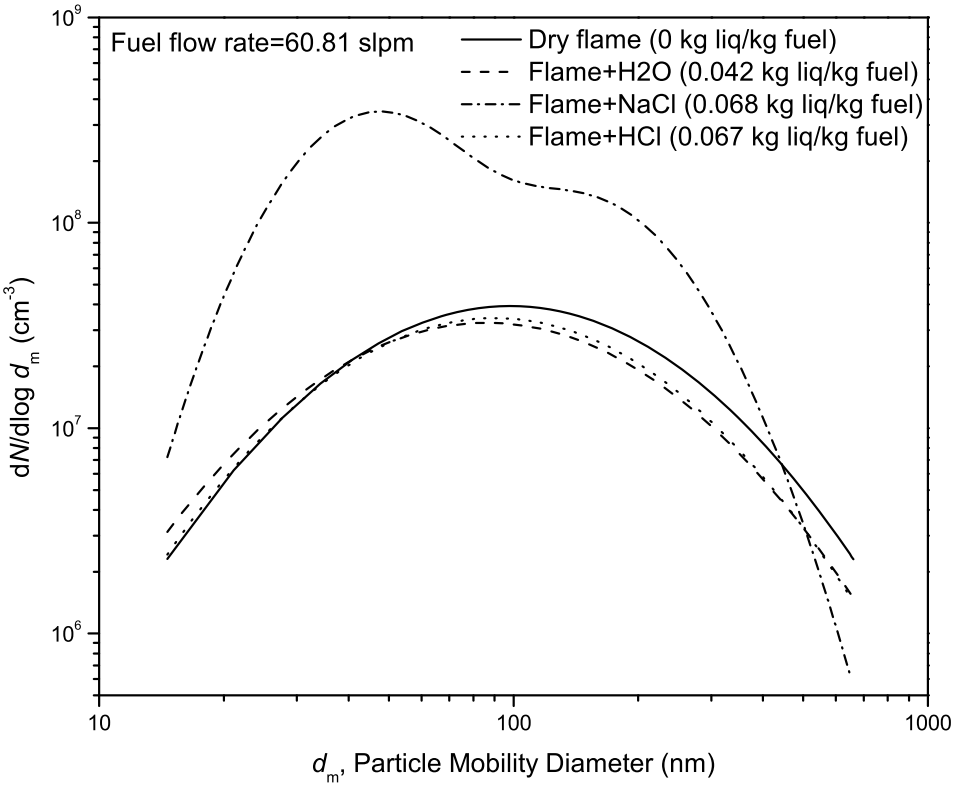

Figure F.1: Particle size distribution for the flare with fuel flow rate of 60.81 SLPM with different liquid mass ratios

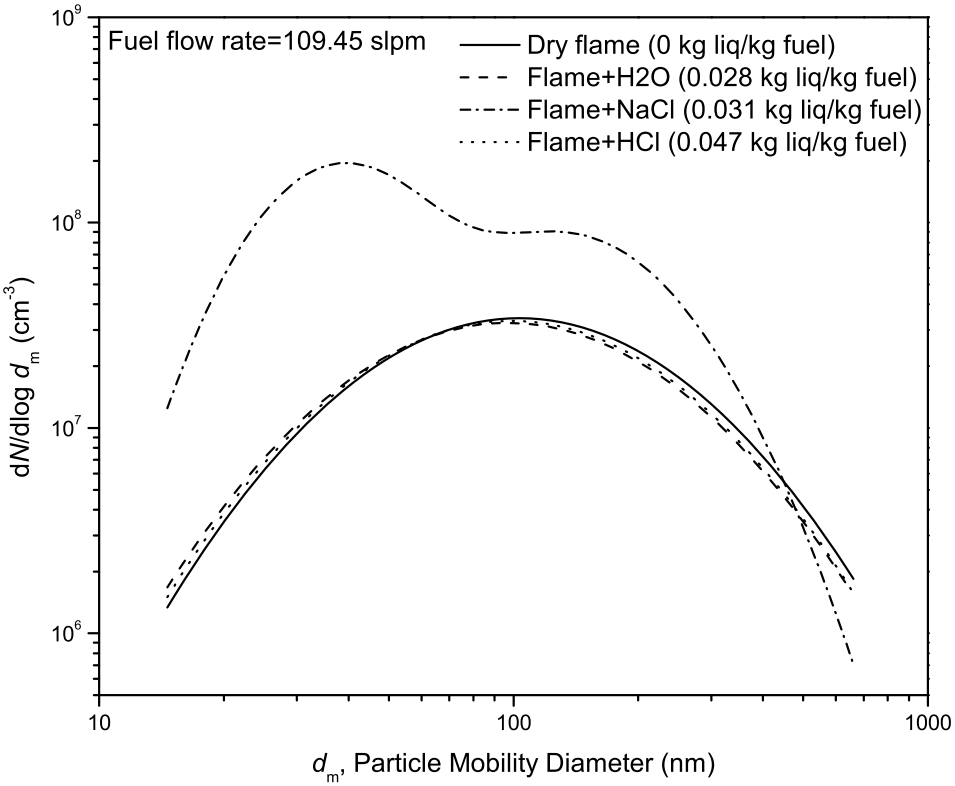

Figure F.2: Particle size distribution for the flare with fuel flow rate of 190.45 SLPM with different liquid mass ratios

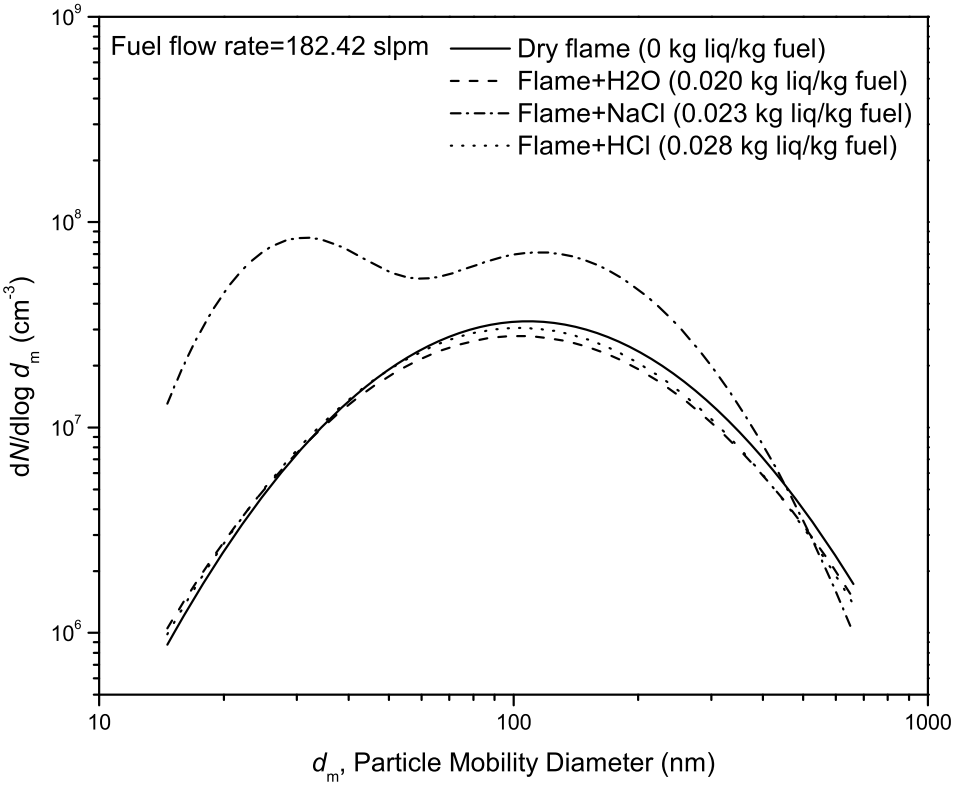

Figure F.3: Particle size distribution for the flare with fuel flow rate of 182.42 SLPM with different liquid mass ratios

Appendix G Particle size distribution for different liquid types

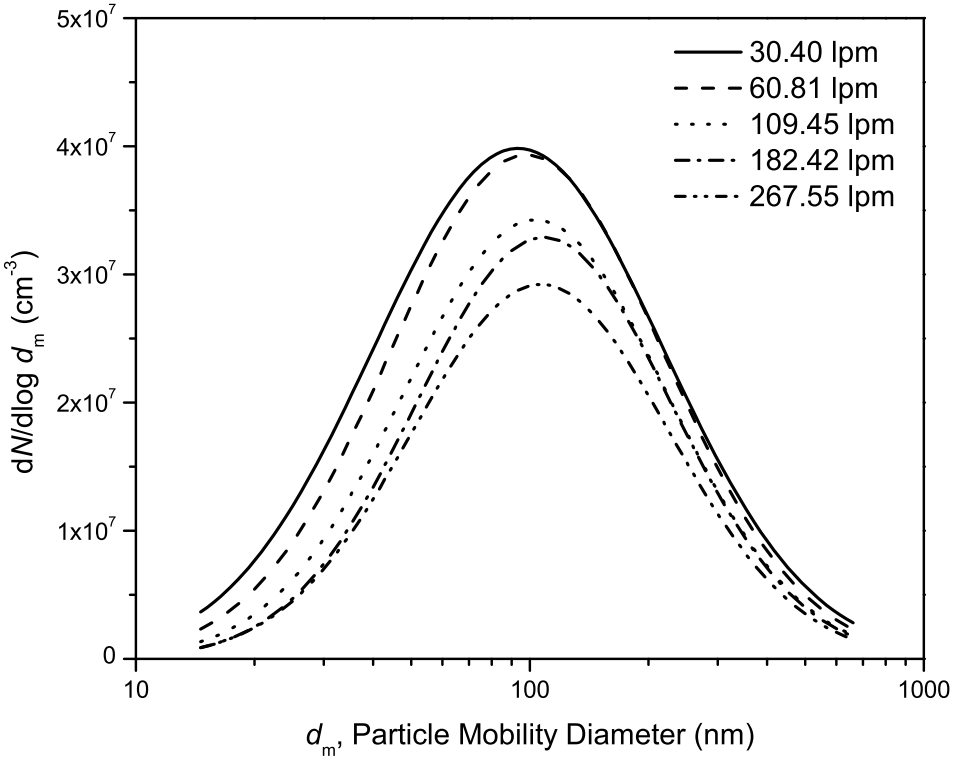

Figure G.1: Size distribution for particles from the dry flame with different fuel flow rates

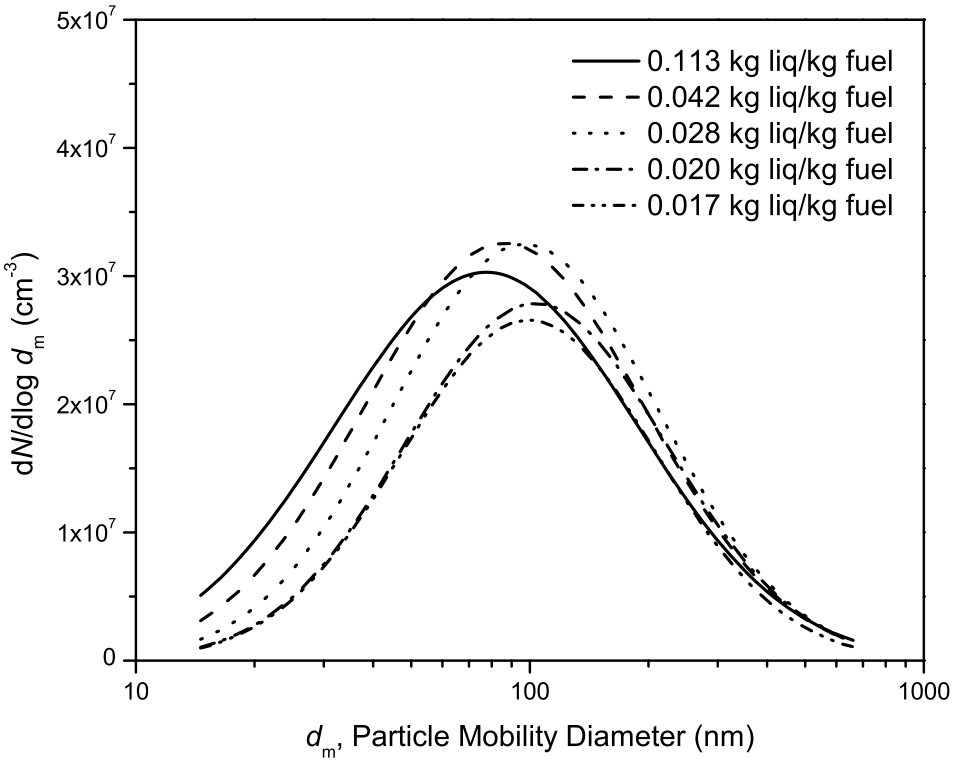

Figure G.2: Size distribution for particles from the flame with distilled water droplets at different liquid mass ratios

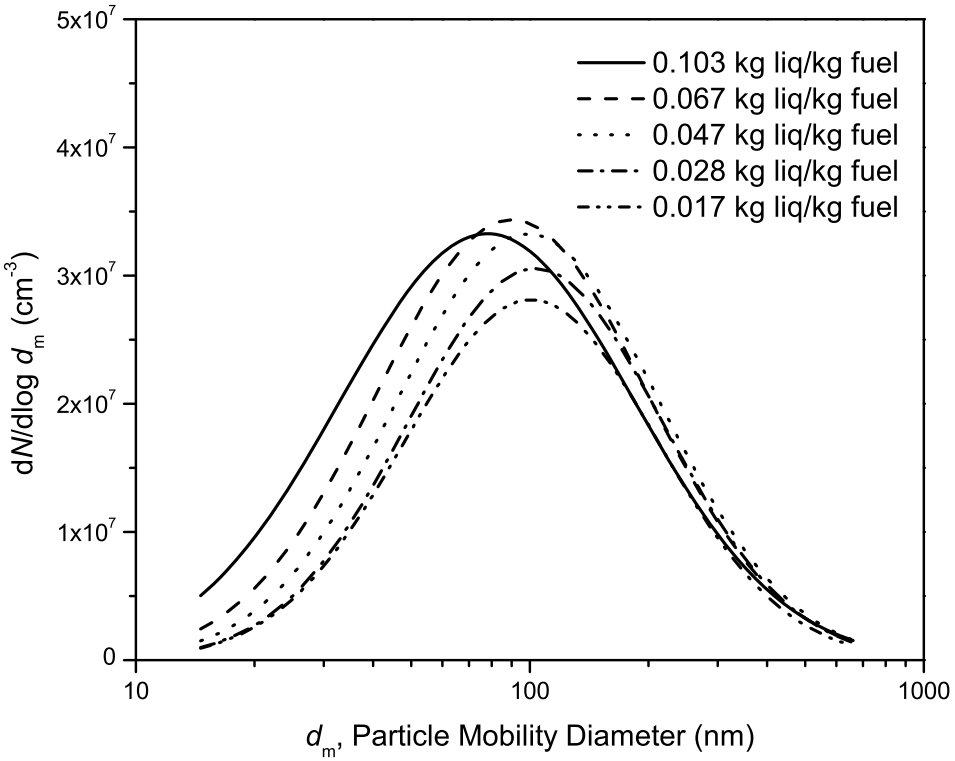

Figure G.3: Size distribution for particles from the flame with HCl solution droplets at different liquid mass ratios